UNIVERSITÀ DEGLI STUDI DI PADOVA

SCUOLA DI SCIENZE
Dipartimento di Geoscienze
Direttore Prof. Fabrizio Nestola

TESI DI LAUREA MAGISTRALE IN

GEOLOGIA E GEOLOGIA TECNICA

Geological characterisation of Cabeza de Vaca Mining District (Copiapó – Chile) by remote sensing, fieldwork and spectral analysis

Relatore: Prof. Matteo Massironi

Correlatore: Prof. Paolo Nimis

Laureando: Marco Trevisan

Matricola:1148467

Anno Accademico 2017-2018

INDEX

RIASSUNTO

La presente dissertazione di laurea è stata resa possibile grazie all'accordo internazionale tra l'Università di Padova e l'Università di Atacama (Cile) sita a Copiapò, (Regione di Atacama, Cile Settentrionale) e fondata nel 1857come prima Scuola Mineraria del Sud America.

Il lavoro svolto in questa tesi ha avuto come scopo la prospezione mineraria nei pressi del distretto di Cabeza de Vaca, situato nella Quebrada Carizallillo a 60 km a sud di Copiapò.

Lo studio è stato suddiviso in tre fasi:

Studio preliminare di telerilevamento: è stato svolto usando il sensore multispettrale ASTER con l'intento di caratterizzare l'area di studio e di individuare le principali unità geologiche e litologie affioranti.

Studio di campagna ed analisi di campioni rappresentativi: individuate le aree di interesse (zone di possibile alterazione idrotermale o discordanti rispetto alla cartografia geologica esistente) si è proceduto con la verifica e il campionamento in campagna. I campioni raccolti sono stati analizzati con l'utilizzo del microscopio ottico a luce trasmessa e analisi XRPD.

Studio di prospezione: individuate e classificate le varie litologie, mineralizzazioni ed alterazioni associate, è stato svolto un lavoro di prospezione mineraria usando il sensore iperspettrale Hyperion.

L'insieme di questi metodi ha permesso di giungere a nuove osservazioni utili allo studio minerario dell'area. In particolare sono state riconosciute le seguenti alterazioni:

- Propilitica: questa alterazione idrotermale di basso grado caratterizzata dai clorite e epidoto si trova in gran parte dell'area di studio.
- Fillica: questa alterazione è caratterizzata dall'associazione albite, muscovite e illite ed è stata segnalata come area di interesse.
- Argillica intermedia: è strettamente legata a sistemi idrotermali tipo breccia pipe ed High Sulfidation epithermal systems (HS). E caratterizzata dall'associazione illite e smectite.
- Argillica avanzata: nella maggior parte dei casi segue l'argillica intermedia. In questo caso appaiono i minerali alunite e caolino (o pirofillite in livelli crostali di maggiore profondità).
- Vuggy silica: questa alterazione è causata dalla percolazione di fluidi molto acidi che alterano totalmente la roccia incassante. Il prodotto di questa reazione è un aggregato monomineralico di quarzo con all'interno dei fori.

Lo studio di campagna, il lavoro di prospezione e i risultati delle analisi hanno permesso di individuare zone ad elevato interesse minerario per una possibile coltivazione di mineralizzazioni prevalentemente a rame ed oro. Nell'area di studio sono stati identificate infatti giacimenti epitermali ad oro (di tipo HS), campo di vene polimetalliche e breccia pipe a tormalina e quarzo.

INTRODUCTION

On the basis of the Academic Collaboration Agreement (Memorandum d'intesa) signed on 25 November 2016, the University of Padua and the University of Atacama (Copiapó, Chile) have agreed on a mutual exchange of students.

The University of Atacama is based in the city of Copiapó and was born in 1857. It is one of the most important universities in northern Chile and its main mission is to train professionals in the fields of geology, engineering, education and technology, incorporating the natural sciences and the legal sciences. The Department of Geosciences of the University of Padua has therefore launched a competition for three student exchange scholarships for a stay at the University of Atacama during the first semester of the academic year 2017/2018.

The three successful candidates, Lorenzo Albertini, Ilaria Sparelli Zambon, and me, spended three months working in different areas in the Atacama Desert.

My work contributes to the study of lithology and alterations in the Atacama region, focusing on one of the main mining sites (Quebrada Carizallillo). This region has been severely affected by hydrothermal alterations during the Cenozoic.

In particular, the aims of this work are:

1. To understand, with the use of remote sensing field surveys and laboratory analyses, which types of hydrothermal systems were active in the study area.
2. To integrate the currently available geological map through the identification and characterisation of alteration halos for future detailed mining exploration.

The research combines remote sensing techniques (using software ENVI 5.3) and field surveys as well as analytical studies on collected samples.

Remote sensing involves the elaboration of a satellite image Aster level 1T for the pre-fieldwork study and a Hyperion level 1T to search sites of mining interest during the period following the survey in the countryside. Part of the time in Chile was devoted to the fieldwork activity, mainly related to geological mapping of specific sites where samples were also analysed and described. The collected data were stored and processed in a GIS environment (software Arcgis).

Samples were used to create thin sections, for a preliminary study using the petrographic microscope, then, they were prepared for qualitative mineralogical analysis by X-ray diffractometry.

Combining all the elaborations and analyses, different zones have been identified as prospective for copper-gold ore deposits. Currently, breccia pipes and veins are exploited by local companies. Furthermore, the study of alterations identified some areas with high-sulphidation (HS) epithermal type systems. These particular deposits are formed at shallow crustal levels from fluids of dominantly magmatic-hydrothermal origin. These systems often occur above deeper porphyry-style systems. It is therefore hypothesized that a hidden porphyry copper deposit may be present at depth.

1 GEOGRAPHIC AND GEOLOGICAL SETTING

1.1 GEOGRAPHIC SETTING

Chile stretches north to south along the South American mainland for over 4000 km, from 18°S, where it borders with Peru, Bolivia and Argentina, to 56°S at Tierra del Fuego and the islands of Cape Horn. Its western margin is the Pacific Ocean, and its eastern boundary are the Andes Mountains, so that in a width of rarely more than 200 km, the topography rises from sea level to a maximum of almost seven thousand metres.

Figure 1.1_The regions of Chile; from the site www.emaze.com

The study area is located in the Atacama region (Figure 1.1), also named the third Chilean region, in a location called Quebrada Carizallillo. The exact position is between latitudes 27° 37' and 27° 41' South and longitudes 69° 53' and 70° 02' West.

Figure 1.2_ Google Earth view of the area of Quebrada Carizallillo. The studied area is outlined by the red rectangle.

1.2 GEOLOGICAL SETTING

During most of its history, the continental margin of South America was an active plate margin. The Late Proterozoic to Late Palaeozoic evolution was punctuated by terrain accretion and westward arc migration. Although accretion of some terrains has been documented for the post-Triassic history, the evolution during post-Triassic times is characterized more by the eastward retreat of the continental margin and eastward arc migration. The intermediate period, comprising the Late Permian and the Triassic, corresponds to an episode of no, or very slow, subduction activity along the continental margin, during which a totally different

palaeogeographic organization was developed and a widely distributed magmatism with essentially different affinities occurred.

During the long-lived history of the Chilean Andes is possible to differentiate five major tectonostratigraphic stages.

- Pampean tectonic cycle (Late Proterozoic–Early Cambrian);
- Famatinian tectonic cycle (latest Cambrian–Early Devonian);
- Gondwanan tectonic cycle (Late Devonian–earliest Permian);
- Pre-Andean tectonic cycle (Latest Permian–earliest Jurassic);
- Andean tectonic cycle (late Early Jurassic–Present).

The area of study is characterized by rocks formed during the Andean tectonic cycle.

The early evolution of this cycle in northern Chile (north of 39ºS) is characterized by the development of a magmatic arc parallel to the Pacific Ocean and a relative backarc basin on its eastern side. In contrast, the later evolution (Late Cretaceous and Cenozoic) is characterized by the gradual shift to more easterly positions of the magmatic arc, and by the development of the foreland basins on the eastern side of the arc. These two major periods correspond to the Early Andean Period and Late Andean Period, respectively, well described by (Coira et al. 1982). Each of these periods can be subdivided into shorter stages, which can be differentiated from each other by major palaeogeographic changes, due to changes in convergence and subduction pattern in the region. In particular, the evolution of the Andean tectonic cycle can be described in three stages: Early Jurassic–late Early Cretaceous; Late Cretaceous–Early Palaeogene; and Late Palaeogene–Present. Some of these stages have been in turn subdivided into substages (Figure 1.3,) (Charier et al. 2007).

An important feature is the development of major trench-parallel shear zones developed along the axes of the successive magmatic arcs, i.e. the Atacama, Domeyko (Figure 1.3). All of them can be traced for several hundreds of kilometres of fault systems along the mountain range (Figure 1.3).

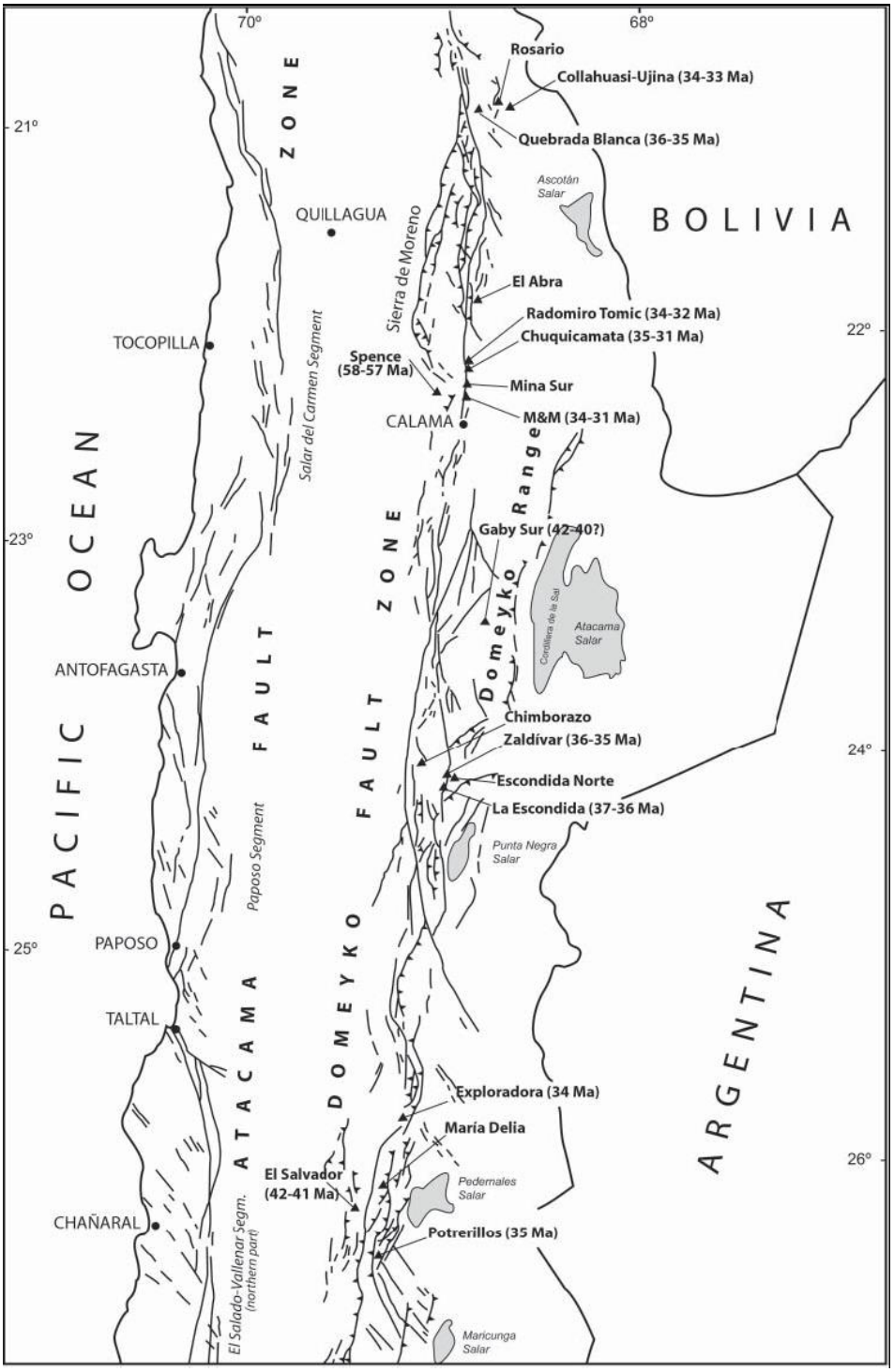

Figure 1.3_ The Atacama Fault System (SFA) and the Domeyko Fault System (SFD) (Charrier et al., 2007)

ANDEAN TECTONIC CYCLE

PERIODS*	STAGES**	SUBSTAGES**	AGE
Late Period	Third Stage		Late Paleogene to Present
	Second Stage	Second Substage	Early Paleogene (Paleocene-Early Eocene)
		First Substage	late Early Cretaceous to Late Cretaceous
Early Period	First Stage	Second Substage	Kimmeridgian-Tithonian to Albian
		First Substage	late Early Jurassic to Kimmeridgian

* Subdivision according to Coira et al. (1982)
** Subdivision according to this work

Table 1.1_ Subdivision in stage of the Andean tectonic cycle Coira (1982)

1.2.1 First stage: Early Jurassic–late Early Cretaceous

The first stage of the Andean cycle north of 39ºS corresponds to the development of a north-south magmatic arc along the present-day Coastal Cordillera and a backarc basin to the east.

In this time, subducting plate remained inactive for 40–50 million of years. This condition was maintained for most of Jurassic and Early Cretaceous time, permitting the dominance of extensional tectonic conditions on the continental margin, intense magmatic activity along the arc, and abundant sedimentation in the backarc basin (Pardo-Casas and Molnar 1987). Contemporaneously with volcanism, huge batholiths were emplaced into the volcanic succession.

In this first Andean stage it is generally possible to separate two substages (Charrier, 2002) where:

- The first substage (late Early Jurassic to Kimmeridgian) is characterised by intense activity in the arc and development of a transgressive–regressive marine cycle in the backarc basin.
- The second substage (Kimmeridgian to Aptian–Albian) is characterised by apparently less activity in the arc in some regions, and by a second transgressive–regressive marine cycle in the backarc basin. The existence in the backarc basin of regions that were covered by the sea and others that

remained under a continental regime indicates considerable palaeogeographic variations along the basin. At the end of the first substage the sea progressively retreated from the backarc basin and gave rise in Oxfordian and Kimmeridgian times to the deposition in most regions of thick gypsum levels used as stratigraphic boundary.

1.2.2 Second stage: late Early Cretaceous–Early Palaeogene

In late Early Cretaceous times, a major change in plate interactions occurred along the continental margin. This episode can be related to the Cretaceous phase of very rapid ocean crust production in the primitive Pacific Ocean (Larson 1991), and probably was linked to a reduction of the subduction angle below South America (Chilean-type subduction). As a consequence of these modifications, the second regression episode of the previous stage culminated in the emergence of the continental margin during an episode of intense contractional deformation, with uplift and erosion of the pre-existing units, particularly of the Early Jurassic to Early Cretaceous backarc basin fill (backarc basin inversion). This tectonic phase (the so-called Subhercynian or Peruvian; see Charrier & Vicente 1972; Aubouin 1973b) marks the separation between the early period and late period into which Coira et al. (1982) subdivided the evolution of the Andean tectonic cycle. After this episode the palaeogeographic organization in this region of the Andes changes completely: the magmatic arc shifted considerably eastwards, a continental foreland basin was formed to the east of the arc instead of a backarc basin, and a rather wide forearc region west of the arc was produced as a result of eastward arc migration. Oblique subduction also prevailed at this time, since the movement of the Farallon oceanic plate towards the continent was north–southward, producing dextral displacement along north–south orientated transcurrent fault system (Figure 1.4) (Pardo-Casas and Molnar 1987).

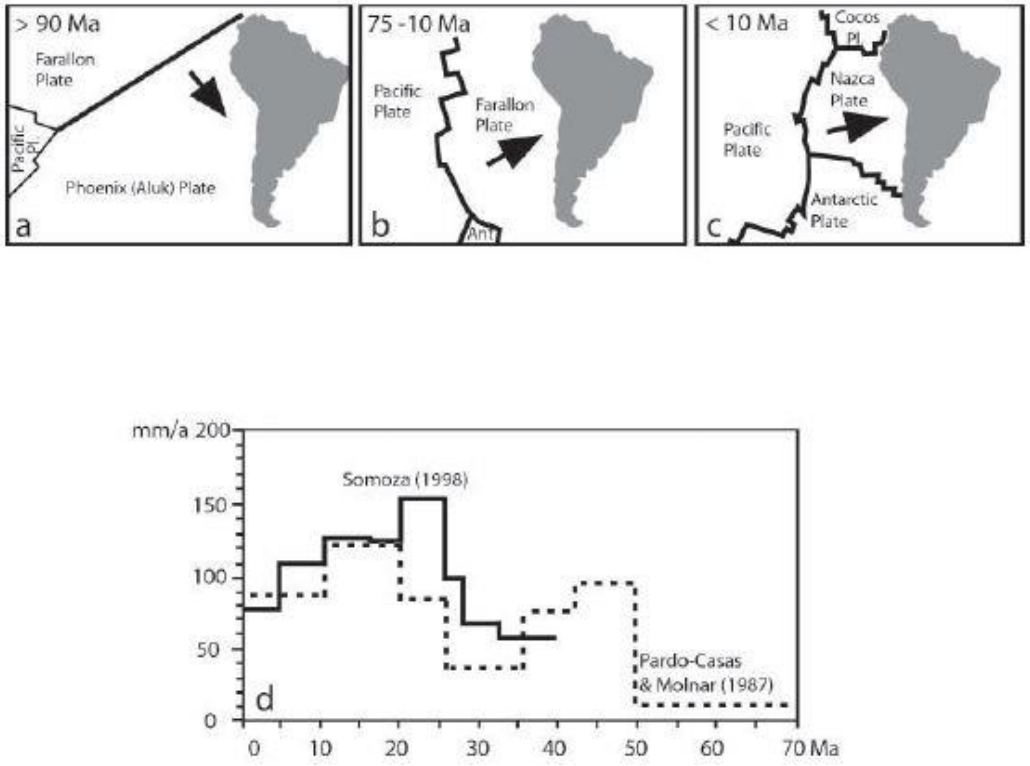

Figure 1.4_Plate geometries for (a) Early Late Cretaceous; (b) Late Cretaceous to late Miocene, and (c) Late Miocene to Present, taken from Scheuber et al. (1994) and Reutter (2001). Different obliquity between (a) and (b) explains different movements along the Atacama Fault Zone in Jurassic to Early Cretaceous times (sinistral) and in Late Cretaceous times (dextral). (d) Cenozoic convergence rate curves between the Farallon and Nazca plates and South America according to Pardo-Casas & Molnar (1987) and Somoza (1998).

This stage of Andean evolution is characterised by extensional episodes associated with intense magmatic activity. This activity is represented by major plutons and abundant volcanic deposits of andesitic and rhyolitic-dacitic nature, frequently associated with development of great calderas as the Megacaldera Carizallillo and other smaller one in the Atacama Region. The Late Cretaceous deposits in this stage accumulated in a series of fault controlled extensional basins located along the magmatic arc: Cerro Empexa, Quebrada Mala and Llanta (Cornejo et al. 2003). Latest Cretaceous and earliest Palaeocene inversion of these basins was followed by the development of early Palaeogene depocentres further to the east where more thick volcanic and volcaniclastic successions were deposited (Rivera, et al. 1994). The end of the stage is marked by a major deformation event in Eocene times.

1.2.3 Third stage: Late Palaeogene–Recent

The third stage corresponds to the last phase of Andean development, during which the Argentina–Chilean Andes adopted their present configuration. During this stage Andean uplift took place, morphostructural units were formed, the volcanic arc reached its present position, and the porphyry copper deposits were emplaced.

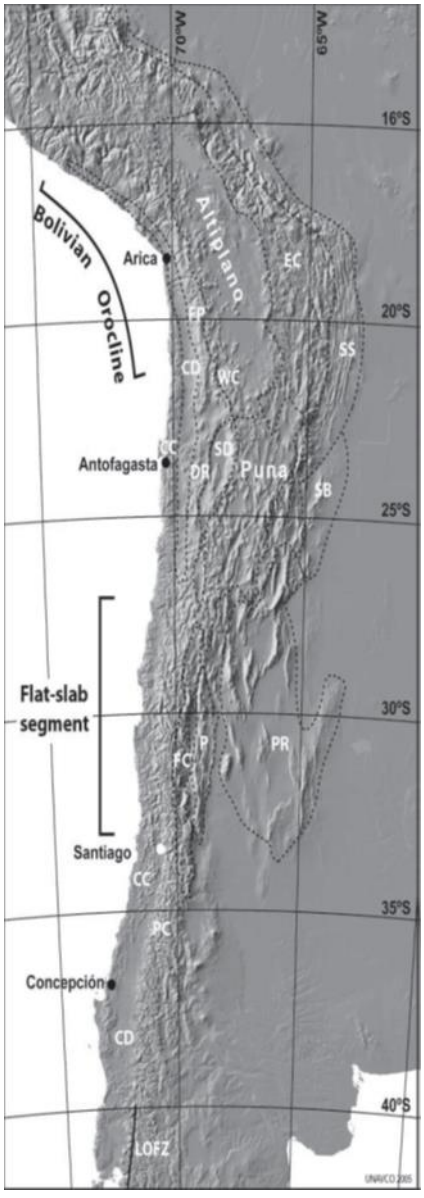

Figure 1.5_ Digital elevation model of the Andes between 16ºS and 40ºS with indication of the main geographical, tectonic and morphostructural features. Compare with Figure 3.2a. Abbreviations: CC, Coastal Cordillera; CD, Central Depression; EC, Eastern Cordillera; FC, Frontal Cordillera; FP, Forearc Precordillera western flank of the Altiplano) and, further south, Sierra de Moreno; LOFZ, Liquiñe–Ofqui Fault Zone; P, Precordillera in Argentina; PC, Principal Cordillera; PR, Pampean Ranges; SB, Santa Barbara System; SD, Salars Depression; SS, Subandean Sierras; WC, Western Cordillera. Geology of Chile, 2007.

Deformation of the deposits of the previous stage occurred in middle Eocene times at the end of an episode of increasing convergence rate (Pardo-Casas and Molnar 1987). According to (Pardo-Casas and Molnar 1987) and (Somoza 1998), after this episode of high rate convergence, relative displacement of the oceanic and continental plates was almost parallel to the continental margin, and the convergence rate diminished until 26 Ma. At this moment, another plate readjustment occurred and the oceanic plate adopted an almost orthogonal motion relative to the continental margin (Yáñez et al. 2002), and convergence rate was increased until 12 Ma (Ramos 1999; Pardo-Casas and Molnar 1987) (*Figure 1.4*). These modifications of the plate kinematics and convergence rates caused important variations of the tectonic regime on the continental margin, expressed in the forearc (i.e. the western side of the Andes) by uplift and synchronous extensional, strike-slip, and compressional deformation (Hartley et al. 2000).

The units formed during late Eocene to Present times are exposed in all morphostructural units (Figure 1.6). However, the distribution of the deposits is not uniform and, furthermore, their continuity in the Central Depression is interrupted in the flat-slab segment as a consequence of major uplift caused by the present-day subduction of the Juan Fernández Ridge. In this intermediate Andean segment, which lies between 27ºS and 33ºS, no Central Depression is developed, volcanic activity is absent along the axis of the cordillera, and the Frontal Cordillera (Figure 1.5). Quebrada Crizallillo is situated at the beginning of this transition in the north side.

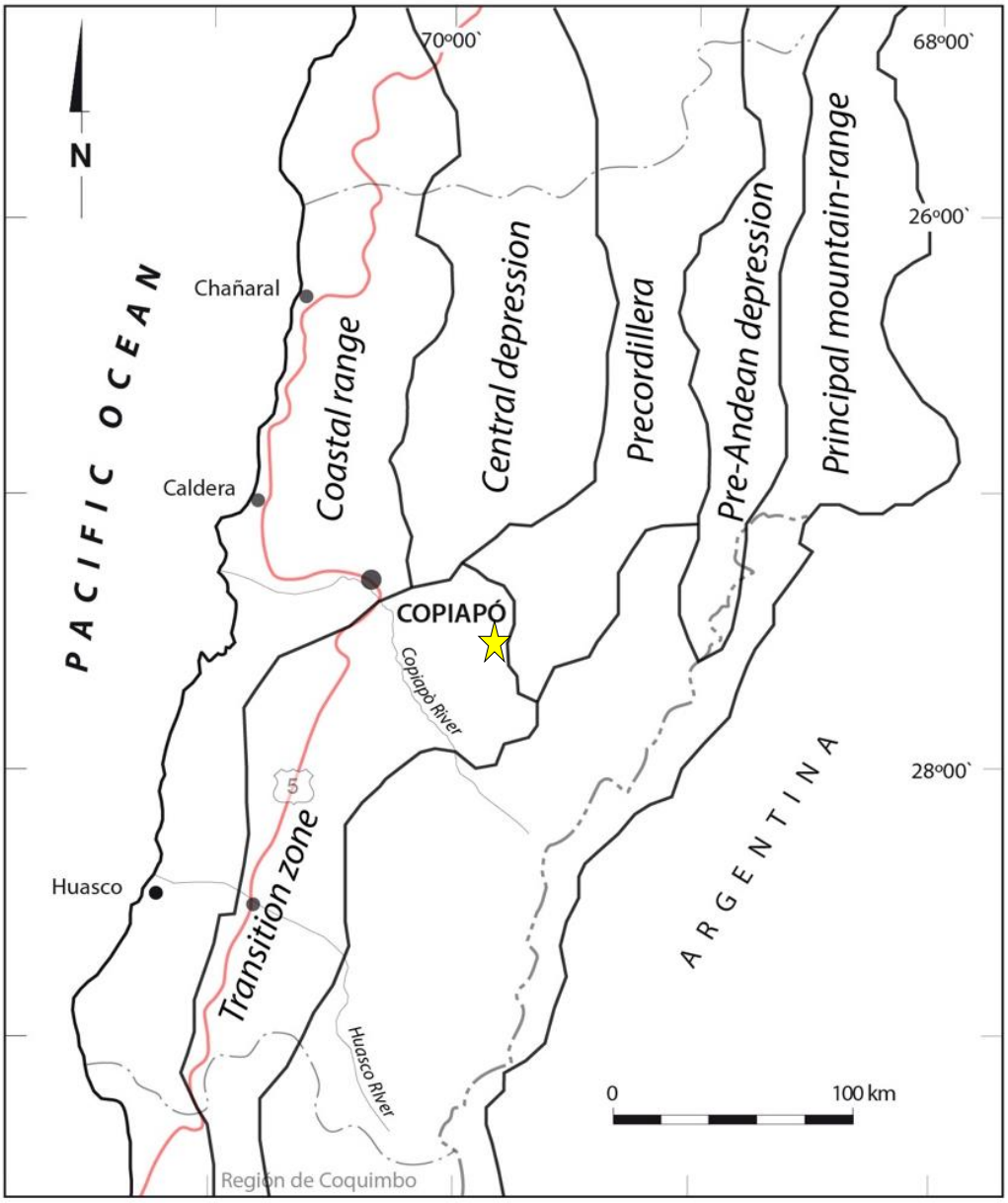

Figure 1.6_ Morphological units of northern Chile between 26°- 30°S, The star shows the position of the studied area.

1.3 METALLOGENIC SETTING

1.3.1 General Chilean setting

The work on subduction zones of Uyeda and Nishiwaki (1980) showed that there are two extreme types of subduction zones, which are characterised by different metal endowments. The so-called Mariana-type subduction (from the Marianas arc in the western Pacific) is characterised by a high angle of subduction and development of a marginal back-arc basin. In contrast, the Chilean type is characterised by the development of a big accretionary wedge associated with high tectonic activity (Dallmeyer et al. 1996). In Mariana-type margins, the conditions are adequate for the generation of submarine exhalative deposits, such as the Kuroko-type deposits in Japan, whereas the Chilean-type margins are more favourable for the generation of porphyry coppers. The current Chilean-type subduction in the Central Andes has been maintained since the Upper Cretaceous, while during the Jurassic and Lower Cretaceous the subduction was similar to the Mariana one (Boric 1990). Hence, the copper mineralization occurring in the igneous rocks associated with the Jurassic to Early Cretaceous magmatic arc are rare (Andacollo and some subeconomic prospects such as the Zona de Altering Domeyko – Dos Amigos). In contrast, porphyry coppers are the most economically important deposits associated with the igneous rocks of the youngest magmatic arcs in northern Chile (Figure 1.7)

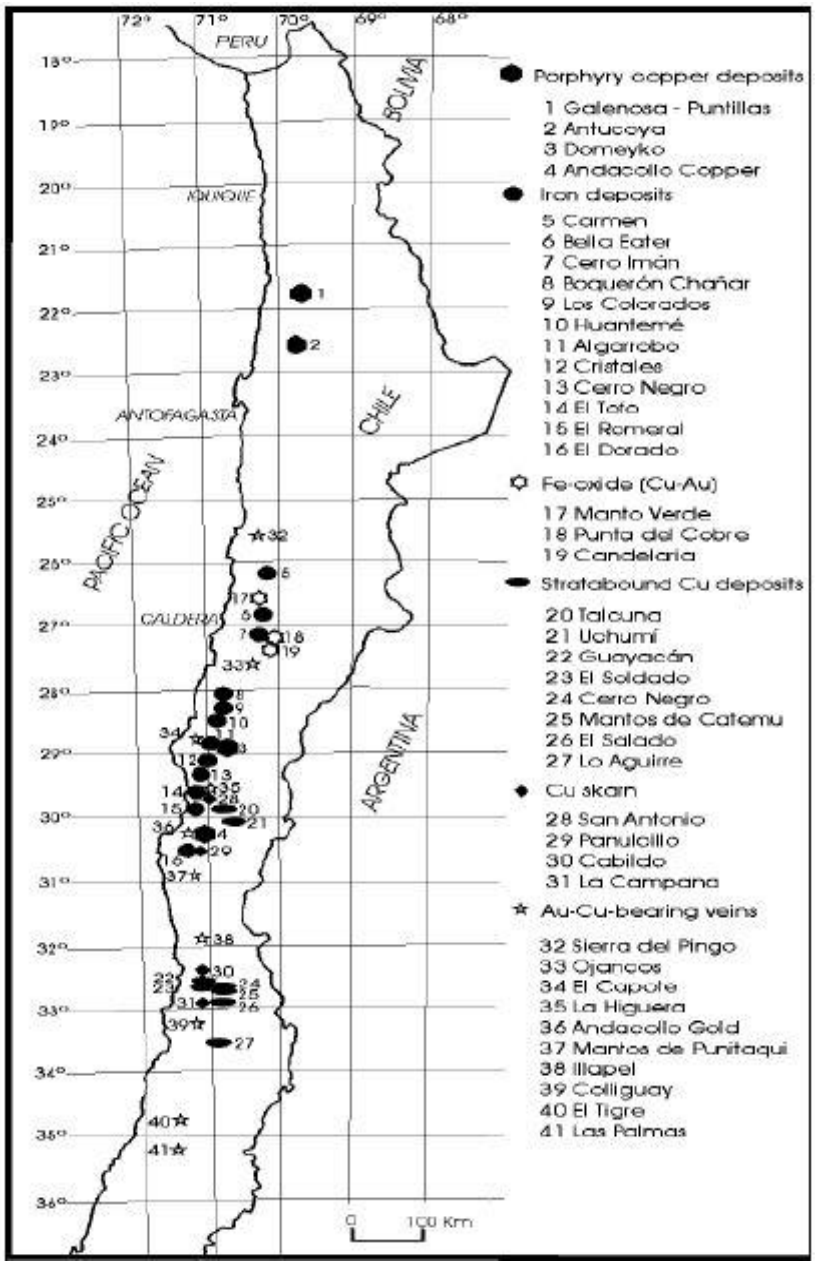

Figure 1.7_ Distribution of the main ore deposits located in north of Chile. The yellow star shows the area studied in this work..

Porphyry coppers in Chile are distributed in five metallogenic belts (Figure 1.8), mainly between 18 and 34º S and extend in age from the Lower Cretaceous to the Pliocene. These metallogenic belts are (1) the Cretaceous Belt, (2) the Lower Paleocene-Eocene Belt, (3) the Upper Eocene-Oligocene Belt, (4) the Upper

Oligocene-Middle Miocene Belt and (5) the Upper Miocene-Pliocene Belt (Campus 2003).

The porphyry copper mineralisation of Cretaceous age has been recognised on the eastern flank of the Cordillera de la Costa (Figure 1.7). According to their geographical distribution, the deposits form three clusters located in the north of the country (Antucoya-Buey Muerto and Galenosa-Puntillas) (Figure 1.8), in Central Chile (Andacollo, Domeyko, Pajonales and Los Loros) and in the south (San José, Polcura and Galletué), respectively (Campus 2003).

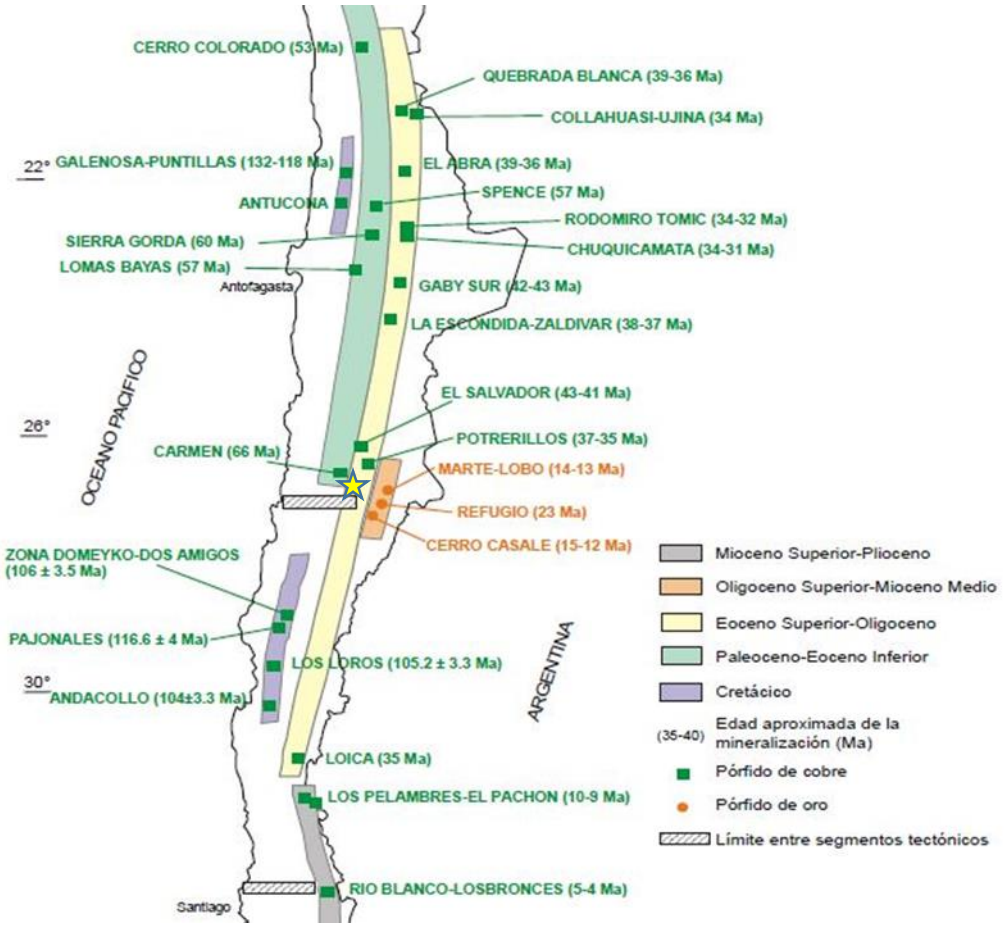

Figure 1.8_ Metallogenic porphyry copper and porphyry gold belts in Chile, with location of the main deposits and prospects. The yellow star shows the area studied in this work.

1.3.2 Metallogenic setting of Quebrada Carizallillo

Quebrada Carizallillo is host to several mining areas. This zone is characterised by volcano-sedimentary units of the Upper Cretaceous (Kennth 1968). In the

Cabeza de Vaca mining district, emerge a complex of tourmaline-quartz breccias, related to Cu, Mo ± Au, Ag, Pb and Zn (Marschik, 1996). Historically, the district has been exploited mainly for Cu and Au (Marschik, 1996). Currently, in this district there is a mining project, which is being explored by the Canadian-based consulting firm called "Acapella Mining Developments".

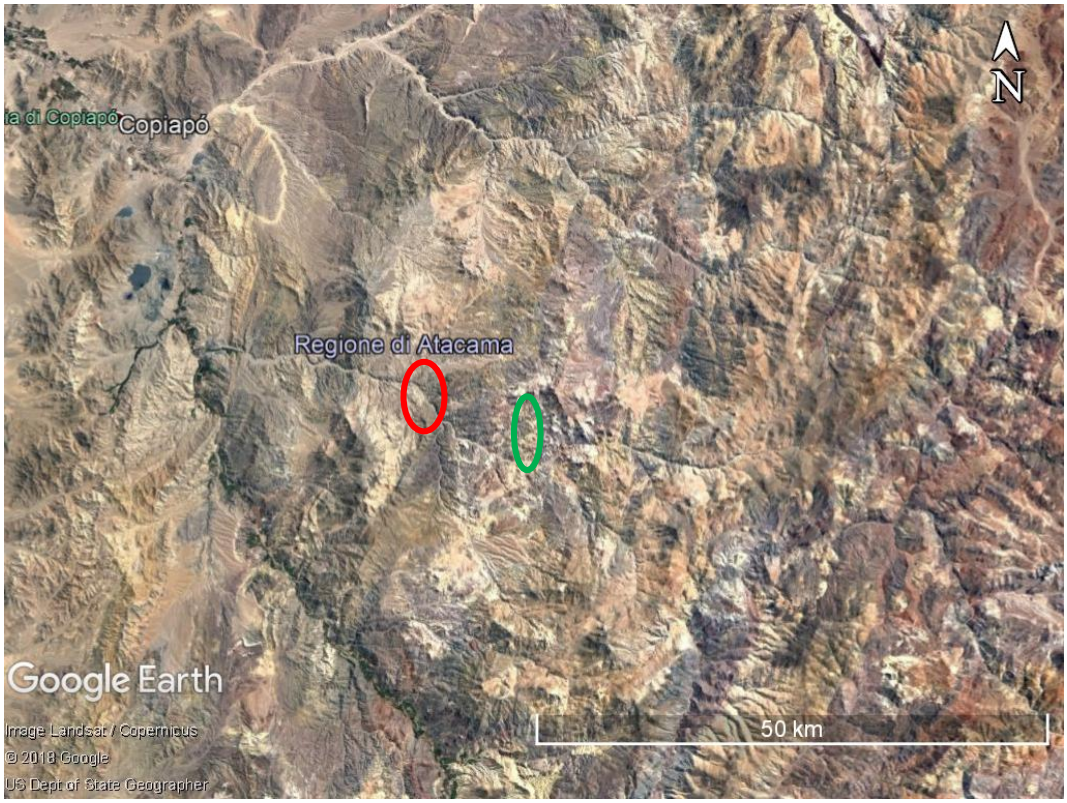

Figure 1.9_ The studied area of Quebrada Carizallillo. The red ellipse shows the breccia pipe zone and the green ellipse indicates the location of project JASPE.

In a neighbour place (Figure 1.9), the company ARAGONITA ASESORIAS LTDA bought the mining lease to investigate the area within a project called JASPE (Aragonita Asesorias LTDA 2016). In particular, the JASPE reports have shown that the area was subject to different types of hydrothermal alterations due to the development of a high-sulfidation system (Figure 1.10), composed of three epithermal bodies. The average Au grade of the bodies is 0.35 g/tonn, with increasing Cu concentrations with depth. In the following, the area of the JASPE project will be called ‘Carizallillo alteration zone’.

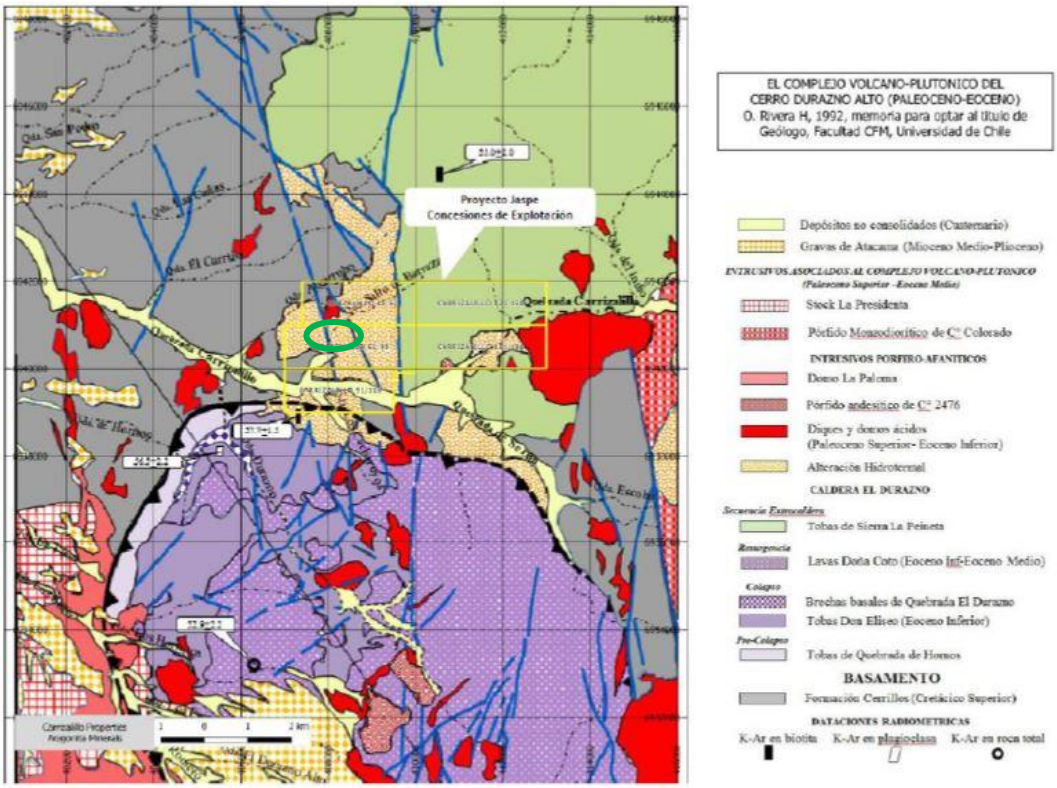

Figure 1.10_Geologic map shows the concessions bought by Aragonita Asesorias LTDA (yellow reptangle). Indeed the green ellipse shows the position of the ephitermal system.

2 ORE DEPOSITS ON CONTINENTAL ARCS

Activity of magmatic centres producing intermediate to felsic igneous rocks is associated with a large number of hydrothermal deposits of different metals (Ridley 2013). The magmatic centres associated with hydrothermal deposits are generally groups of small intrusions, such as dykes and stocks, which can mark the eroded roots of long-lived volcanoes. These igneous bodies are the remains of upward migration of magmas derived from a larger pluton. In these cases, the magmatic centres develop above dome-shaped protrusions or on top of the pluton. In other cases, there is no indication of an immediately underlying large pluton, and the small intrusions may have been generated from deep crustal levels.

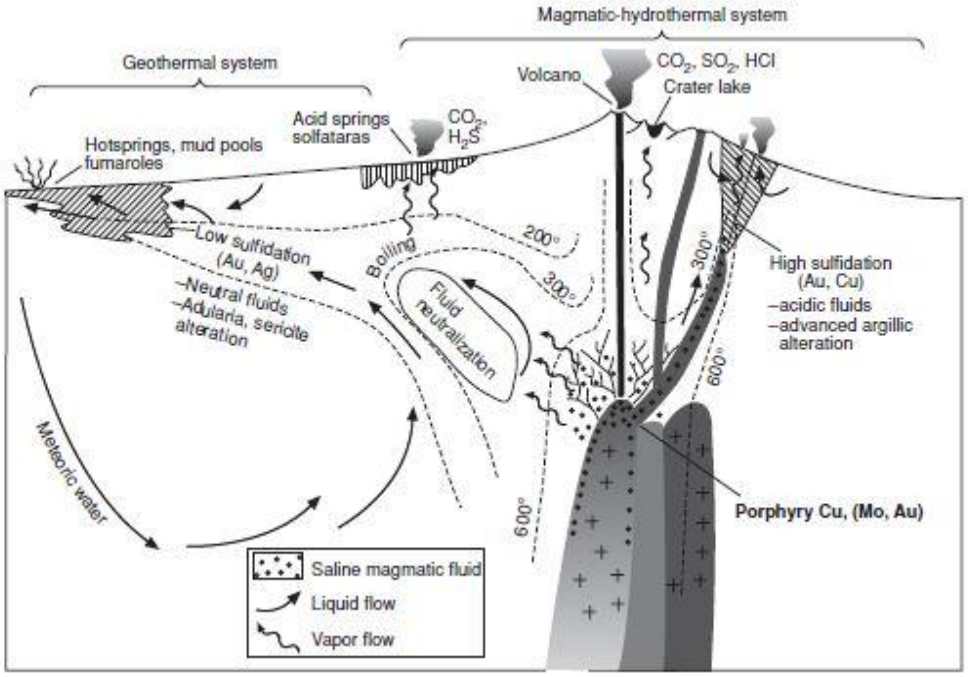

Figure 2.1_Simplified sketch of a porphyry-epithermal system (Robb, 2005)

Indeed, multiple magmatic centres may form above the same large plutons (Ridley 2013).

A great variety of ore deposits may form around magmatic centres (Figure 2.1). They are distinguished on the basis of metals associations, style of mineralisation, and geological setting of ores.

The ore deposits in which metals derive directly from the underlying magma are:

1. *Porphyry deposits:* large-tonnage deposits of low-grade disseminated ore associated with pervasive hydrothermal alteration within and immediately around intermediate to felsic porphyritic stocks that have intruded shallow levels of the crust. These are most commonly ores of Cu, or Cu with Au or Mo, more rarely of Mo or of Sn–Ag.

2. *Greisens and related deposits:* deposits of predominantly Sn and W together with Mo, F, Li and B in quartz–muscovite metasomatically altered (greisenised) granite at the top of an intrusion, or in sheeted quartz veins in and adjacent to altered granite.

3. *Skarn deposits and carbonate replacement deposits:* deposits of one or more of the metals Cu, Au, Fe, W and Pb–Zn in carbonate-bearing rocks that have been metasomatically replaced. In skarns the metasomatic replacement also produces high-temperature calc-silicate gangue minerals, whereas in carbonate replacement deposits the replacement is essentially by sulphide minerals.

4. *Vein fields:* swarms of veins centred on clusters of small intermediate or felsic intrusions, often extending over several kilometres from the intrusions, and often with a spatial zonation of metal content.

5. *Epithermal deposits:* a diverse set of deposits mainly mined as ores of Au, Ag and Cu, which form at relatively low temperatures and shallow depths around volcanic centres and in geothermal fields.
    - 5.1. *High-sulphidation epithermal deposits:* these are closely associated with volcanic centres and are hosted by intensely altered rocks.
    - 5.2. *Low-sulphidation epithermal deposits:* these have different ore and alteration mineralogy, are more typically vein-hosted and are generally in more distal settings relative to volcanic centres.

In this chapter, I summarise the main features of the deposit types and structures that have been encountered during the thesis work or that are the most likely to occur in the study area.

2.1 PORPHYRY DEPOSITS

Porphyry deposits represent a repeated and distinct mode of hydrothermal fluid escape from large intrusions in the crust. The three most important commodities by value worldwide in these deposits are Cu, Mo and Au. They are the dominant world source of Cu (> 65% production) and Mo (> 95% of production) and account for significant proportions of production of Au, and also for Ag and Re as by-products. (Ridley 2013) Porphyry deposits are large deposits with between 1 Mt and 10 Gt of ore in pervasively altered and veined rock in which ore minerals are uniformly disseminated at relatively low grades. Grades are commonly less than 1% Cu in a copper porphyry deposit, about 1 ppm Au where this is an economically important product, and about 0.1% Mo in a molybdenum porphyry deposit. (Ridley 2013)

The most common porphyry deposits are those in which Cu is the most important commodity by value (Cu porphyries). Many of these deposits are located in north side of Chile (Figure 2.2) have concentrations of Mo of up to about 0.03% Mo and/or Au up to 1 ppm, either or both of which can constitute part of the value of the ore (Cu–Mo and Cu–Au porphyries). (Laurence Robb, 2006)

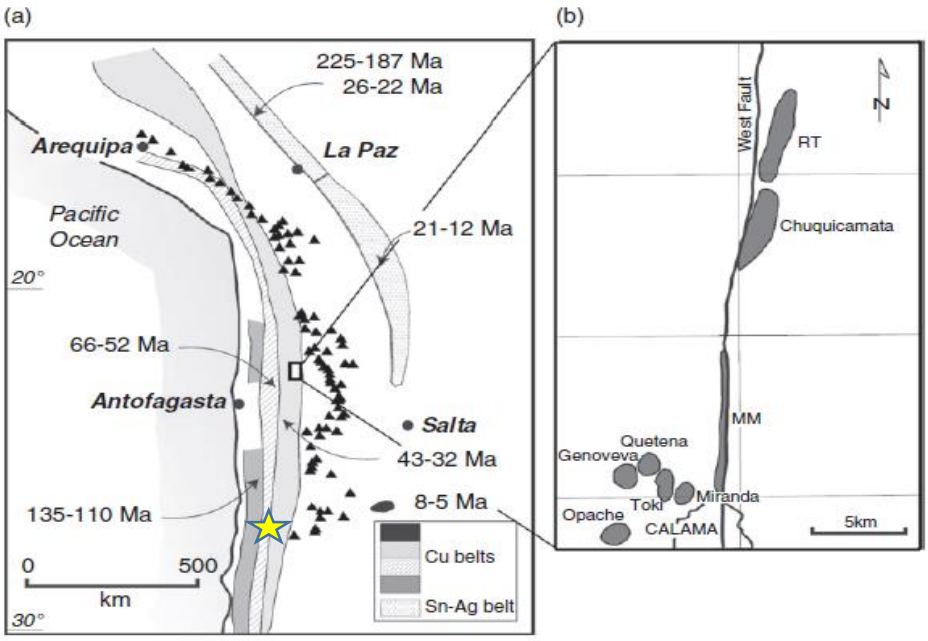

Figure 2.2_ a) Distribution of the most important porphyry deposit of northern Chile. The star indicates the area of study; b) Example of clustering of deposits around one of the most important porphyry deposits in the world (Chuquicamata). (Lowrence Robb,

2.1.1 Alterations

Hydrothermal altered rock are a characteristic component of porphyry deposits. Alteration is pervasive in the ore zones and in adjacent, overlying and underlying rock, in some cases extending kilometres beyond the limits of the ore body (Pirajno 2009).

Up to six alteration types (alteration facies) are distinguished based on the presence of one or, in most cases, combinations of specific and characteristic minerals. The zones are each developed broadly concentrically around and above the porphyry intrusion and ore body. In many deposits, lower-temperature alteration assemblages partially overprint higher-temperature assemblages (Lowell et al. 1970).

- *Potassic*: this facies is ubiquitous and is characteristic of the ore zone and of deeper levels of most deposits, especially of the barren core beneath and in the interior of an ore shell. Essential minerals of the potassic alteration

facies are quartz and one or both of K-feldspar and biotite. These minerals are in many cases part of the primary assemblage of the rocks, especially of felsic rocks, but potassic alteration is recognised where a significant proportion of the K-feldspar or biotite has replaced earlier plagioclase and mafic minerals of, for instance, the host intrusion. Other alteration gangue minerals can be chlorite, albite, sericite, magnetite, anhydrite and pyrite. A high concentration of magnetite is a feature of potassic alteration zones in the core of the ore shell of many deposits. Sub-facies have been mapped in some deposits based on the relative abundance of biotite, K-feldspar and magnetite (Figure 2.3). This type of alteration is the result of metasomatic addition of potassium at high temperatures (450–600 °C).

- *Sodic-calcic*: this occurs in some deposits peripheral to the lower depth limits of the ore zones. Essential minerals are albite/oligoclase, actinolite and magnetite. The facies generally lacks pyrite and is almost never a host to ore. It is considered to be the result of infiltration of saline waters at temperatures of approximately 450 °C.

- *Phyllic*: this alteration facies is, like potassic alteration, ubiquitous in porphyry deposits. Commonly, however, it forms relatively late in the development of the hydrothermal system and often overprints potassic and chlorite-sericite alteration zones, especially the upper and peripheral parts of these zones (Figure 2.3). The late timing of this alteration is documented for instance by sericitic haloes to D-type quartz–pyrite veinlets, which crosscut potassic altered rock and the A- and B-type veinlets associated with potassic alteration. The essential minerals are quartz, sericite and pyrite. These minerals grow over the earlier rock texture in such a way that phyllic altered rock appears bleached and often almost textureless in hand sample. Other gangue minerals can include K-feldspar, kaolinite, calcite, biotite, rutile, anhydrite, topaz and tourmaline. Phyllic alteration occurs at moderate temperatures (200–450 °C) and is the result of a moderately to

strongly acid fluid, such that the metasomatic reactions involve addition of H^+ and dissolution of K, Na, Ca, Mg, Ti, Fe from the rocks (Robb 2006).

- *Chlorite–sericite:* this alteration facies caps the ore zone at some deposits, although it can include ore. It has a characteristic pale green colour. In addition to chlorite and sericite (or illite) minerals such as haematite, pyrite and, in some cases, smectite clays may occur. It forms from similar fluids and at similar temperatures as the phyllic alteration zone, but of slightly lower acidity.

- *Argillic:* this alteration may be developed at relatively shallow levels of the hydrothermal system above and peripheral to the phyllic zone. Essential minerals are clays, dominantly montmorillonite (intermediate argillic) or kaolinite (advanced argillic). Other minerals include biotite, illite, chlorite, pyrophyllite, diaspore, alunite, sulphides, quartz and andalusite. Argillic alteration is the result of intense low-temperature metasomatism (100–300 °C) in which clay minerals are produced because of acid leaching of feldspars and mafic silicates.

- *Propylitic*: this alteration is very ubiquitous and is extensively developed around most porphyry deposits, and can extend up to several kilometres from the deposits with progressively decreasing intensity away from the ore body. Propylitic alteration assemblages closely resemble those of greenschist-facies metamorphism. Essential minerals are epidote, chlorite and calcite. Pyrite is normally present. Other minerals include iron oxides, sericite and apatite. Propylitic alteration is the result of addition of H_2O, CO_2 and, in many cases, S_2 to the host-rocks without significant acid–base metasomatism or addition or leaching of metals at temperatures of about 250–400 °C.

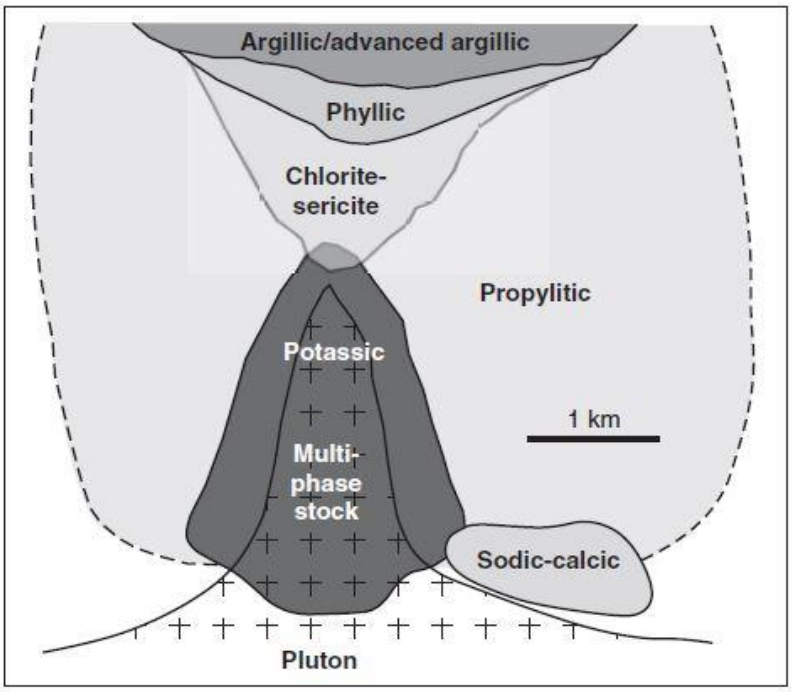

Figure 2.3_ Schematic cross section through a porphyry deposit showing an idealised distribution of different alteration facies (Ridley. 2013).

2.1.2 Breccia pipes

Breccia pipes are present in some porphyry deposits and they may comprise part of the ore. Their shapes suggest that they formed in a similar way as diatremes in kimberlites, during venting of magmas or fluids to the surface. Others are collapsed breccias that may develop on emptying of a magma or fluid-filled space at depth (Burnham 1985).

The production of an exsolved H_2O fluid within a magma is, however, also accompanied by the release of mechanical energy, since the volume per unit mass of silicate melt plus low-density H_2O fluid is greater than the equivalent mass of H_2O-saturated magma (Burnham 1985). At shallow levels of the crust, the volume change accompanying H_2O fluid production may be as much as 30% (at a total pressure of 1 kbar). This results in over-pressuring of the magma chamber and can cause brittle failure of the surrounding rocks. The hydrofracturing that results from this type of failure forms high-angle fractures, because expansion of the rock mass takes place in the direction of least principal stress, which is usually in the

horizontal plane (Sillitoe at al 1971) . Hydrofractures tend to emanate from zones of H_2O fluid production in the apical portions of the granite body and may propagate into the country rock and even reach the surface. Volatile saturation, bubble vesiculation, and rapid cooling are the main factors that help to promote brittle failure in high-level granite-related ore forming systems (McCallum 1985)

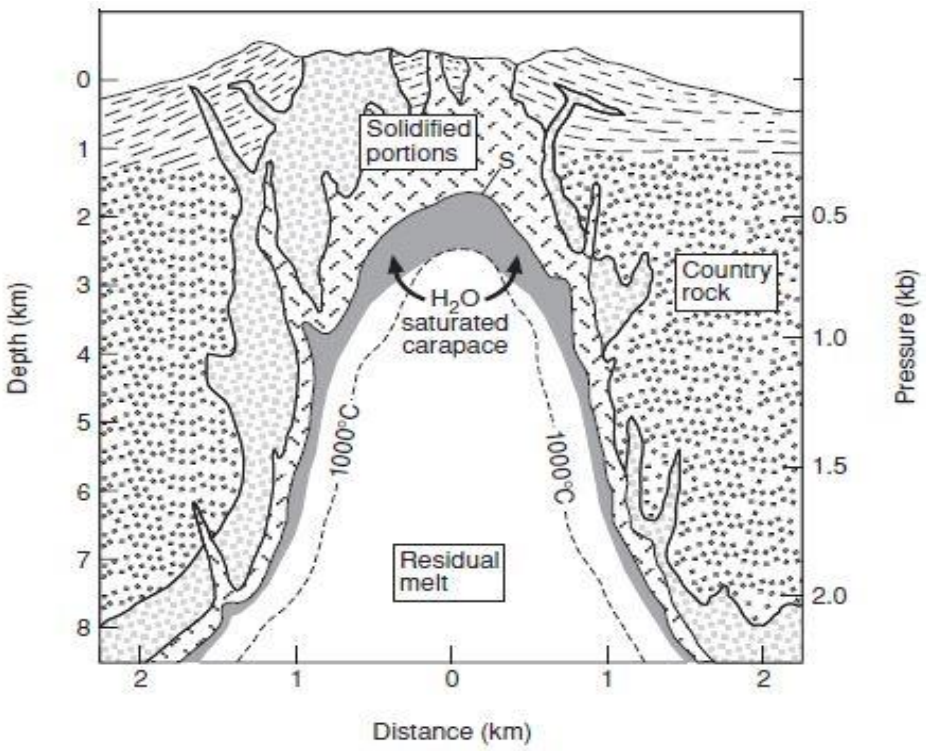

Figure 2.4_ Section through a high-level granodioritic intrusion undergoing progressive crystallisation and showing the hypothetical position in space of the H2O-saturated granite solidus (S), as well as the zone (in grey) where aqueous fluid saturation occurs in the residual magma (after Burnham 1979).

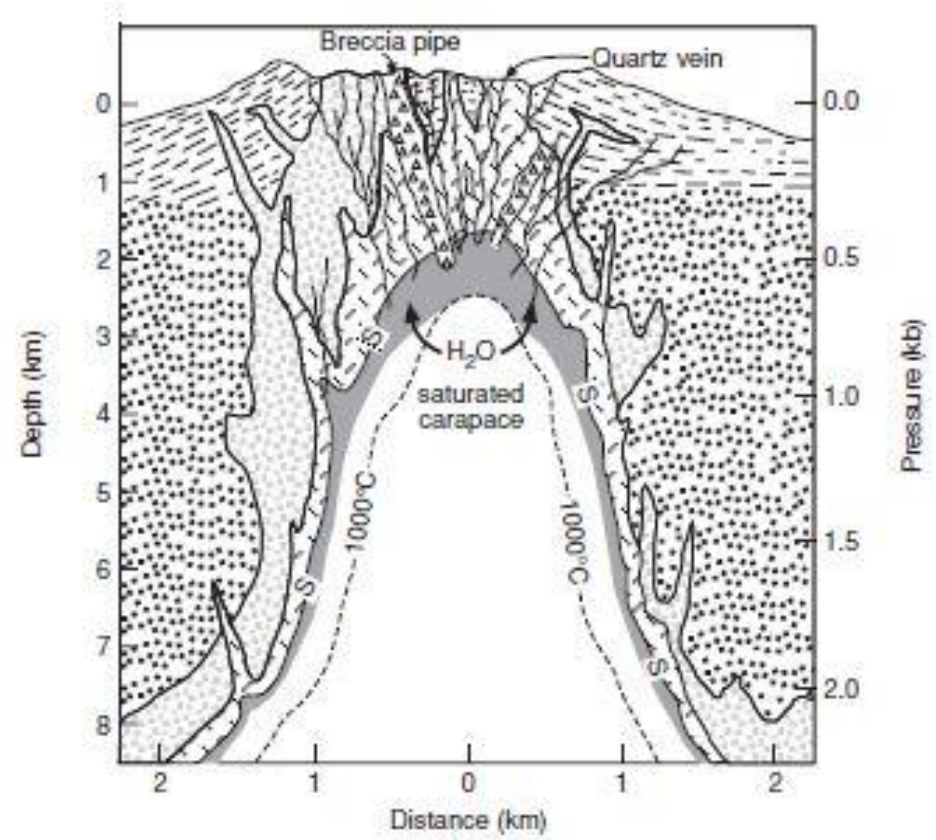

Figure 2.5 Section through a high-level granodioritic intrusion showing the nature of hydrofracturing and breccia pipe formation that could form around the apical portion of a granite body (after Burnham 1979).

2.2 HIGH-SULPHIDATION EPITHERMAL DEPOSITS

High-sulphidation epithermal deposits are Au or Au–Cu deposits with by- or co-product Ag, which are hosted in intensely altered rocks, in most cases in intermediate to felsic volcanic or high-level intrusive rocks, including lavas and pyroclastic rocks (Hedenquist 2000) The forming environments of most of the geologically young deposits are located at about 1.5 km depth and less than 2 km away from a volcanic centre, active in the same period of time of the mineral deposition.(Hart at al. 2005) Some typical settings are inside calderas or under lava domes and central craters of volcanoes with intermediate or felsic lavas. Phreatic breccia pipes, which splay upwards, are a common host of some ore bodies or part of them (Sillitoe at al. 1971).

Some of the most important Au producing region of the central Andes are located in Chile (Figure 2.6). They are the world-class Au-Ag-Cu high-sulphidation epithermal deposits of El Indio (Chile), Tambo, Pascua (Chile), La Coipa (Chile) and Veladero (Argentina), with a total resource of 1358 t of Au, 28746 t of Ag and 2 Mt of Cu (Laznicka 2006).

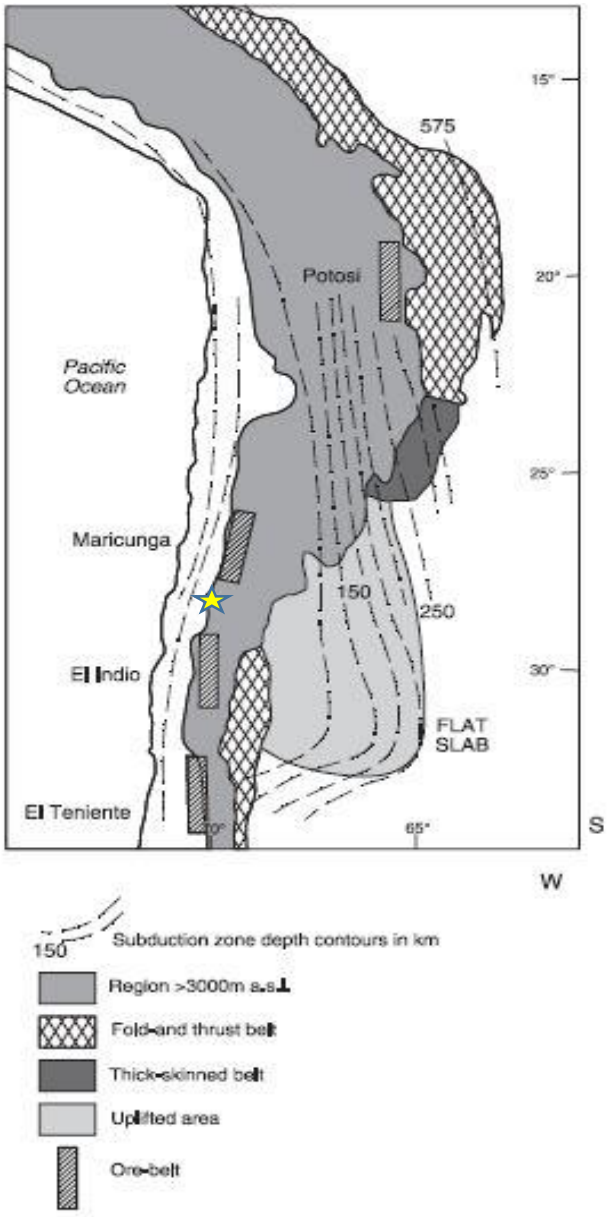

Figure 2.6_Distribution of main ore belts in the central Andean region (Ridley,2013). The star indicates the location of the area studied in this work.

2.2.1 Alterations

Temperature, pressure, type of rock, nature of circulating fluids and water/rock ratios are the factors that drive the development of the different alteration mineral assemblages in hydrothermal systems. Hydrothermal alteration in epithermal systems may be related to interaction with acid-sulphate fluids, near-neutral chlorinated fluids, or alkaline fluids (Ridley 2013). These different fluids typically produce distinct alteration assemblages (Figure 2.8). The recognition of these mineral assemblages is thus fundamental to understand the different types of epithermal systems and a guide exploration programmes.

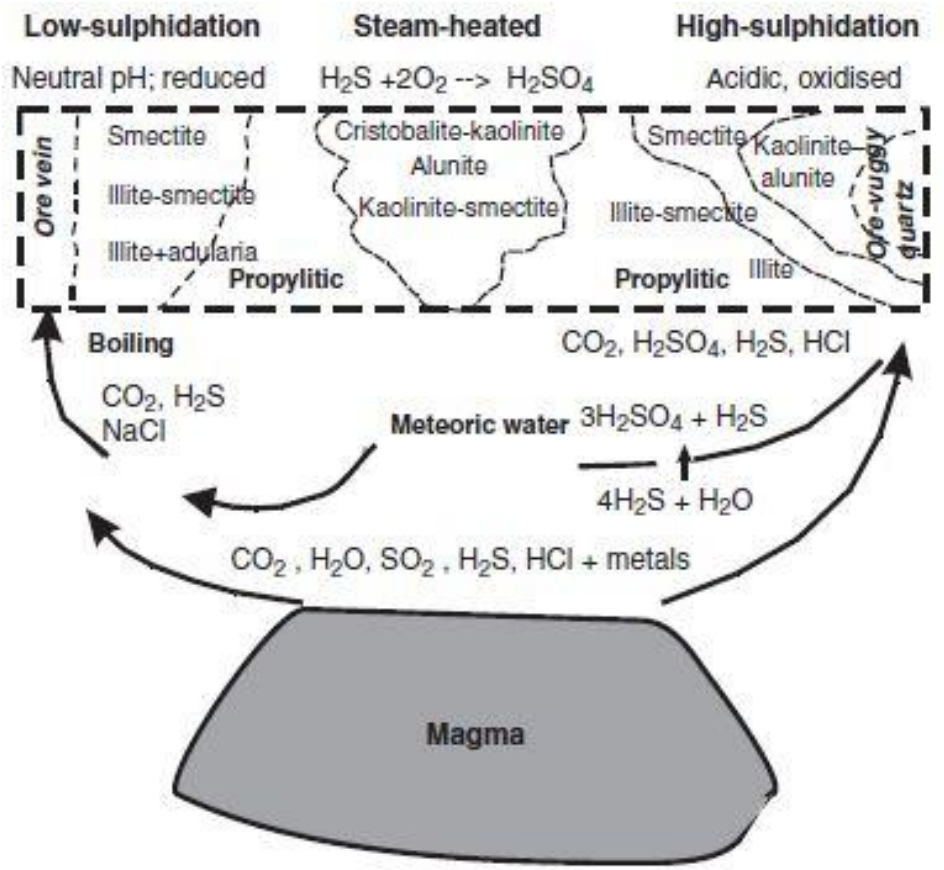

Figure 2.7 Figure 2.8_ Simplified scheme of the distribution of hydrothermal minerals in low- and high-sulphidation epithermal systems; steam-heated alteration can occur in both types, but it is especially common in low-sulphidation systems, where silica sinters develop where hot springs discharge. After Hedenquist et al. (1996)

The first peripheral alteration zone is constituted by smectite to the surface and illite at depth. These minerals form the intermediate argillic alteration and their

presence indicates that acidic fluids were passed throw the rocks. At lower temperature, the mineral phases related to acid-sulphate fluids, which are characteristic of high-sulphidation systems, are kaolinite, alunite, cristobalite, gypsum, opal, native sulphur, quartz and sulphides. Pyrophyllite, diaspore and andalusite may form at temperatures in excess of 250°C. Barite, anhydrite and hydrated Fe oxides may also be present in the lower temperature range.These mineral assemblages constitute what is known as the *advanced argillic alteration*. The central ore zone of most high-sulphidation epithermal deposits consists of porous to massive quartz-rich (up to 95%) rock. In this type of alteration, known as *vuggy silica*, the hydrothermal fluids have leached all major chemical components of the rock other than silica. Primary volcanic quartz phenocrysts may be distinguished from the secondary fine-grained quartz that crystallised from the silica component of leached matrix minerals, for instance feldspars. In general, however, primary rock textures are not preserved. Millimetre- to centimetre-sized vughs are scattered throughout the altered rock and comprise up to a few per cent of the rock. These voids formed during alteration as a result of overall leaching of the rock.

Summing up, moving from the central area to the peripheral one of high-sulphidation epithermal systems, it is possible to observe the following alteration zones: vuggy silica, advanced argillic, and intermediate argillic. (Figure 2.9).

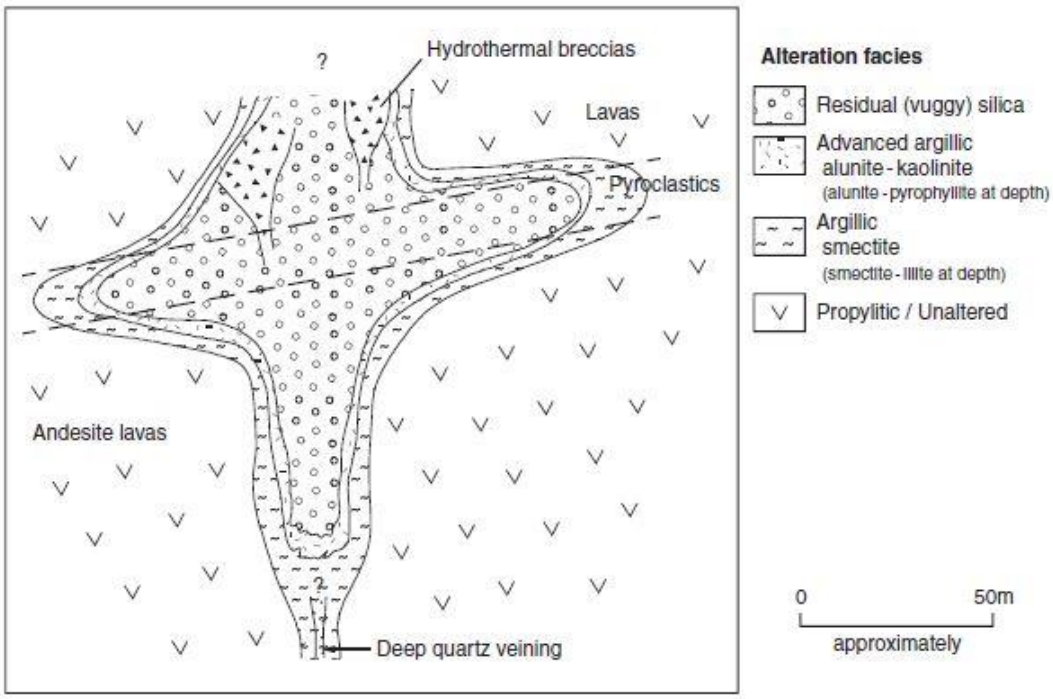

Figure 2.9_ Alteration halos in a typical high-sulphidation epithermal system (Ridley,2013).

2.3 POLYMETALLIC VEINS

A large number of small, mainly historic mines exploited veins in and around magmatic centres. Many vein fields are well-defined clusters of veins spread over several kilometres, separated by altered but unmineralised rock or by unaltered rock. These veins mark a different style of fluid migration from magmatic centres than porphyry and epithermal deposits. Many are polymetallic and have economic grades of one or more of the metals Sn, W, Mo, Bi, U, Au, Ag, Cu and Zn (Hart and Goldfarb 2005). In some ore camps, they overprint porphyry ores, but may be significantly more extensive, such as at Main Stage Veins at Butte, Montana, USA (Meyer et al. 1968) and at Morococha, Peru (Catchpole et al. 2011). Other examples are peripheral to either greisens or porphyry deposits (e.g., tin mining districts of Cornwall, UK) or occur around magmatic centres which lack known porphyry or greisen deposits (e.g., Idaho Springs – Central City district of Colorado, USA, Rice et al. 1985). Hydrothermal fluid in these vein fields is in

most cases dominantly a magmatic-hydrothermal fluid, although it may contain varying proportions of in-mixed meteoric waters. Fluid cooling and evolution of the fluid composition because of interaction with wall-rocks, and mixing of the metal-carrying fluid with other fluids are the possible cause for a large-scale metal zonation in vein fields. (Ridley 2013) Different vein fields appear to have formed from different phases of fluid migration. Fluid phase separation is recorded in a huge number of fields, but in the same fashion as in porphyry deposits it may not be a critical factor promoting ore mineral precipitation. Mixing with groundwaters will in general be most important at the outer edges of the vein field and during the later infill stages of the veins.(Robb 2006)

3 REMOTE SENSING DATA

3.1 ASTER DATA

Aster (Advance Spaceborne Thermal Emission and Reflectance Radiometer) is a multispectral instrument built by a cooperation between EOS (Earth Observing System) – ERDSDAC (Japan's Earth Remote Sensing Data Analysis Center) and NASA-METI (Japan's Ministry of Economy, Trade and Industry) (Abrams and Hook 2002).

Launched on December 18, 1999 in Vandenberg Air Force, California, USA, this satellite orbits the Earth at about 705 km high (synchronous sun) with a period of 98.88 minutes and an inclination of 98.3 degrees compared to the equator. The time resolution is 16 days and crosses the equator at 10.30 am (from north to south). A single ASTER image has a swath of 60 km2 and the scanners are is whiskbroom type.

Figure 3.1_ Aster satellite

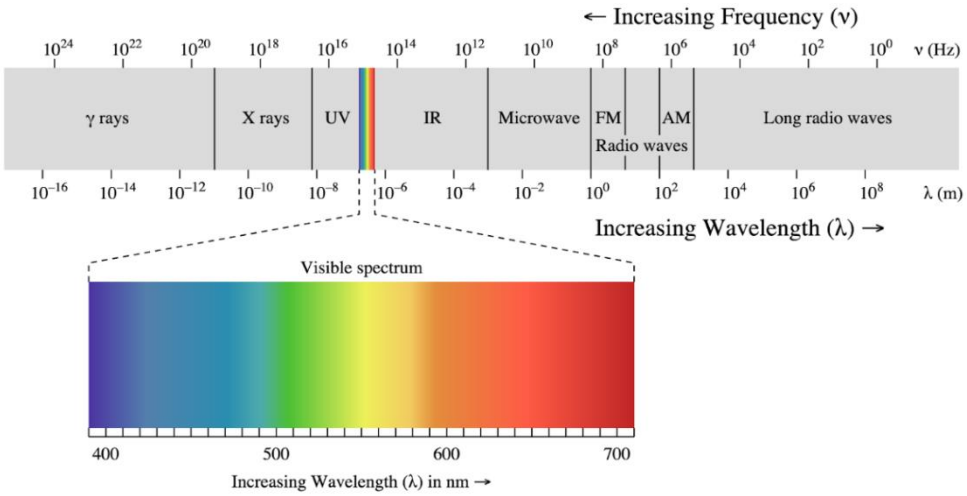

Figure 3.2_Electromagnetic spectrum

Indeed Aster is composed by three spectrometers, which are able to detect informations of radiations reflected or emitted from objects on ground surface in different range of wavelength (tab.2.1). Totally it has 14 bands. Three bands on visible-near Infrared field acquiring in Nadir position (VNIR) and one (band 3B) in a backward view to permit creations of Digital Elevation Models (DEM), six bands on short wave infrared (SWIR) and five on thermal infrared (TIR) (Abrams at al. 2002).

Subsystem	Band No.	Spectral Range (μm)	Spatial Resolution, m	Quantization Levels
VNIR	1	0.52-0.60	15	8 bits
	2	0.63-0.69		
	3N	0.78-0.86		
	3B	0.78-0.86		
SWIR	4	1.60-1.70	30	8 bits
	5	2.145-2.185		
	6	2.185-2.225		
	7	2.235-2.285		
	8	2.295-2.365		
	9	2.360-2.430		
TIR	10	8.125-8.475	90	12 bits
	11	8.475-8.825		
	12	8.925-9.275		
	13	10.25-10.95		
	14	10.95-11.65		

Table 3.1_ Characteristics of the Aster sensor

As reported in the ASTER user manual, the instrument produces two different Level 1products: Level-1A (L1A) and Level-1B (L1B). ASTER L1A data are defined as reconstructed and unprocessed instrumental data at full resolution wit headers containing radiometric and geometric coefficients for image calibration. The L1B data are already radiometrically and geometrically corrected.

The file used in this work is a ASTER Level 1 Precision Terrain Corrected Registered At-Sensor Radiance data (L1T) and was downloaded from Earthexplorer.usgs.com. ASTERL1T corresponds to a L1B ASTER file that has been geometrically corrected and rotated to a UTM north-up projection. The precision terrain correction incorporates ground control points with a digital elevation model to achieve topographic accuracy for all daytime scenes where correlation statistics reach a minimum threshold, with alternate levels of correction possible for scenes acquired at night or that otherwise represent a reduced quality ground image (e.g. cloud cover).

Differences between three type of Aster files ASTER L1T, ASTER 1B and ORTHORECTIFIED ASTER are summarised below. (https://lpdaac.usgs.gov/dataset_discovery/aster/aster_products_table/ast_l1t)

- ASTER Level 1B at-sensor radiance is in a path-oriented projectionas opposed to the north-up UTM projection available in both the ASTER Level 1T and ASTER Orthorectified products.
- ASTER Level 1B images dimensions for each of the three sensor subsystems (VNIR, SWIR, and TIR) remain constant from one scene to the next, but the ASTER Level 1T and ASTER Orthorectifed image dimensions vary by scene because of the rotation process.
- ASTER Orthorectified at-sensor radiance is produced using proprietary software, an ASTER derived digital elevation model and ground control points, whereas the ASTER Level 1T uses the GLS2000 digital elevation data, and derived ground control points with Land Processes1 Distributed Active Archive Center (LPDAAC).

- The ASTER Level 1T is a multi-file product generated with a single resampling from the ASTER Level 1A input scene to provide, full resolution imagery, and an independent geometric verification report with browse in addition to standard metadata

Figure 3.3_Earth observation satellite.

3.2 HYPERION DATA

The National Aeronautics and Space Administration EO-1 satellite (Figure 3.3) was launched the 21st of November 2000 as part of a one-year technology validation/demonstration mission. After this period, considerable potential of this sensor was noted for environmental studies, with the decision to prolong the mission. After 16 plus years of EO-1 science observations the NASA has been determined that, it was time to finish it.
https://archive.usgs.gov/archive/sites/eo1.usgs.gov/index.html

On February 22nd, 2017, the Earth-Observing One (EO-1) satellite will be decommissioned. The Hyperion historical data will continue to be available through Earth Explorer (EE) https://earthexplorer.usgs.gov/ for the foreseeable future.

Hyperion is a "push broom" high-resolution hyperspectral-imaging instrument that can image a 7.5 km by 100 km land area per image, and provide detailed spectral mapping across 220 bands from 400 nm to 2500 nm, with ground resolution of 30 m. (Figure 3.4)

Specification Item	Performance Measurements
GSD	29.88 m
Swath	7.5 km (0.61 degrees TFOV)
Spectral coverage	VNIR: 400 - 1000nm SWIR: 900 - 2500nm
Imaging aperture	12.4968 cm (4.92 in.)
VNIR SNR 550 - 700nm	144 - 161
SWIR SNR 1000 - 1050nm	90
SWIR SNR 1200 - 1250nm	110
SWIR SNR 1550 - 1600nm	89
SWIR SNR 2100 - 2150nm	40
On-Orbit life	1 year
IFOV	42.4μrad

Figure 3.4_Caracteristic of Hyperion sensor.

A multispectral sensors have just few bands so, the resulting spectral resolution is less accurate (Figure 3.5). It has a single telescope and two spectrometers, one visible/near infrared (VNIR) spectrometer and one short-wave infrared (SWIR) spectrometer.

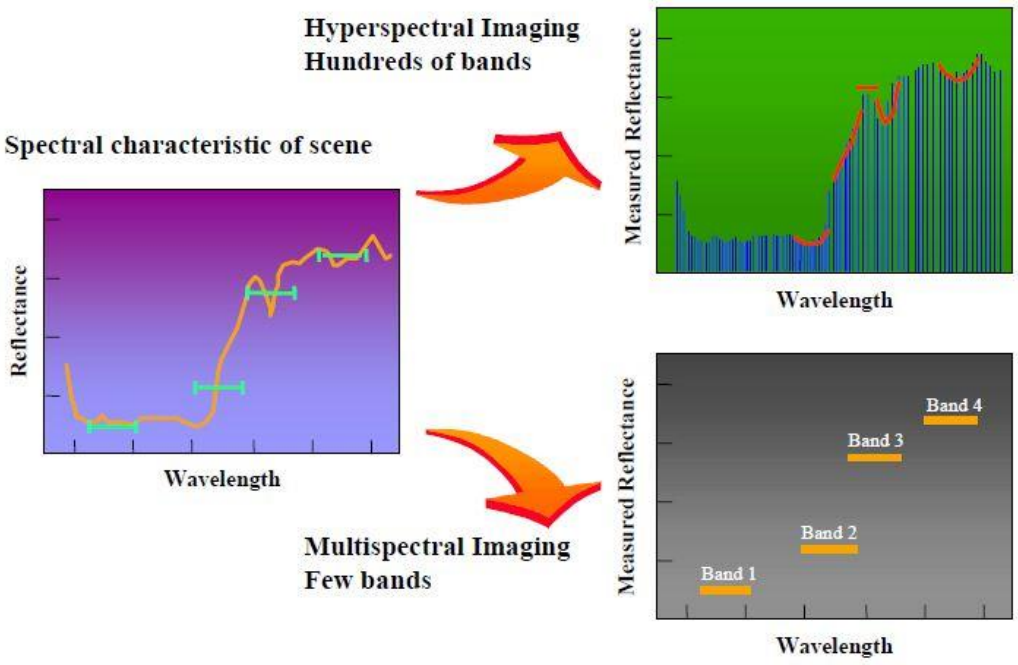

Figure 3.5_Difference between hyperspectral and multispectral sensor

Hyperion data are provided in the following format (https://lta.cr.usgs.gov/ALI)

- Level 1Gst is terrain corrected and provided in 16-bit radiance values. The data are available in Geographic Tagged Image-File Format (GeoTIFF) and are distributed via download at no charge through either EarthExplorer or GloVis. The Level 1Gst product will also include terrain correction through use of a digital elevation model (DEM). This addition corrects parallax error due to topographic relief and improve the overall band-to-band registration accuracy. The elevation data used for correction consist of the Shuttle Radar Topography Mission (SRTM) "Finished" data set and other elevation data as required.

- The Level 1R data set consists of radiometrically-corrected images (watts/(sr-micron-m2)x100), formatted as HDF files, and metadata in binary and ASCII formats. Level 1 metadata filenames have an extension attached which indicates the intermediate Level 1 process (e.g., after smear correction, echo correction, dark subtraction) from which the file

was generated, although the intermediate files themselves are not included on the tape.

- Hyperion Level 1T (L1T) consist in a level 1Gst file but with systematic geometric corrections incorporating ground control points L1T scenes are provided in GeoTIFF format.

4 ASTER DATA PROCESSING

Preliminary studies were conducted using the remote sensing analysis in a 1T level Aster file (Aster L1T), using ENVI software, version 5.3, to process the images. This program is able to create new customized images by combining the different spectral bands of the original file.

By sharing information with the professors Karl Riveros and Miguel Càceres of the University of Atacama it was possible to understand and interpret the results of the first elaborations. The geological maps used for the framing of the area were the maps Los Loros and Hoja la Guardia provided by the National Service of Geology and Mining of Chile in 1:100000 scale.

During this work the following processes were performed:

- Radiometric calibration of the Aster L1T image in HDR format;
- False colour composition of the spectral band;
- Band ratios analysis in the spectral bands of the visible range, near infrared and short waves infrared (VNIR / SWIR).
- Principal component analysis (PCA) using spectral band of the visible, near infrared and short wave infrared (VNIR / SWIR).

4.1 RGB ANALYSIS

The most common RGB association using ASTER data is 731, which corresponds to thev742 composition of Landsat 7ETM This output gives a general geologic informations of the area. The choice of band 7 was made in order to highlight the Al-OH absorption of white mica and clays and the Mg-OH absorptions of

phyllosilicates, amphiboles, and epidote. Fe crystal field absorption and high reflectance by vegetation cover are recorded by band 3. Band 1 is representative of charge transfer of Fe ions in phyllosilicates, amphiboles, pyroxenes, and ferric oxides (Koziol et al. 2018)

In Figure 4.1 it is possible to see different zones that represent a first spectral distinction. The blue colour represents the most basic rocks in the area that are basalts and andesite. The grey area detect very well a formation called Grava de Atacama, constituted of unconsolidated gravel of heterogenic compositions. The red zone instead, highlighting the phyllosilicates such as muscovite, biotite but also montmorillonite, and illite may show acid volcanism or hydrothermal alterations. The white area is difficult to classify without further processing. The absence of a sharp green colour is due to lack of vegetation.

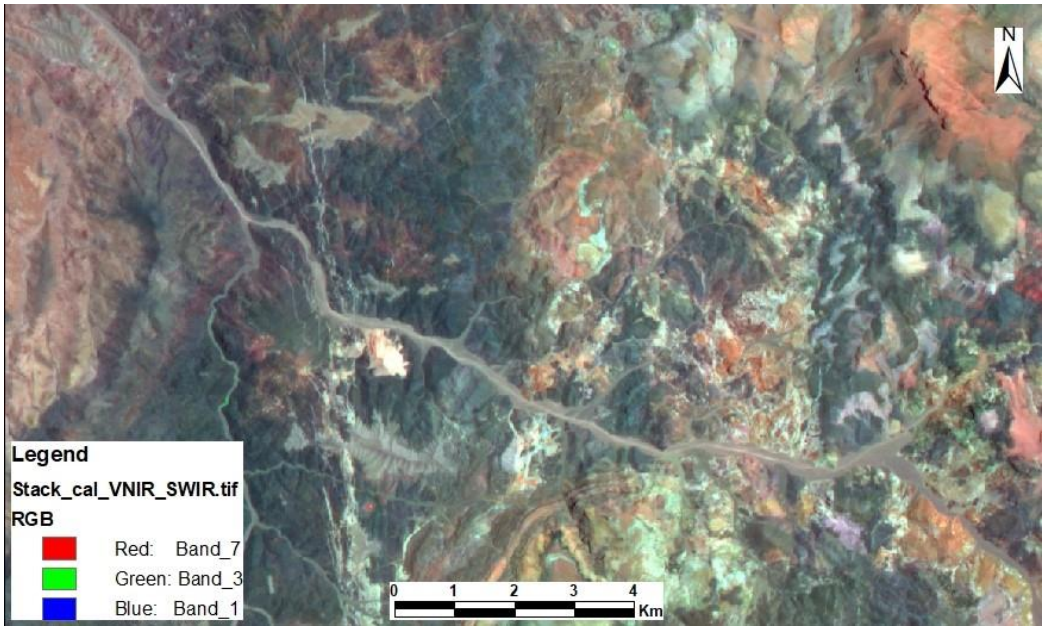

Figure 4.1_Aster image with RGB compositin 731.

4.2 BAND RATIOS ANALYSIS

Many more features can be extracted using band ratios focused on specific absorptions (Bishop et al. 2011). Many specific minerals have been analysed by the predefined spectral library present on ENVI but just a few of them have shown

reliable results. In particular, the composition of false ASTER RGB colours 2/1, 9/3 and (5+9)/8 has been used. (Pour and Hashim 2012)

The (5+9)/8 ratio is important for highlighting the Mg-OH bond stretching specified for chlorite (Figure 4.2-a), but also biotite, epidote, and amphiboles.

The 2/1 and 9/3 ratios were selected for the absorption bands due to Fe charge transfer and crystal field effects, respectively. Indeed resampling a spectral signature according to ASTER spectral resolution, peaks could appear stretched on bigger interval of wavelength respect to the normal spectra because the resulting multispectral signatures have few bands placed in precise interval of wavelength as it is show for the all spectral signatures of hematite, goethite, and chlorite (Figure 4.2-b).

RGB false colour products are shown in Figure 4.3. Blue zone correspond to the basaltic-andesite lava flows of Sierra la Dichosa formation. Green colour detect very well the Cabeza de Vaca granitoid pluton, on the West side and others lithology to the East that correspond to Dacitic-Riolitic tuff-ignimbrites representing the explosive-magmatic phase of Carizallillo caldera (Rivera, et al. 1994). The last colour, Red, shows last phases of caldera's activity, showing Dacitic Domes and dikes injected in the fractures caused by volcano tectonic extensional activity. Furthermore, there are well-detected zones affected by hydrothermal alterations forming limonite gossan visible in greenish – yellow colour in the image.

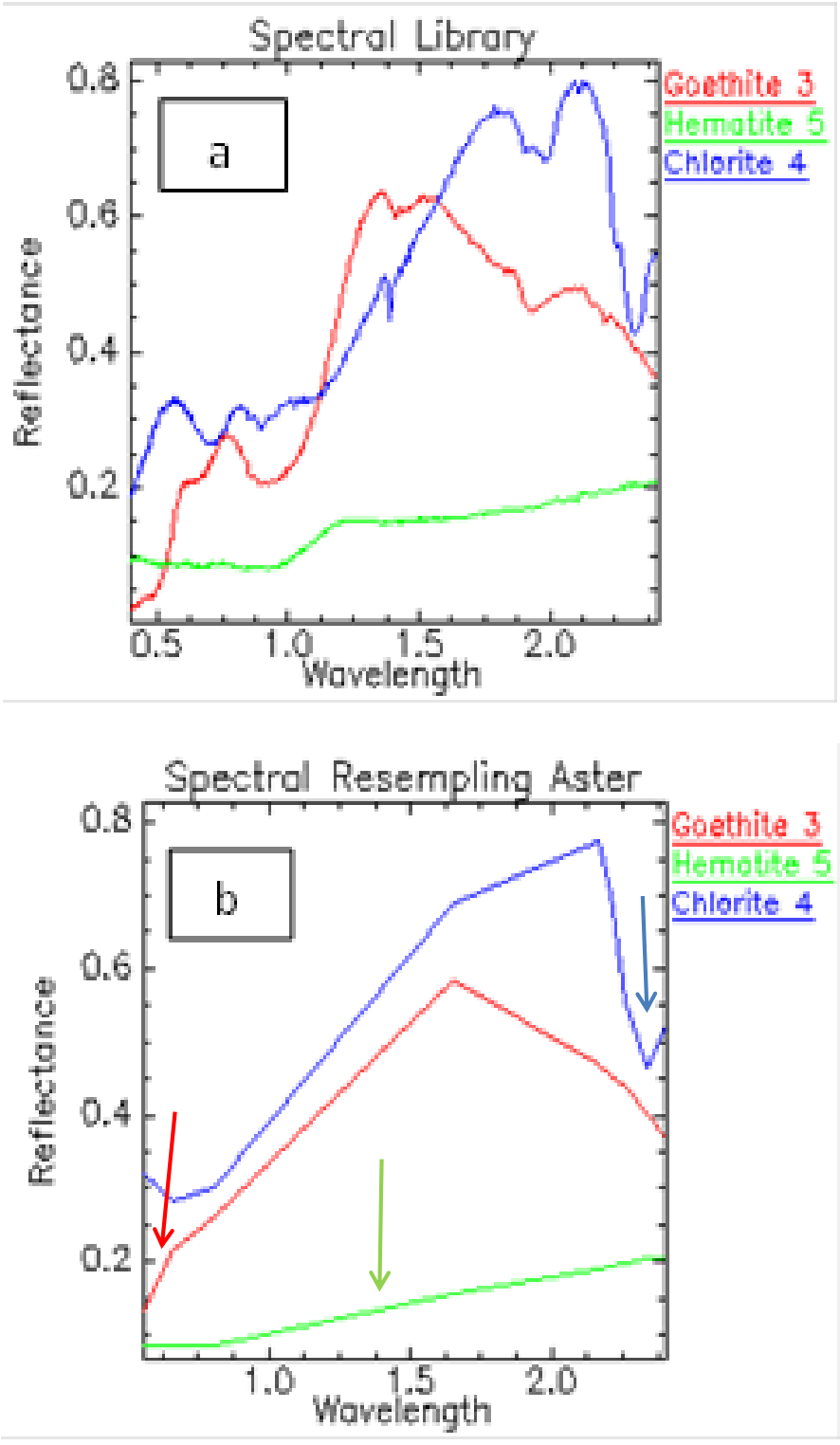

Figure 4.2 a) Complete spectral signatures, between 0.4 and 2.5 µm of the chlorite (blue) and a blue arrow shows the peak of absorption, hematite (green) and green arrow shows the relative peak and finishing the goethite (red) with the respective peak; b) signature resampled according to Aster spectral resolution in the NIR-SWIR interval.

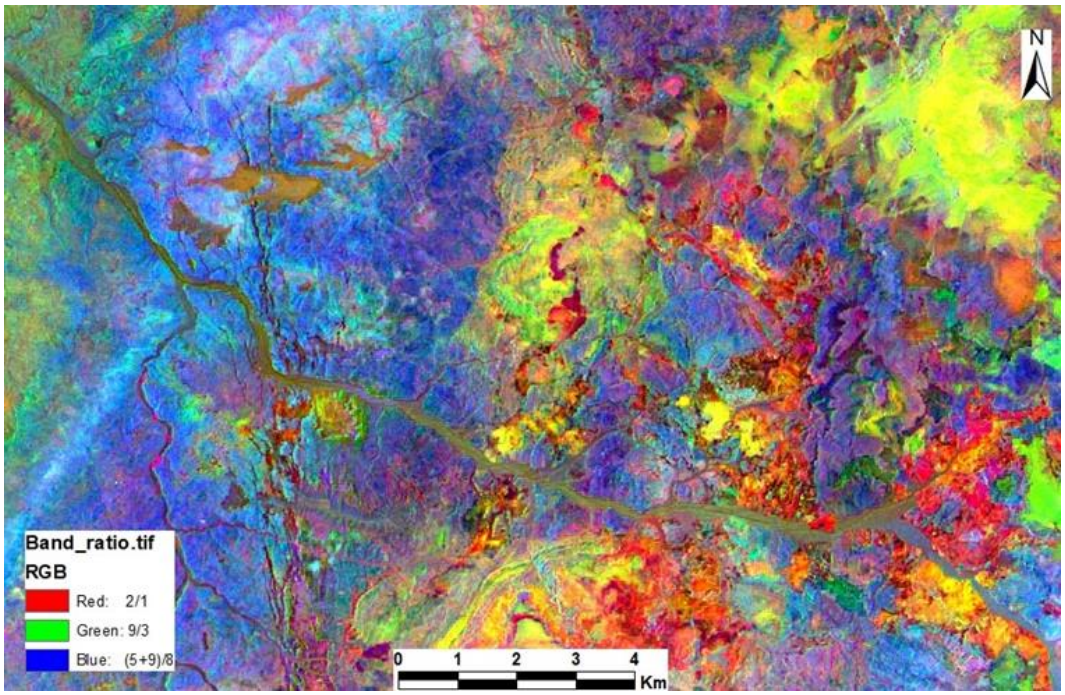

Figure 4.3 Aster band ratio image. Red is associated to 2/1 ratios, green to 9/3, and the blue to (5+9)/8 one.

4.3 PRINCIPAL COMPONENT ANALYSIS

Principal components analysis (PC) has been applied to the whole scene and the PC9, PC7, and PC5 bands were helpful for detecting, mainly, alteration halos associated with faults and fractures (Massironi et al. 2008).

In Table 4.1, PC eigenvectors are presented (Singh and Harrison 1985). PC9 is principally positively loaded by band 2 (+0.65) and negatively by band 1 (−0.72), and reflects the presence of Fe oxides and sulphurs. In contrast, PC7 has a lower negative eigenvector for band 5 (−0.67), which is affected by the Al (OH) absorption characteristic of Alunite, but has a medium positive one for band 6 (+0.43), which reflects OH structure composition of minerals. PC5 is characterized by a value close to zero on band 7 (−0.01), which is located in a peak that correspond to OH absorptions, and a very high positive loading by band 9 (+0.72). In the RGB composites of PC9-PC7-PC5, the altered zones are therefore outlined by green to yellow colour corresponding to the variable content

of hydrothermal minerals and iron oxides (Figure 4.4). Clearly is possible to see a large area affected by alteration, especially in the eastern side of the image. It is possible to distinguish the different alteration grade only making XRPD analysis (see chapter 4). In blue are emphasized the basaltic flow of Lava sierra la Dichosa and violet halos are possible to detect between this unit. All the other lithology are better detected using the processing explained before.

Eigenvectors	Band 1	Band 2	Band 3	Band 4	Band 5	Band 6	Band 7	Band 8	Band 9
PC 1	-0.26507	-0.31462	-0.31462	-0.33876	-0.32943	-0.33477	-0.31699	-0.33791	-0.34316
PC 2	-0.38781	-0.43136	-0.56259	0.219512	0.178555	0.133357	0.274747	0.29092	0.298425
PC 3	0.046768	0.077878	0.077087	-0.20051	-0.46541	-0.57367	0.460278	0.382432	0.20441
PC 4	-0.32782	-0.25058	0.432069	0.691788	-0.12363	-0.33923	-0.13013	-0.1308	-0.00966
PC 5	-0.17922	-0.18458	0.287461	-0.37339	-0.059	0.083122	-0.43067	-0.00687	0.718222
PC 6	-0.31389	-0.38407	0.479	-0.34007	-0.03816	0.356963	0.383254	0.061698	-0.35959
PC 7	-0.14244	0.221326	-0.09375	0.199288	-0.67464	0.473801	-0.26061	0.352902	-0.10068
PC 8	0.034036	0.070508	-0.08363	0.101291	-0.35769	0.243004	0.435937	-0.70963	0.30985
PC 9	-0.71944	0.640746	-0.00586	-0.11504	0.199198	-0.09002	0.070196	-0.07651	-0.00418

Table 4.1_ Eigenvectors values.

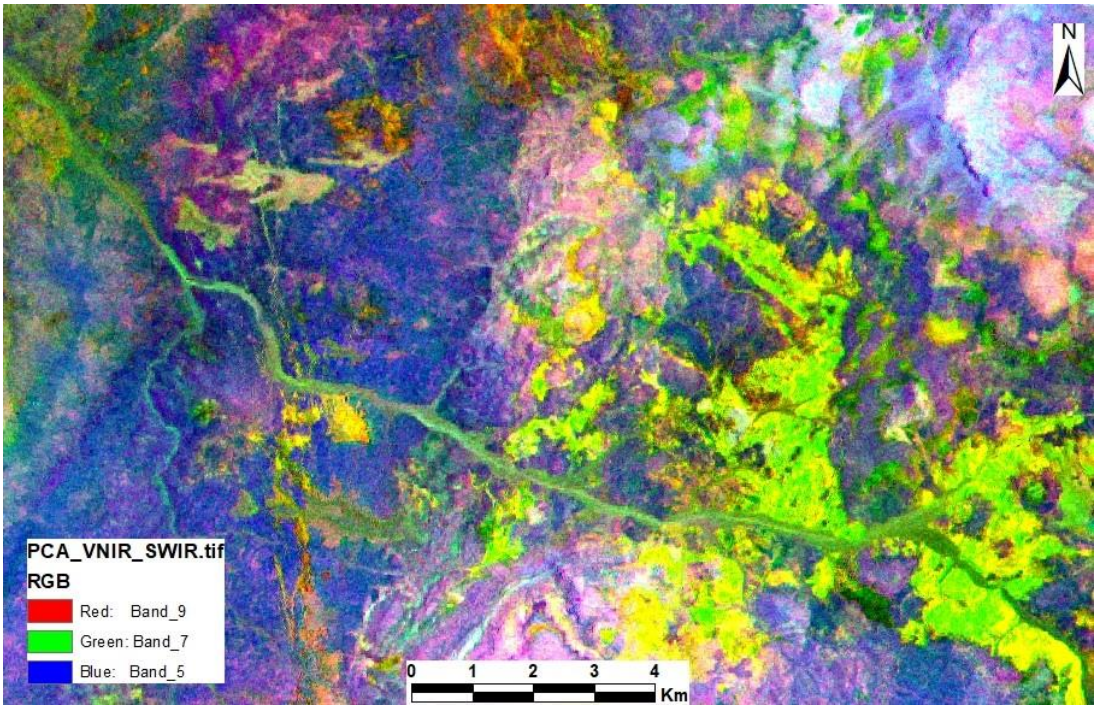

Figure 4.4_ RGB represent PC 975 composition.

4.4 EDGE SHARPENING FILTERS

All the processing steps described above have made possible to identify the main geological units of the area. In many cases, a sharp change in lithology can be interpreted as a structural contact especially in an active geodynamic area.

Structural studies, therefore, have been done using RGB false colour images to see changes in lithology due to tectonic activity and using directional filters to emphasise the morphology. A directional filter is an edge detector that compute the first derivatives of an image. The first derivatives (or slopes) are most evident when a large change occurs between adjacent pixel values, as usually appear acrossfractures. For images, x- and y-directional filters are used to compute derivatives in their respective orientations. Apply a filter to an image, mean to do a matrix operation mathematically. Every process has a different matrix depending to the direction to emphasise (matrices are usually 3x3).

In the following figures, you can see three different directional filters. The first (Figure 4.5), indicates the lineaments with east-west orientation. The second image (Figure 4.6), on the contrary, mainly shows the morphology that extends from north to south.

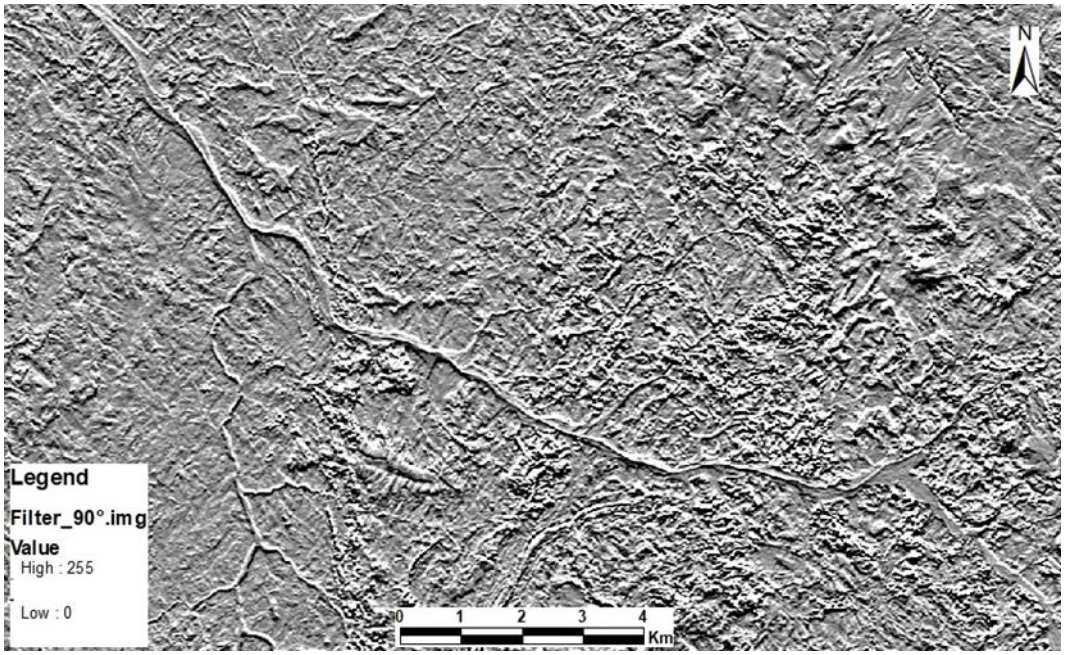

Figure 4.5 Directional filter for Azimut 90°

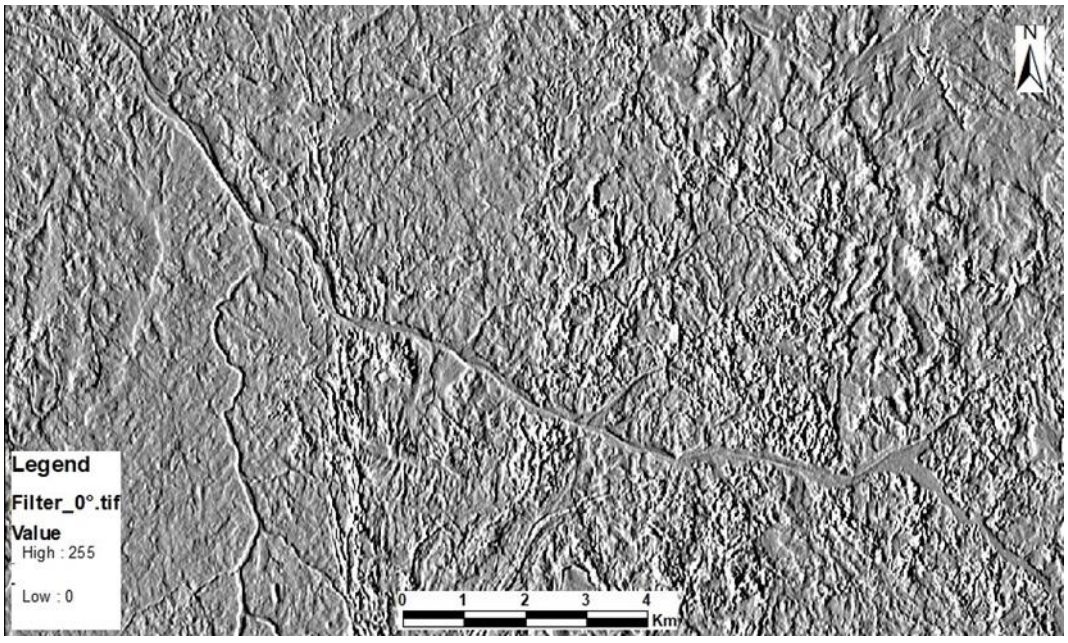

Figure 4.6 Directional filter for Azimut 0

5 GEOLOGICAL MAP

The period spent in Chile lasts from October 2017 until the end of December. Unfortunately, I was granted only fifteen days on the field. Most of the remaining time was spent for remote sensing elaborations, fundamental to organize the fieldwork, and sample analysis. Fifty-two samples were collected and analysed by transmitted light microscopy; this study began in Copiapò and finished in Padova. In addition, X- Ray powder diffraction (XRPD) analyses were carried out on selected samples (in total 12) at the Department of Geoscience, University of Padova.

In total, 130 waypoints were marked using GPS Garmin eTrex 30x (Figure 5.1); they were observation, measurements (yellow spots) and sampling sites (red spots)

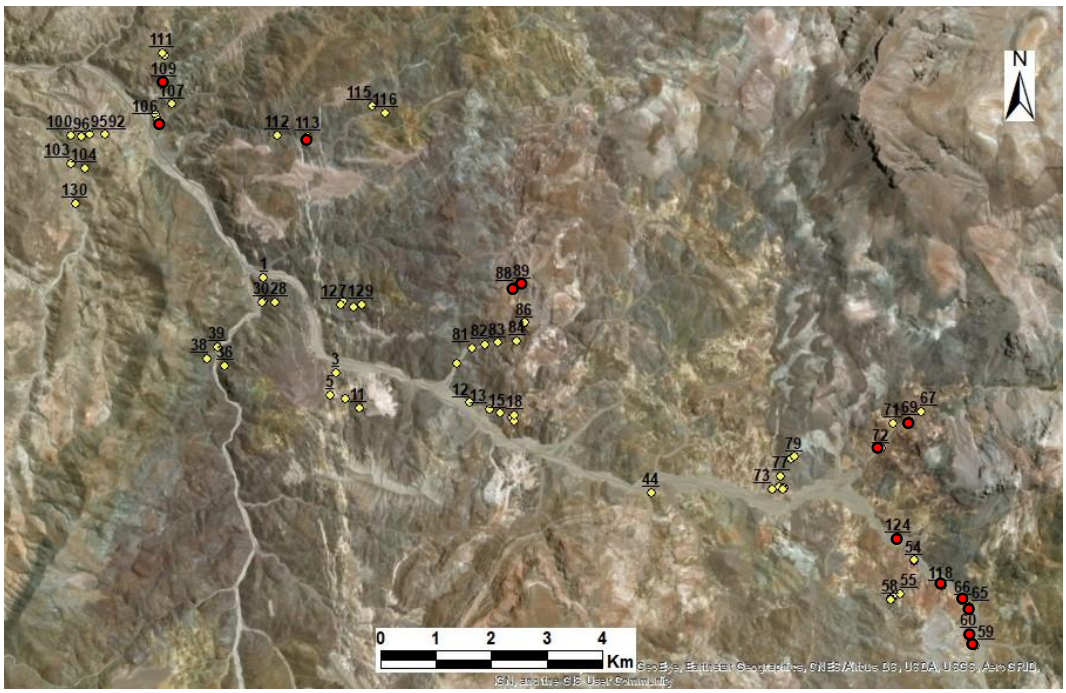

Figure 5.1_ Waypoints taken in the field (yellow spots) and and sampling sites (red spots). The map scale is 1:80000.

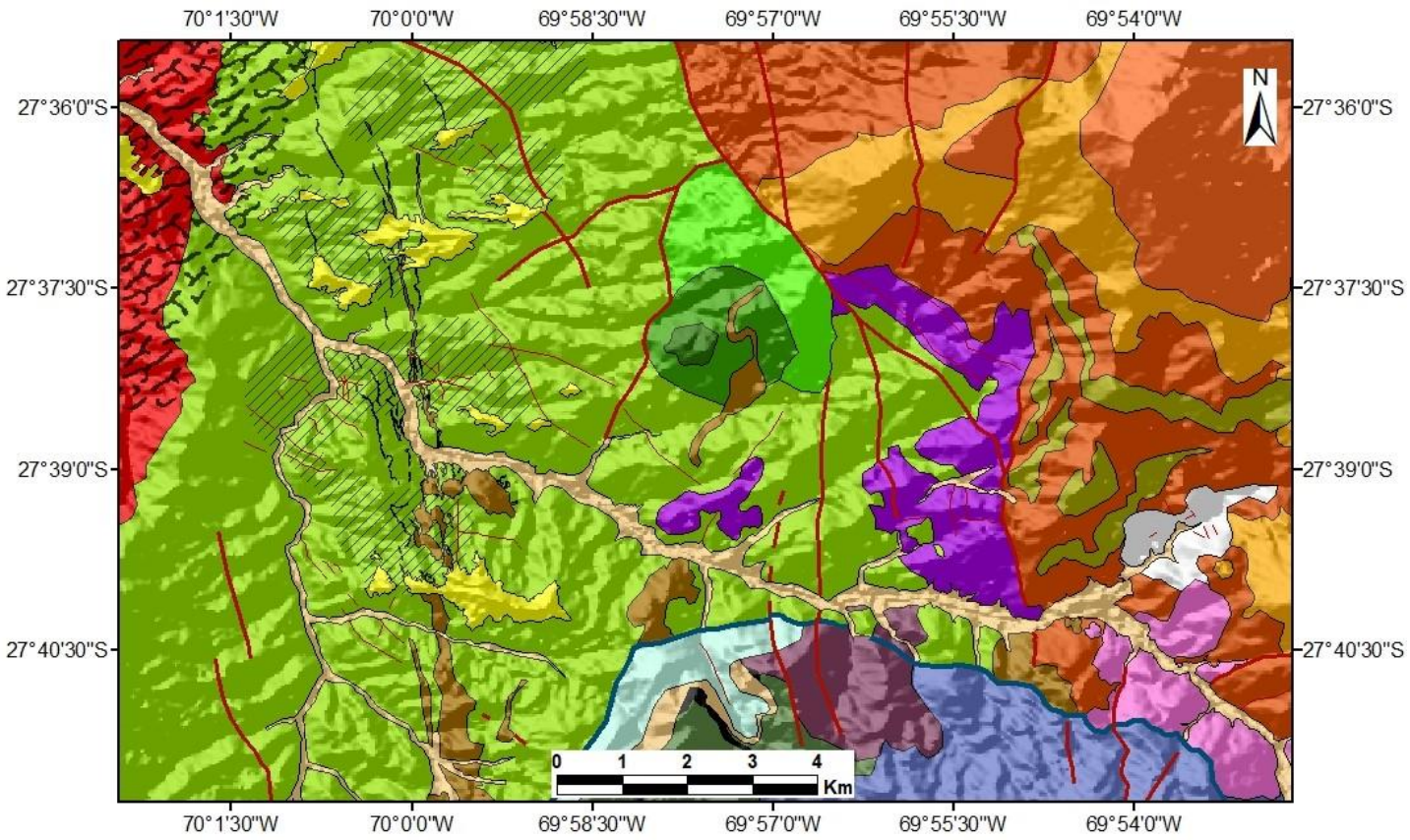

Figure 5.2_Geologic map.

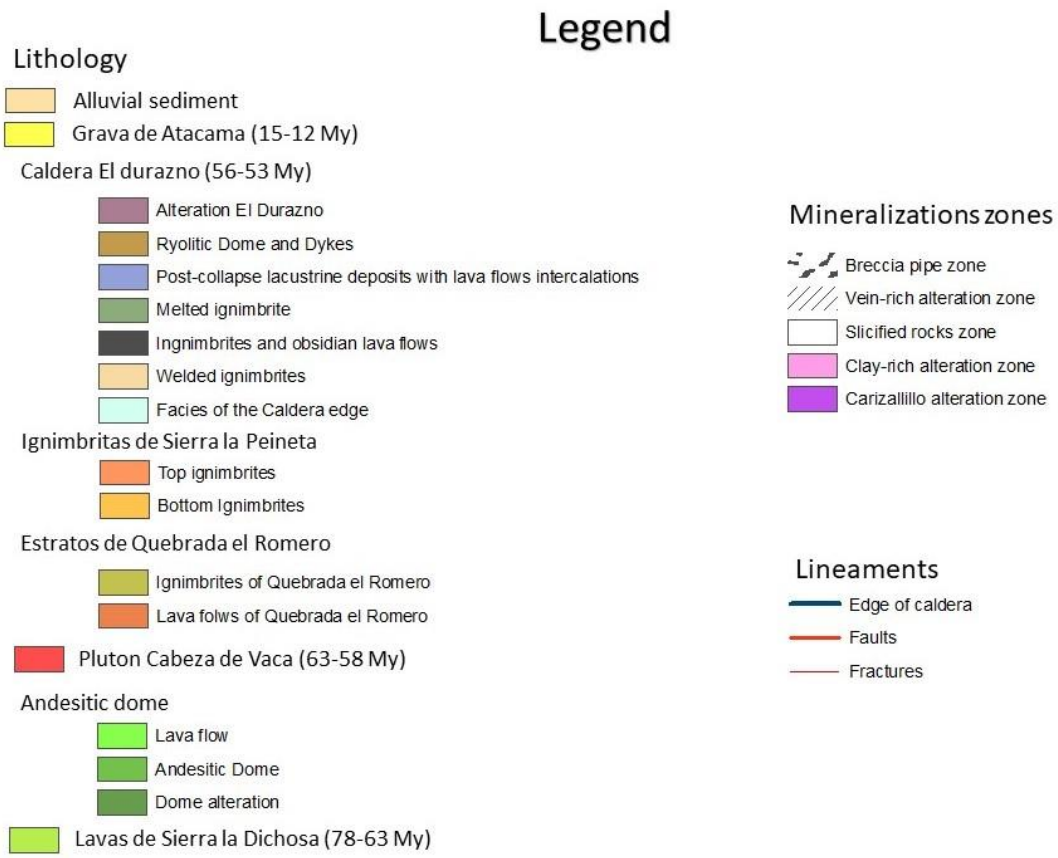

Figure 5.3_legend of geologic map.

5.1 INTRODUCTION

The geological map produced was the result of the combination of bibliographic data, elaborations of ASTER satellite images described in chapter 4 and analysis of collected samples described afterwards.

Bibliographic references were:

- Geological map number 13 in scale 1:100000 provided by Chilean Geology and Mining Service. (Iriarte 1999)
- Geological map resulting from the study of Caldera El Durazno (Díaz-Alvarado, et al. 2016).

The geological map was created using the software ArcGIS 10.5. A geodatabase has been created containing information on lithology, alterations, and structural features of the area. The layout provided in this work is at the 1: 75000 scale.

In the following, all the main geological units and alteration halos as well as the mineralization sites will be presented in detail through macroscopic and microscopic descriptions and on the basis of XRPD data on selected samples.

5.2 LITHOLOGY

5.2.1 Lavas De Sierra La Dichosa

The oldest outcropping formation in the area dates back to the Upper Cretaceous with an age of 78-63 Ma and corresponds to the Lavas de Sierra la Dichosa (Rivera, et al. 1994). This is a volcanic sequence with a total thickness of 800 meters formed by lava flows (Figure 5.4) between 7 and 20 meters thick. The composition of these flows is mainly basic and varies from basalt to trachy-basaltic (45-52% SiO_2) (Rivera et al. 1994). The lava flows are porphyric with phenocrysts of plagioclase and pyroxene, in a pilotaxitic to intersertal groundmass, with grains of olivine altered to iddingsite, bowlingite and chlorite. In subordinate forms, intercalations of breccias, ignimbrites, conglomerates and red sandstones can occur (Arevalo 1994).

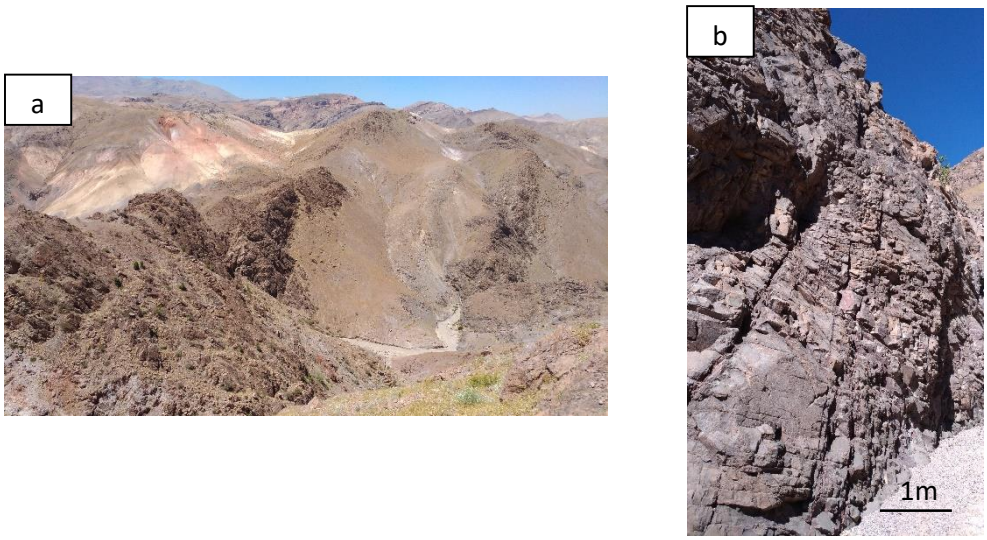

Figure 5.4_ a) View of lava flows in the formation Lavas de Sierra la Dichosa.Wpt. 82 b) Outcrop of lava flow. Wpt. 82

5.2.2 Andesitic Dome within Lavas De Sierra La Dichosa Formation

During the remote sensing analysis, a distinct body within the Lavas de Sierra la Dichosa formation was found thanks to its different colours in both the ASTER 731 (Figure 5.5-b) and band ratios composition red: 3/1, green: 9/3, blue: (5+9)/8 (Figure 5.5 -c).

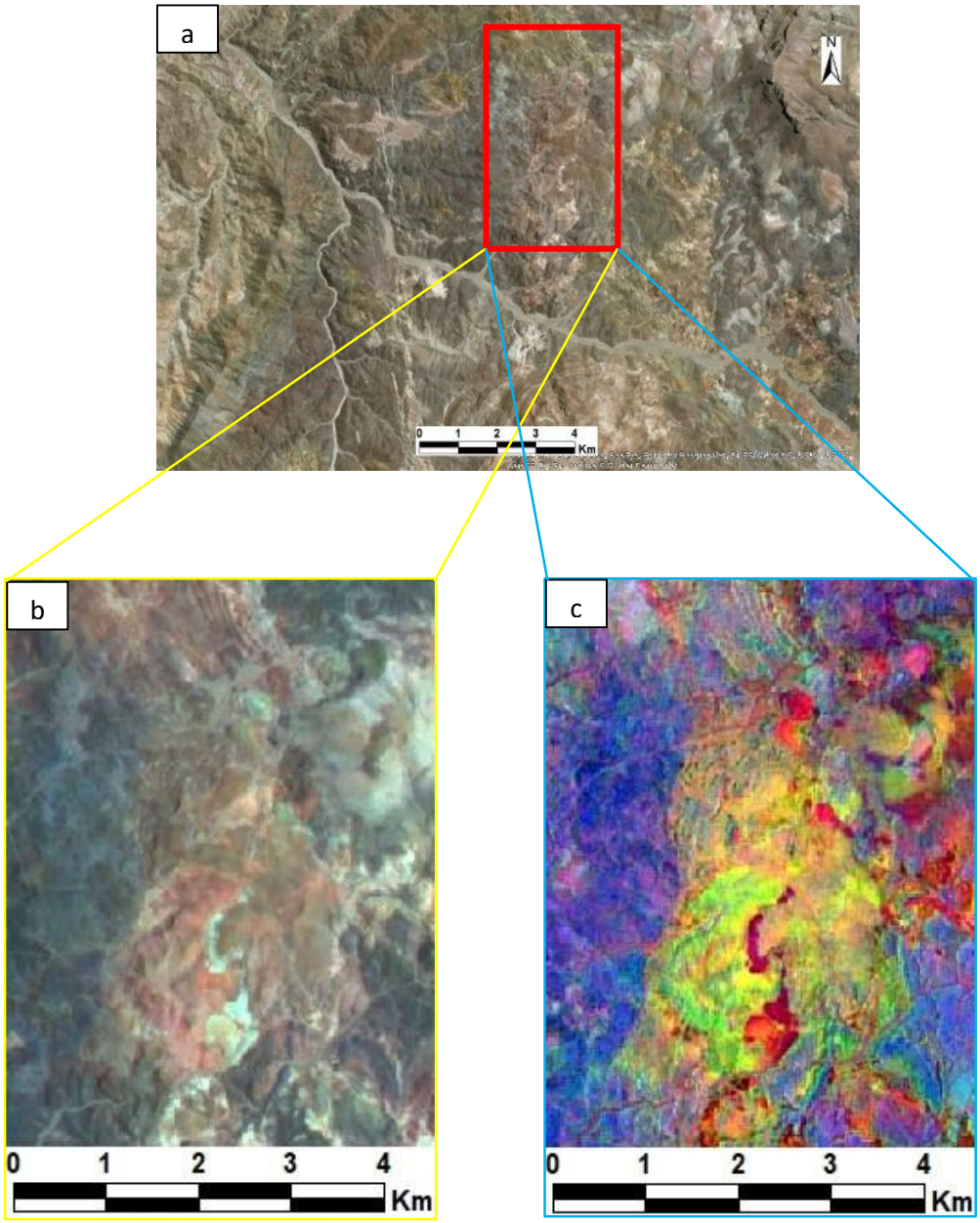

Figure 5.5_ a) Basemap of ArcGIS software show the dome area (red rectangle) on visible wavelength; b) ASTER RGB composition 731; b) ASTER RGB band ratio composition red: 3/1, green: 9/3, blue: (5+9)/8.

The microscope and XRPD analyses have shown that the distinct body is an andesitic dome associated to lava flow of the same composition in its basal part. The dome has shown both a pristine facies (e.g. sample P1 in

Figure 5.6-a) and an altered one (e.g. sample P2 in

Figure 5.6-c). The main difference between the two samples, as also the XRPD analysis shows (Figure 5.7and Figure 5.8), is the replacement by iron oxides of the mafic minerals, such as amphiboles and pyroxenes, in sample P2. However, feldspars remain unaltered.

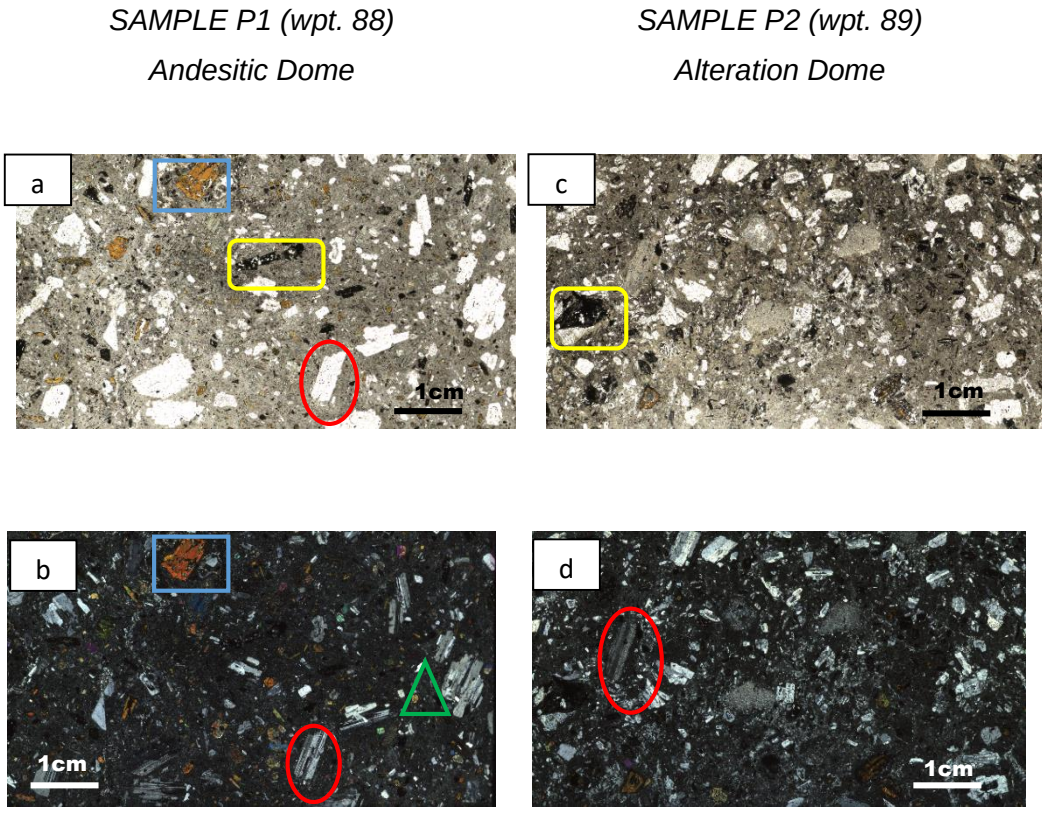

Figure 5.6_ a) Thin section of Alt P1 on parallel Nichols. The blue rectangle is a pyroxene (augite), the yellow one is an oxide mineral. Finally the red ellipse is a plagioclase; b) Thin section of Alt P1 under crossed nichols. The blue rectangle is a pyroxene (augite), the green triangle is an amphibole. Finally, the red ellipse is a plagioclase; c) Thin section of Alt P2 under parallel nichols. The yellow rectangle is an oxide mineral; d) Thin section of Alt P2 under crossed nichols. The red ellipse shows a plagioclase crystal.

The samples examined have a porphyric, hypocrystalline texture and the phenocrysts are mainly plagioclase. Phenocrysts of mafic minerals (clinopyroxene and amphibole) are also common, although less common than plagioclase. The phenocrysts of green hornblende are frequently replaced by brown hornblende or opaque minerals (Barzoi at al. 2010). In the groundmass, the dominant minerals are plagioclase and opaque minerals.

- Plagioclase: in the thin section, plagioclase shows the characteristic albite polysynthetic twinning. This twinning is the most characteristic identifying feature of plagioclase, and makes its identification easy when present. Although some cross-hatched twinning occurs, it is always very simple with only one or two cross twins per grain.
- Augite: this mineral is the second most abundant type of phenocryst in andesites. Normally, the augite can be variably coloured, depending on the amount of iron or titanium. In sample P1, it is predominantly brown and shows a moderate pleochroism.
- Amphibole: the size of the amphibole crystals is about four times smaller than that of the plagioclase phenocrysts, but still distinguishable from that of the groundmass crystals. The cleavages that form 120° angles can be seen very well. The XRPD analysis identified the amphibole as ferro-actinolite.
- Oxide minerals: These minerals are well visible in both thin sections. They are totally opaque in transmitted light and correspond to hematite and goethite (Figure 5.7 and Figure 5.8).

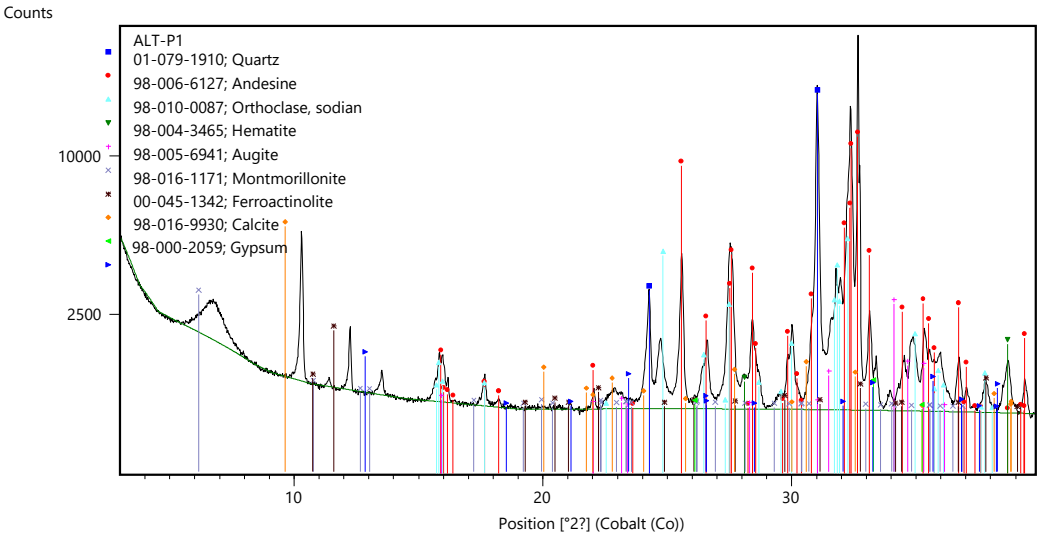

Figure 5.7 _XRPD diffractogram of sample Alt P1

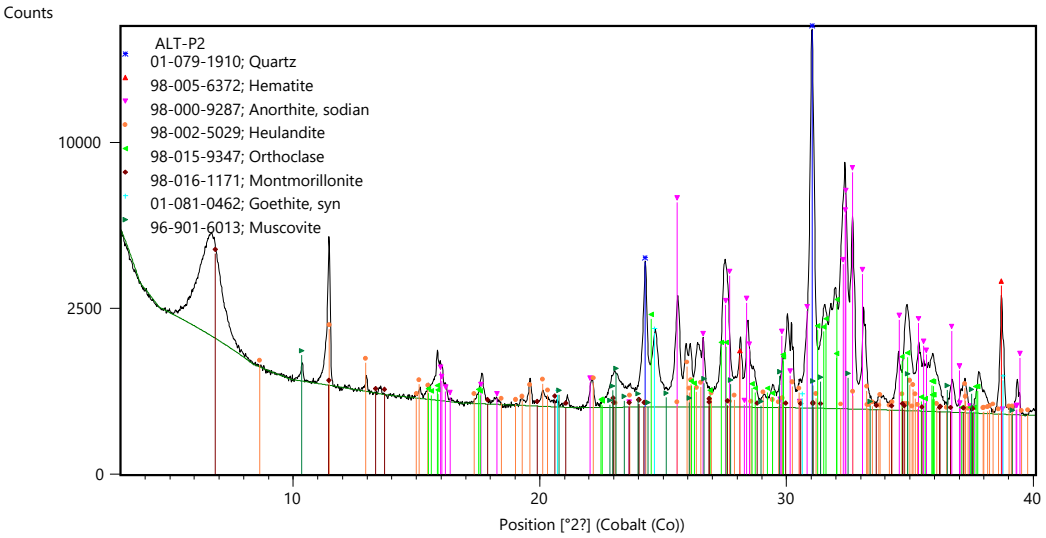

Figure 5.8_ XRPD diffractogram of sample Alt P2.

5.2.3 Pluton Cabeza De Vaca

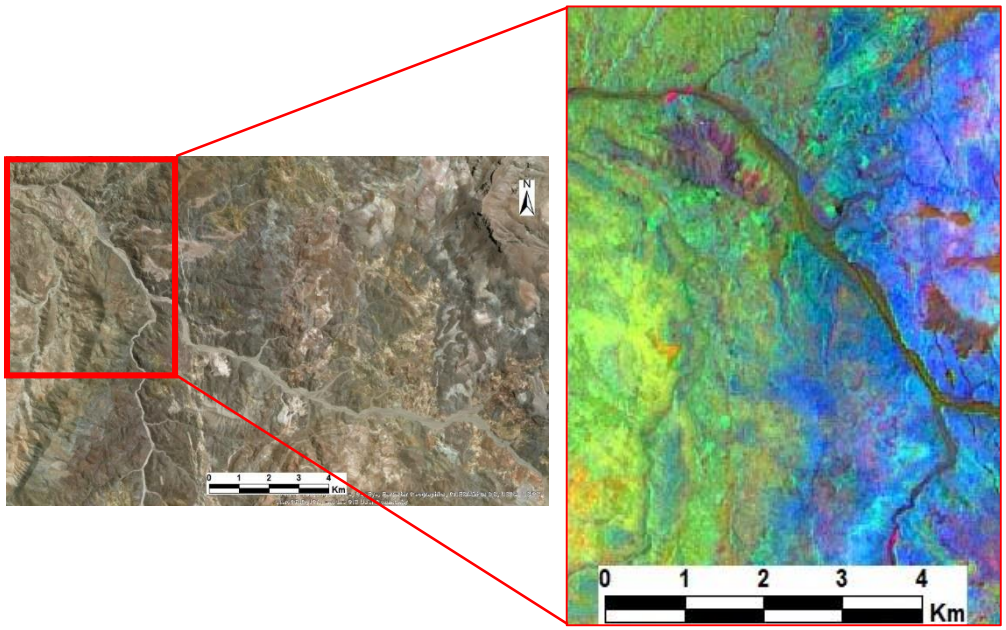

Figure 5.9_a) Basemap of ArcGIS software show the total area on visible wavelength; b)Band ratio image red: 3/1, green: 9/3, blue: (5+9)/8 showing a portion east of the pluton Cabeza de Vaca on contact with Lavas Sierra la Dichosa formation.

An intrusive body of round shape situated in the western area of the map. It is mainly composed of granodiorite and porphyric granite (Figure 5.9). In the granite, the hornblende and biotite crystals can reach a centimetric size in some areas. Monzonite and quartz-monzodiorite may also be part of the intrusion (Kennth 1968). The pluton was dated (Arevalo 1994) to the end of Cretaceous and beginning of Cenozoic. On the ASTER band ratio composition red: 3/1, green: 9/3, blue: (5+9)/8 in Figure 5.10, the pluton has a green colour due to OH absorption of micas with respect to the blue one of the Sierra la Dichosa lavas.

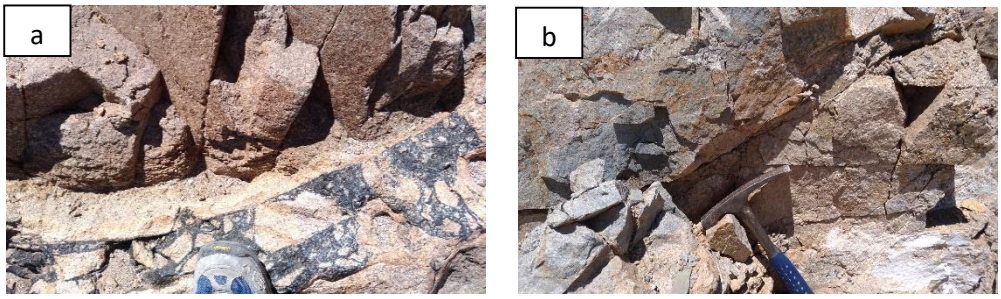

Figure 5.10_ a) Contact between granite and breccia pipe at wpt.95. b) Granodiorite portion of the pluton at the same point.

5.2.4 Estratos De Quebrada El Romero

According to the description of (Kennth, 1968), this formation is divided into three levels. The base is formed by a 900 meter-thick welded tuff of rhyolitic composition. On top are 500 meters of lava flows, whose composition varies from dacitic to andesitic. The series is finally closed by 70 meters of lacustrine limestones, finely laminated sandstones and intercalations of chert. The rocks that are exposed in the map area (Figure 5.11) seem to belong only to the central portion of the section, i.e. the andesitic lava flows.

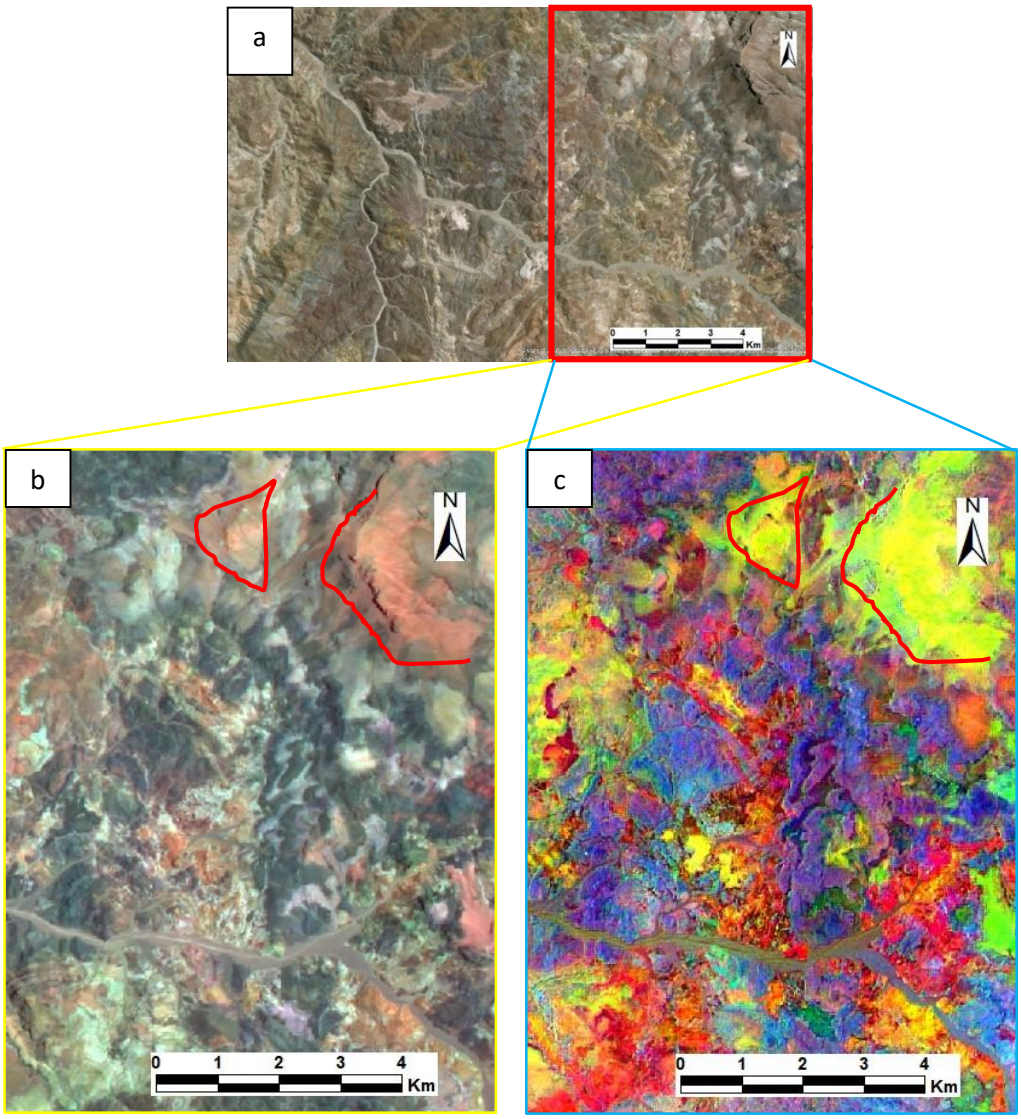

Figure 5.11_a) Basemap of ArcGIS software show the area on visible wavelength; b) ASTER RGB composition 731; c) ASTER RGB band ratio composition red: 3/1, green: 9/3, blue: (5+9)/8.

5.2.5 Ignimbritas De Sierra La Peineta

This is a pyroclastic sequence about 1100 meters thick, in tectonic contact with the formation of the Lavas de Sierra la Dichosa. The basal level of this sequence includes thin layers of tuffs generated by falling material (welded tefra) or by pyroclastic pumice flows. The top of the sequence is made up of massive tuff banks, 20 to 30 meters thick, alternating with trachytic lava flows. The uppermost portion includes dacitic ignimbrites with biotite. We have distinguished this part of the sequence from the lower one because of their spectral difference. Indeed, from Figure 5.11 it is possible to separate the *Top ignimbrite* from the bottom one (considering the red lines). This portion has an orange colour on ASTER composition 731, whereas the bottom one has a dark blue colour. In the same way, from ASTER band ratios (3/1, green: 9/3, blue: (5+9)/8) it is possible to distinguish the top sub-unit with a yellow colour above the red one of the bottom unit.

The origin of the ignimbrite of Sierra La Peineta is still unknown; however, the large amount of ignimbrite and the stratigraphic relations indicate that the deposition occurred before the formation of the El Durazno caldera at the beginning of the Cenozoic (Iriarte, S. 1999).

5.2.6 Caldera El Durazno

This is a circular shape structure that rests above a basement, which includes the formation of the Lavas de Sierra la Dichosa (Figure 5.12) (Díaz-Alvarado, et al. 2016). The El Durazno caldera presents an excellent preservation of the annular and transversal fractures that canalised the effusions of the magmatic material, as well as collapse breccias, intracaldera tuffs, some eruptive ducts, post-collapse lavas, lacustrine deposits and post caldera intrusions. The El Durazno caldera has been dated using K-Ar methods, obtaining values between 56 and 53 Ma (Iriarte 1999).

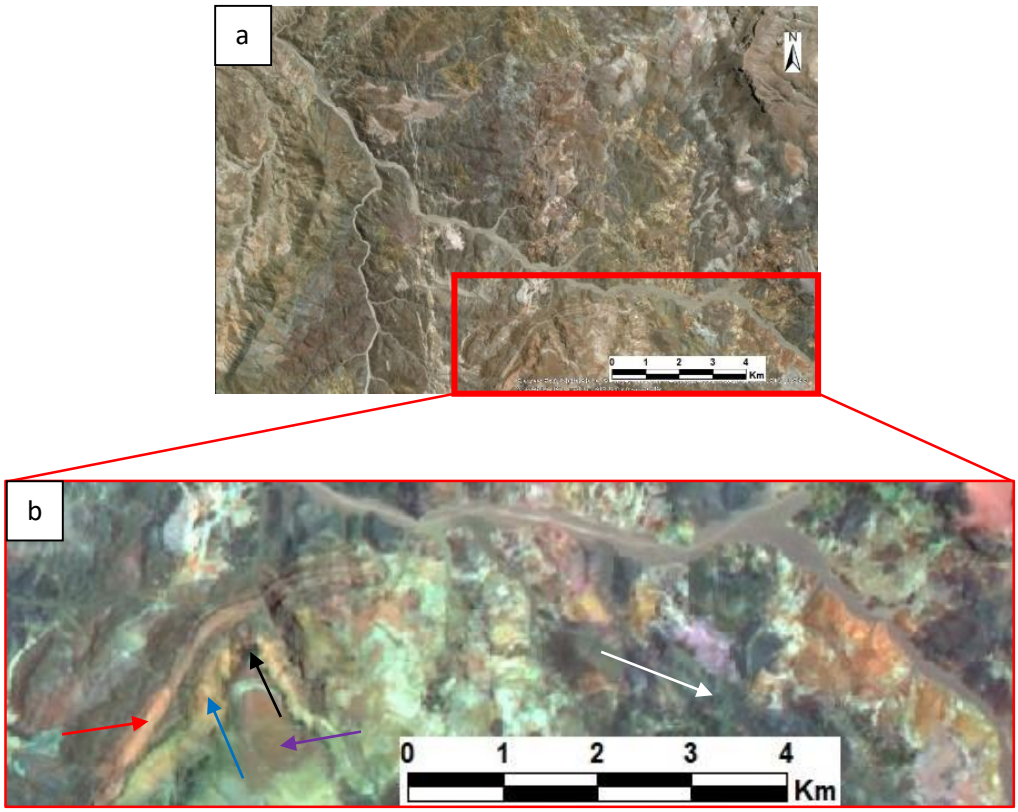

Figure 5.12_a) Basemap of ArcGIS software show the area on visible wavelength; b) ASTER RGB composition 731. Red arrow indicate the edge of caldera, blue arrow the welted ignimbrite, black arrow one

5.2.6.1 Facies of the Caldera edge

These facies are characterized by high dip angles (> 60º) towards the caldera interior. They are mainly composed by lensed deposits with blocks up to several meters in diameter of andesitic composition in a cineritic matrix. Mylonites developed at the base of the caldera, present a strong stretch and reduction of the grain size observed in the phenocrysts of plagioclase, and fault rocks and highly altered materials that compose the matrix of the large rounded blocks of mylonites and breccias (Díaz-Alvarado 2016). In Figure 5.12, on ASTER 731 this unit shows a well-developed stratification of pink colour.

5.2.6.2 Ignimbrite and obsidian lava flows

The composition of the pyroclastic units in the collapse phase of the caldera ranges from dacitic to rhyolitic. To the bottom, they are welded ignimbrites of pink colour (blue arrow on Figure 5.12) with grains always smaller than 1 cm in

diameter. At the top of these ignimbrites, 5 to 15 meters of obsidian lava flows are visible on Figure 5.12 (black arrow).

5.2.6.3 Post collapse lacustrine deposits with lava flows intercalation

At the top of the ignimbrite unit, erosive surfaces and fine-grained sediments and parallel lamination are developed, with some matrix-supported mass flow deposit (green arrow on Figure 5.12). Above this sedimentary unit, principally andesitic lavas are deposited (white arrow on Figure 5.12). The intracaldera units are cut by faults with orientation NE-SW, with normal dextral kinematics, which are the structures along which rhyolitic dykes rose up during post-caldera activity

5.2.6.4 Rhyolitic domes and dykes

During the terminal phase of the El Durazno caldera, the study area was subjected to magmatic flows of acidic composition. The geological forms that highlight this activity are a series of magmatic domes and dykes of rhyolitic composition with high silica contents (66-79%) (Arevalo 1994) The rising magmas exploited the fractures created during the caldera activity (Figure 5.13-a and b). From the satellite view it is possible to see white dikes filling well defined fractures with N-S orientation (Figure 5.14-b).

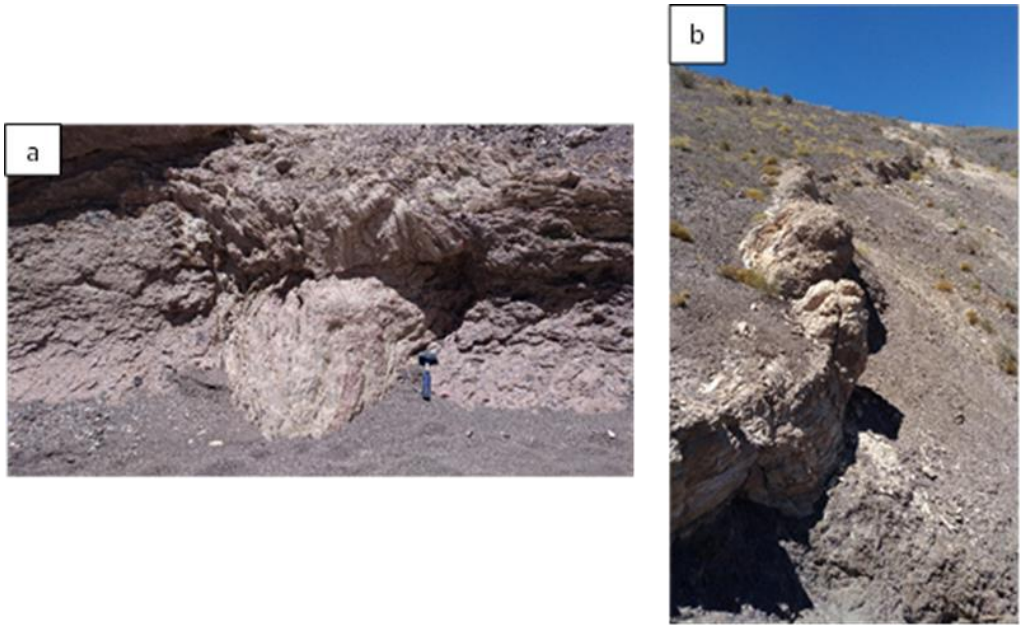

Figure 5.13 In both images, a (wpt.10) and b (wpt.28), it is possible to see the fractures along which acidic magmas were intruded to form dikes and domes

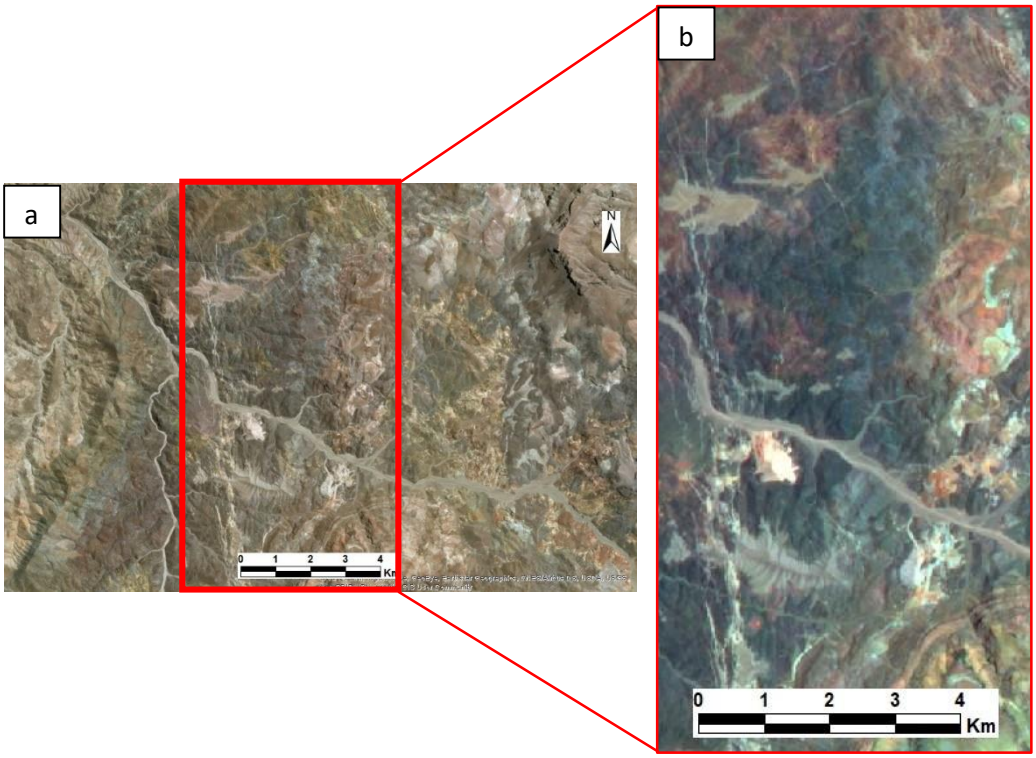

Figure 5.14_ a) Basemap of ArcGIS software show the area on visible wavelength; b) ASTER RGB composition 731. Where the white line with orientation N-S are ryolithic dykes.

5.2.7 Grava De Atacama

This unit consists of unconsolidated, polygenic gravels, with well layered sand and silt lenses and local intercalations of weakly welded tuff. The material constitutes the deposit of an ancient hydrographic network that partly coincides with the current one. Dating using the K-Ar method on tuff samples indicated an age between 12 and 15 Ma (Middle Miocene) (Iriarte 1999).

This unit is easy to visualize using satellite images also in a visible wavelength spectral range. The unit is identified with yellow ellipses in Figure 5.15.

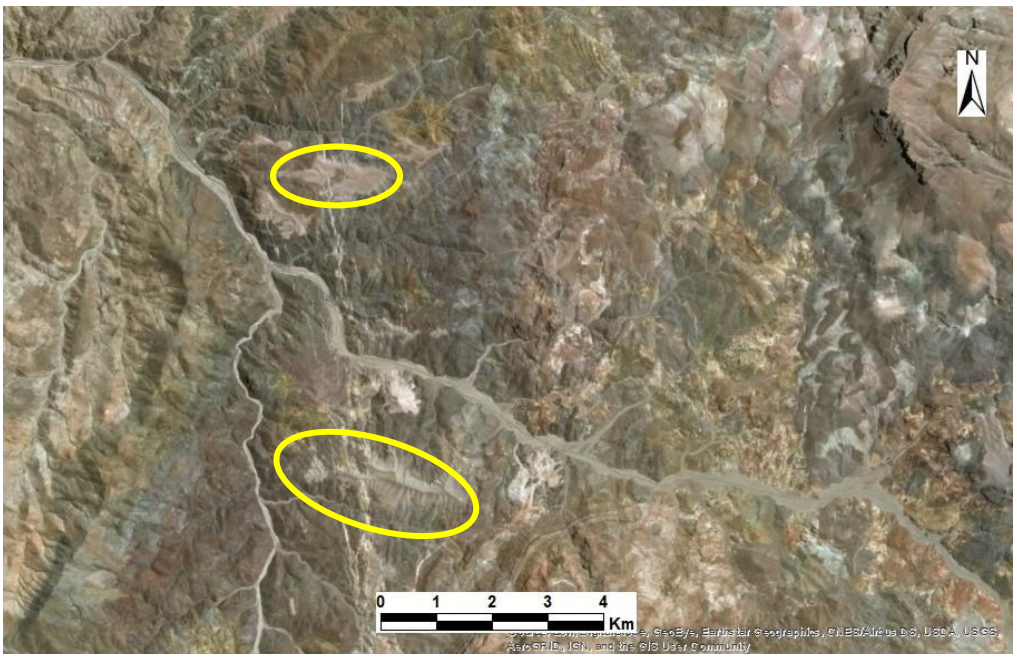

Figure 5.15_ Basemap of ArcGIS software on visible wavelength. Yellow ellipses indicate the Grava de Atacama unit.

5.2.8 Alluvial sediments

These sediments are gravels and sandy gravels associated with drainage systems with intermittent activity. The deposit consists of sub-angular clasts with silt-sandy matrix that were transported from the various secondary valleys. This unit is well detected on Figure 5.15, it has a grey colour and it is localized on the bottom of the valleys.

5.3 HYDROTHERMAL ALTERATION ZONES

In the north-eastern portion of the El Durazno caldera, various areas affected by hydrothermal alteration have been identified by remote sensing. These zones were distinguished from other two (breccia pipe zone and vein-rich alteration zone) situated on the west side because of their different alteration style.

During the fieldwork, a chip sampling was performed to identify and classify the different alterations. Samples were analysed mainly by XRPD because of their high degrees of alteration and poor cohesiveness. However, some samples were also analysed under the microscope to recognise their microstructures.

In general, the type of alteration may vary as a consequence of changes in the compositions and temperatures of fluids circulating through the rock. In the present work, different areas have been classified according to the dominant type of alteration observed in the rocks. In this way, three main zones have been identified.

- Clay-rich alteration zone: in this zone, the alteration is marked mainly by clay minerals. The most characteristic alterations are phyllic and argillic (intermediate and advanced).
- Silicification zone: principally silicified rocks characterise this zone, but in some sites as in waypoint 72 (Figure 5.1) a clay-rich alteration occurs.
- Carizallillo alteration zone: this zone is located next to the mountain Carizalillo, which is formed by the ignimbrite of Sierra la Peineta formation. It was not possible to visit extensively this zone, therefore further remote sensing work was carried out using the Hyperion sensor (see chapter 6).

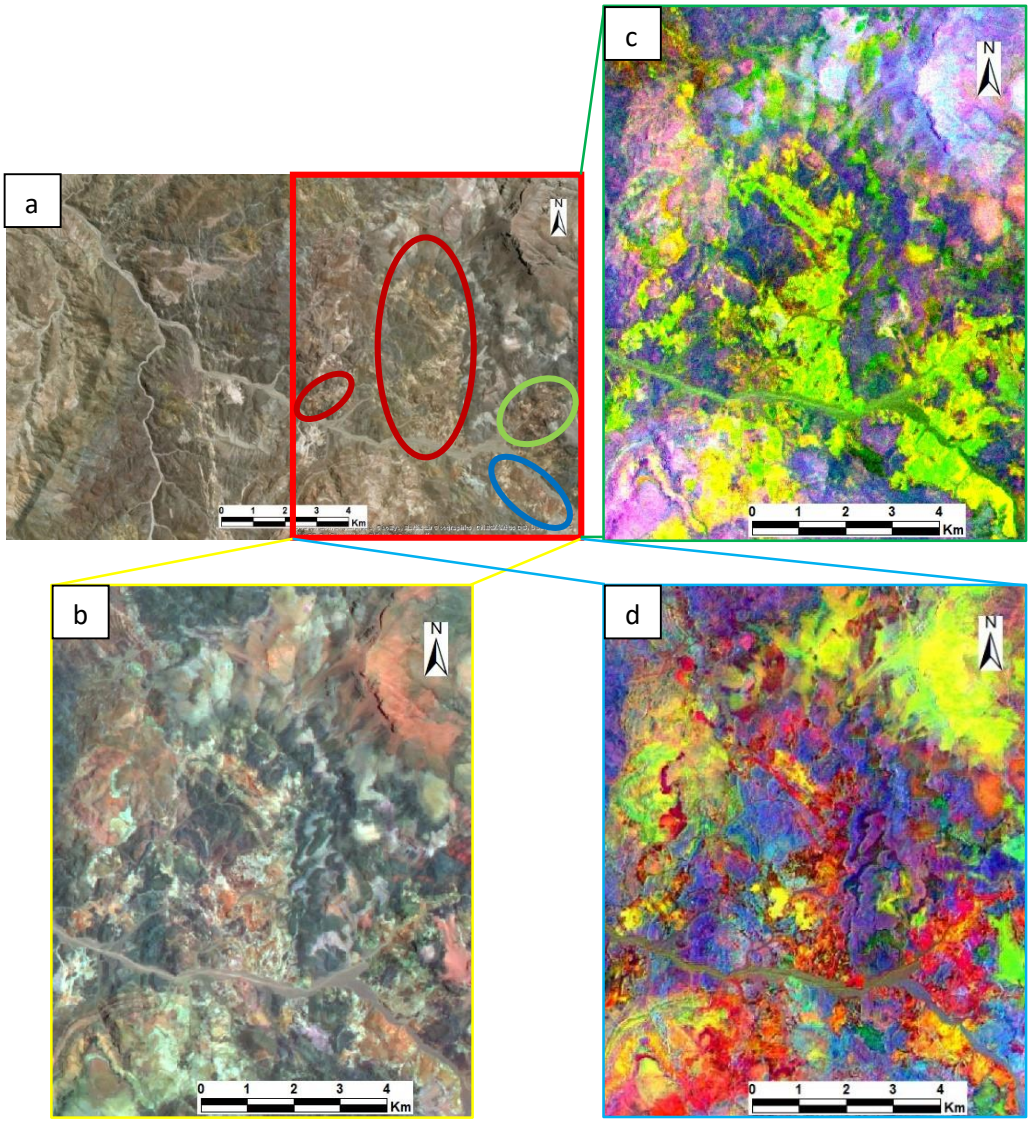

Figure 5.16_ a) Basemap of ArcGIS software show the area on visible wavelength, showing Cla-rich zone with blue ellipse, silicified rocks zone with a green ellipse and Carizallillo alteration with red ones; b) ASTER RGB composition 731; c) Principal Component Analysis (PCA) set on PC9 (red), PC7 (green) and PC5 (blue); d) ASTER RGB band ratios composition focusing to 3/1, green: 9/3, blue: (5+9)/8.

On ASTER 731 composition image (Figure 5.16-b) it is possible to distinguish two principal colours in the alteration zones, red and white. Red colour detects areas where phyllosilicates are present because of the Al-OH and Mg-OH absorption bands. White areas are indicative of high albedo so they do not give specific information; however, considering the RGB band ratios (3/1, green: 9/3,

blue: (5+9)/8). (Figure 5.16-d), the same zones have a red colour. This colour represents the charge transfer on Fe oxides or sulphate minerals. This distinction is also apparent from the Principal Component Analysis (Figure 5.16-c), but with yellow and green colours.

5.3.1 Clay-rich alteration zone

A series of samples were collected along the valley that delimits the alteration zone, on the east side (Figure 5.17-a). This area is dominated by argillic alterations.

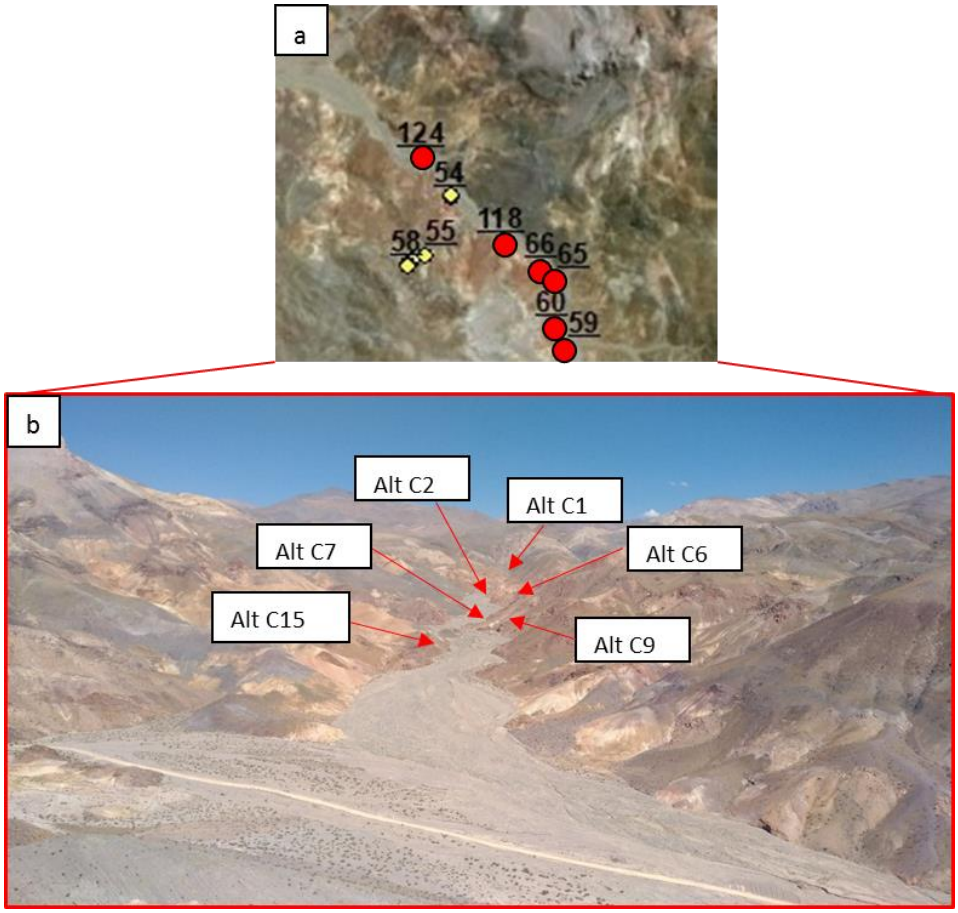

Figure 5.17 _ a) Image shows the waypoints taken in the clay-rich alteration zone (yellow spots) and the sampling sites (red spots); b)View of the valley with the positions where samples were taken.

The sample **Alt C1** has a porphyric hypocrystalline texture, in which the phenocrysts are mainly plagioclase (Figure 5.18). Some mafic crystals are visible

but altered in sericite and oxides. The rock has been classified as a porphyric andesite. It has undergone a low degree of alteration and it has preserved the initial structure. XRPD analysis (Figure 5.19) shows the presence of jarosite and sericite as alteration minerals.

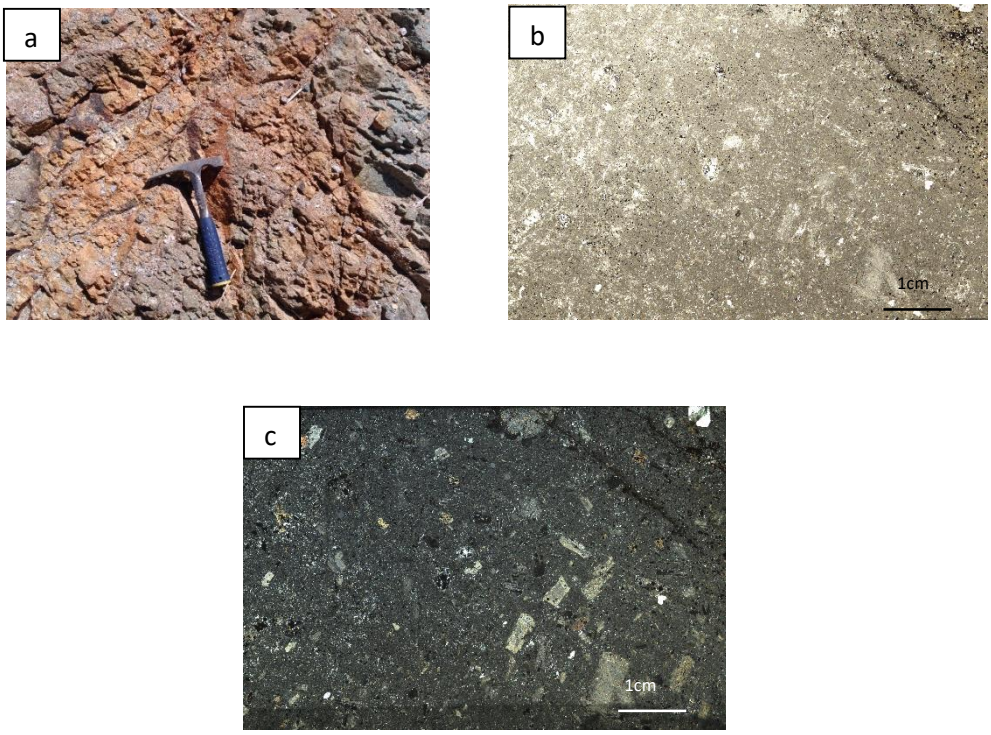

Figure 5.18_a) Outcrop of porphyric andesite with minimum degree of alteration; b) Thin section of sample Alt C1 under parallel nichols, wpt. 59; c) Thin section of sample Alt C1 under crossed nichols, wpt 59.

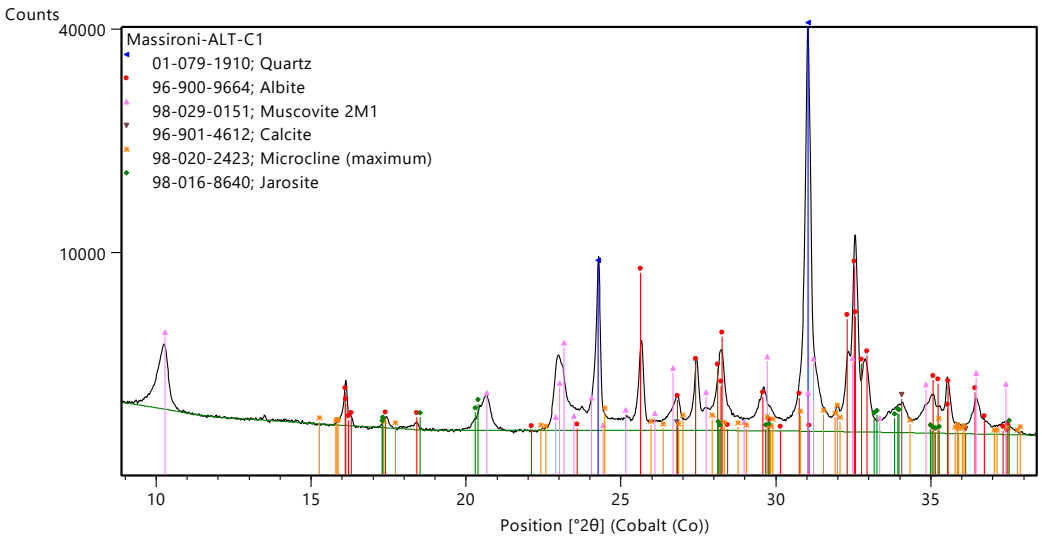

Figure 5.19_ XRPD diffractogram of sample Alt C1

The outcrop from which sample **Alt C2** was taken shows a rock that was completely altered by argillic alteration (Figure 5.20), so it was impossible to determine the nature of the protolith. XRPD analysis indicates the presence of dominant alunite and montomorillonite, with less abundant gypsum, quartz, sericite, microcline and phologopite (probably confused with another phyllosilicate. (Figure 5.21).

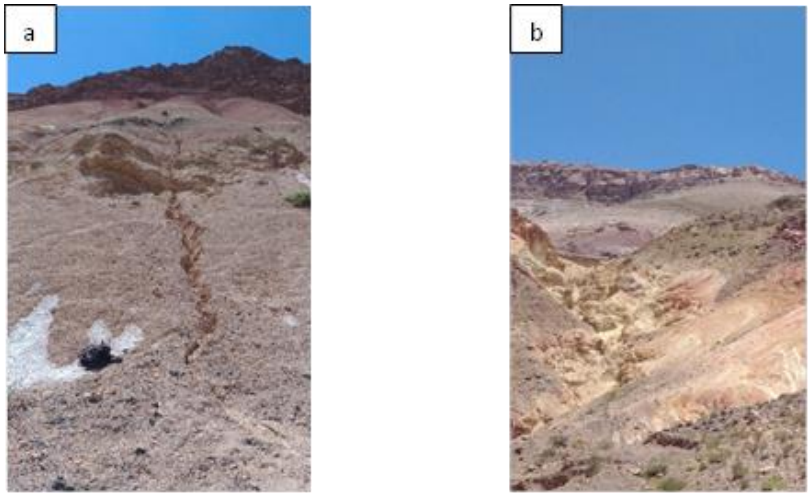

Figure 5.20_ a) and b) are photos of the same outcrops affected by argillic alteration, wpt.60

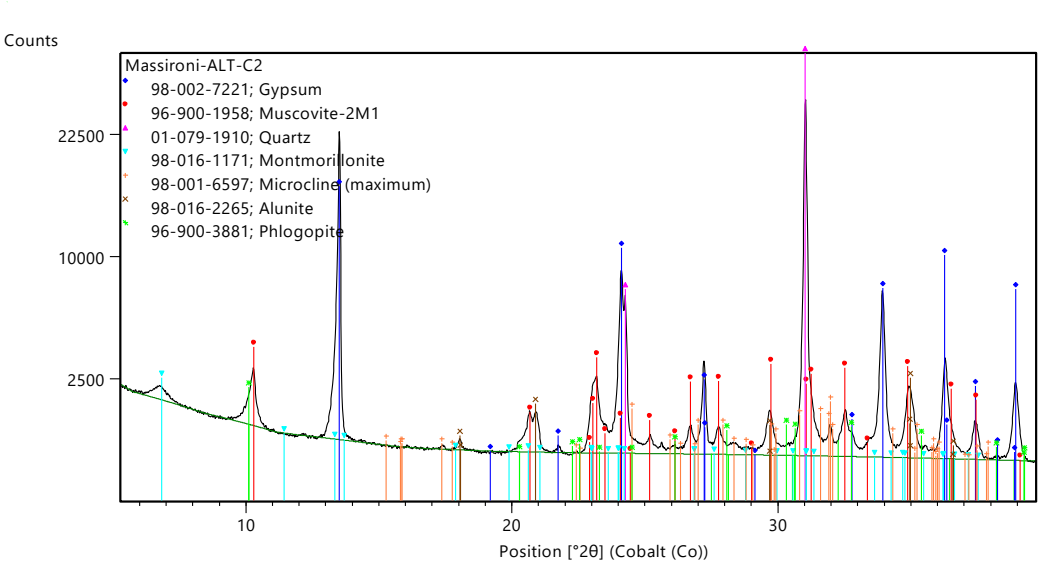

Figure 5.21_ XRPD diffractogram of sample Alt C2

The rock **Alt C6** is completely altered into sericite and pyrophyllite (Figure 5.23). In addition the rock mass is cut by epidote veins (Figure 5.22-c). This mineral has not been detected by XRPD analysis, because it is mostly present within the veins. Other detected minerals are quartz, jarosite, microcline and Ca-rich plagioclase.

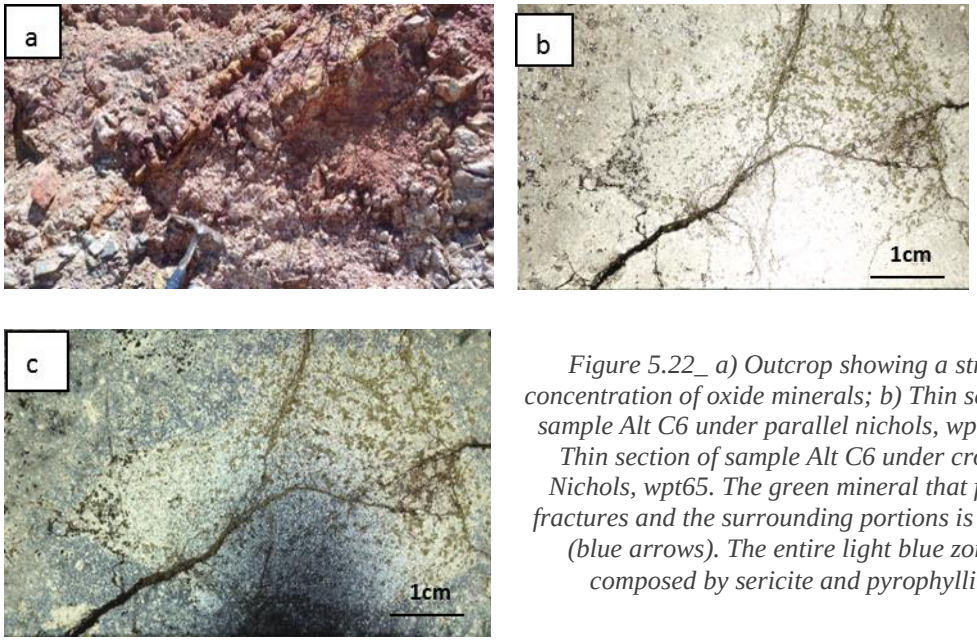

Figure 5.22_ a) Outcrop showing a strong concentration of oxide minerals; b) Thin section of sample Alt C6 under parallel nichols, wpt.65; c) Thin section of sample Alt C6 under crossed Nichols, wpt65. The green mineral that fill the fractures and the surrounding portions is epidote (blue arrows). The entire light blue zone is composed by sericite and pyrophyllite.

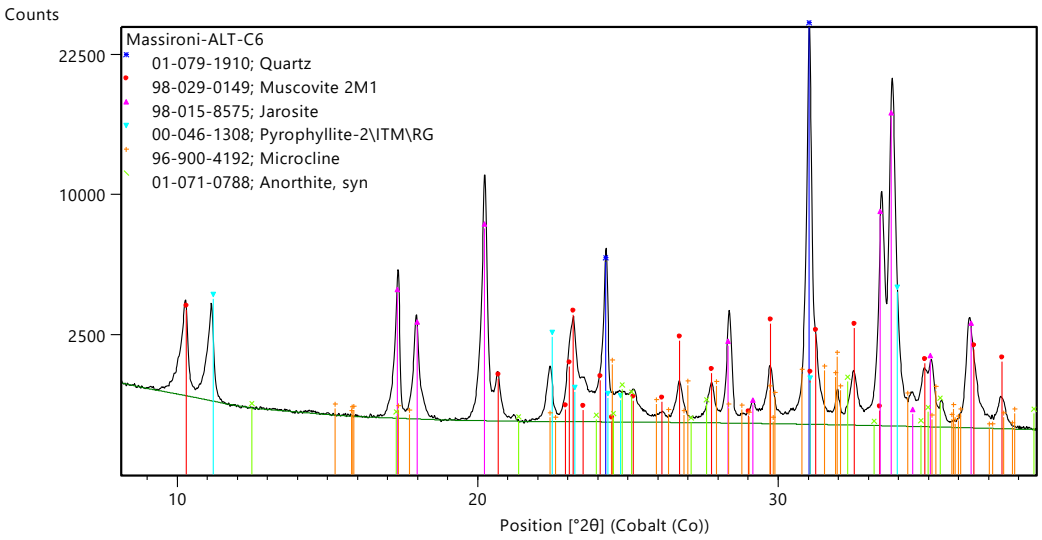

Figure 5.23_ XRPD diffractogram of sample ALT C6

The rock **Alt C7** is completely altered into sericite and clay minerals (montmorillonite) (Figure 5.24). Epidote veins are also occur, similar to sample Alt C6. Phenocrysts of mafic minerals (altered into clay minerals and oxides) or plagioclase (altered into sericite) are also present. Other minerals in this sample are rutile, replacing mafic minerals and hydroniumjarosite (

The outcrop of sample **Alt C9** shows a rock completely transformed by phyllic alteration (Figure 5.26). XRPD analysis shows the presence of illite (Figure 5.27). Other minerals are quartz, rutile, jarosite and muscovite (Figure 5.25).

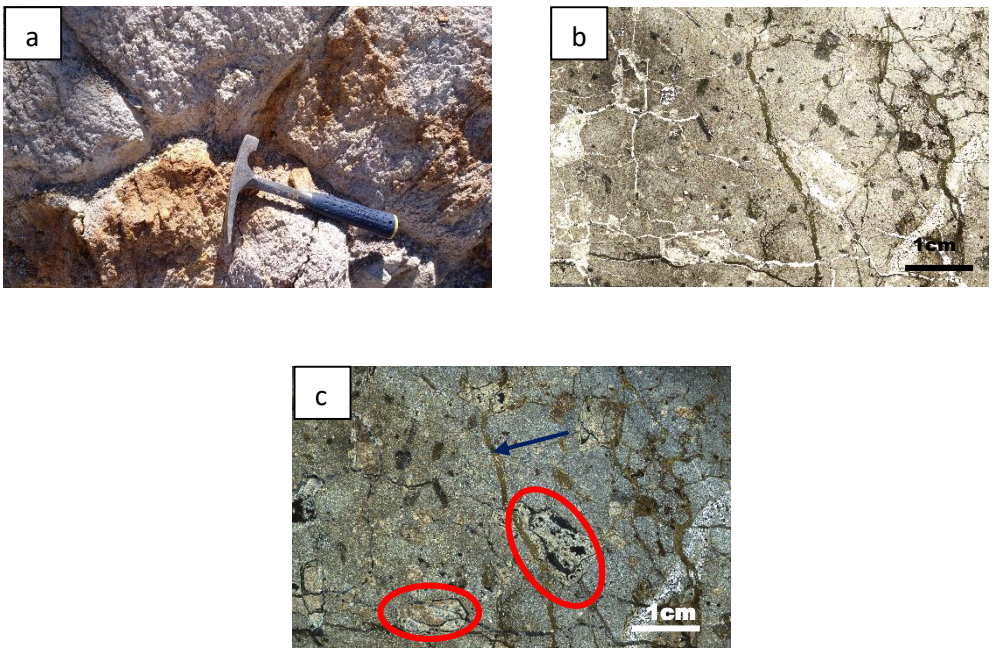

Figure 5.24_a) Outcrop showing argillic alteration, wpt.66; b) Thin section of sample Alt C7 under parallel nichols, wpt.66; c) Thin section of sample Alt C7 under crossed nichols, wpt.66. The green mineral that fill the fractures is epidote (blue arrow). Phenocrysts (red ellipses) are replaced by oxides or clay minerals. All the light blue zone is composed by clays minerals.

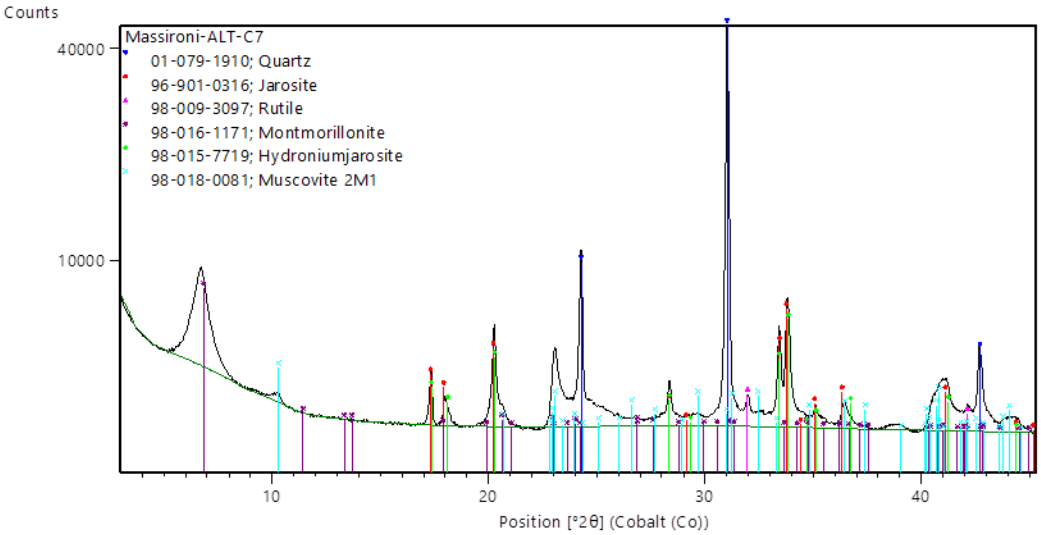

Figure 5.25_ XRPD diffractogram of sample Alt C7

Figure 5.26_ Outcrop with argillic alteration from which sample Alt C9 was collected. Wpt.118

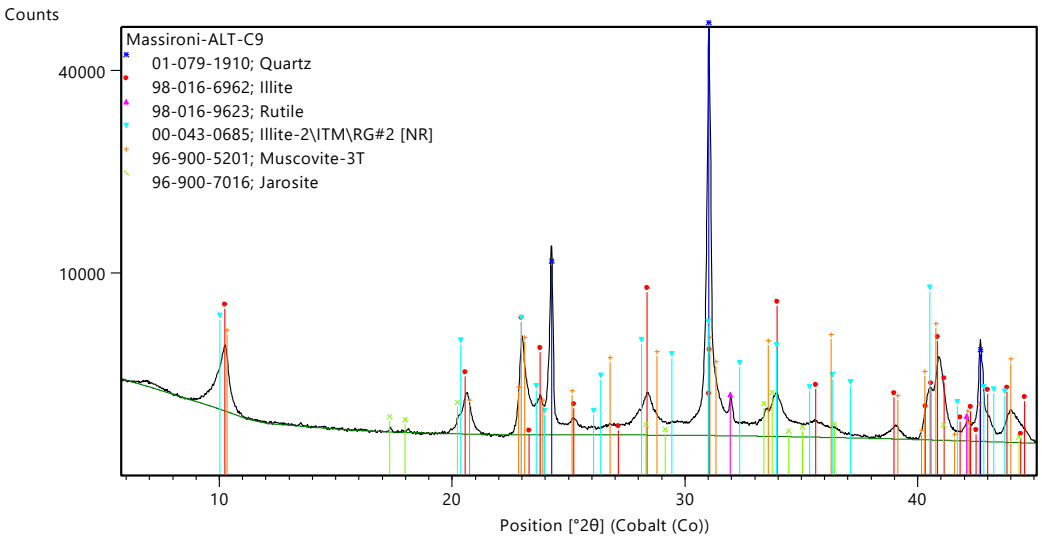

Figure 5.27_ XRPD diffractogram of sample Alt C9.

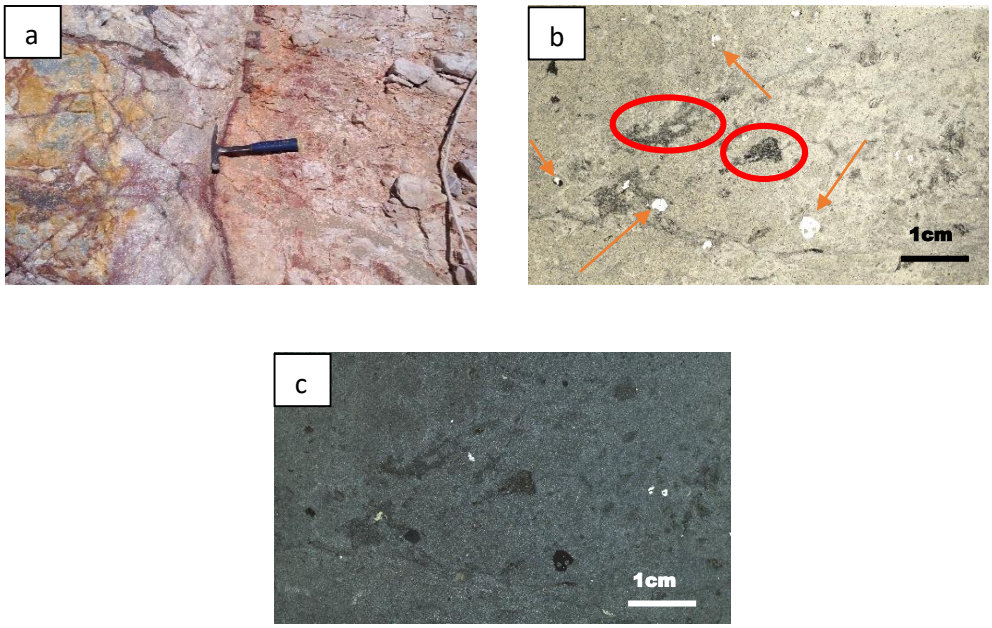

Figure 5.28_ a) Outcrop showing a boundary between relatively fresh andesite and strongly altered rock, wpt.124; b) Thin section of sample Alt C15 under parallel nichols showing a vuggy quartz alteration (red arrows) and oxide minerals (red ellipse); c) Thin section of sample Alt C15 under crossed nichols.

At waypoint 124, a limit between a porphyric andesite, affected by a low grade of alteration, and a strongly altered silicified rock is exposed. In the thin section of samples **Alt C15**, taken from the strongly altered rock, millimetric holes are visible (Figure 5.28-c). This particular texture can be described as a vuggy silica alteration.

5.3.2 Silicified rocks zone

In the east side of the area (Figure 5.16), a zone affected by a strong silica alteration has been found. This area differs from the clay-rich alteration zone because of the significantly lower amount of clay minerals.

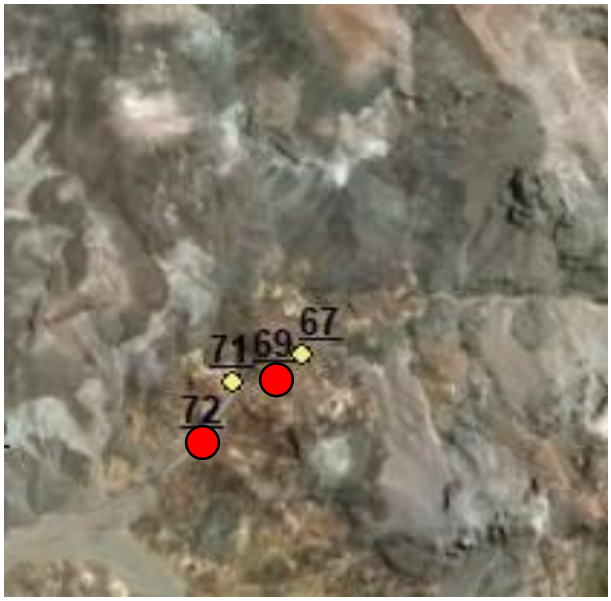

Figure 5.29_Waypoints taken in the field (yellow spots) and sampling sites (red spot)

Sample **Alt M1** collected at waypoint 69 (Figure 5.29) is principally composed by small quartz crystal (Figure 5.30-b). This sample is very similar to sample Alt C15 from the clay-rich alteration zone. Indeed, the two rocks could be derived from the same protolith and were affected to similar extent by the same type of alteration. In Figure 5.30-a, the porphyric texture of an andesite is still recognisable, but analysing the sample Alt M1 the amount of quartz is more than 80% of the rock (Figure 5.30- b). Circular features in Figure….. can be interpreted as pre-alteration features (probably onion-like exfoliations). The percolation of fluids has created several concentric silicified bodies which, with the subsequent erosion, have come off leaving out spherical holes (Figure 5.30-b). This morphology is so particular that could be useful to find silicified outcrops. In the thin section, holes with millimetric diameter are visible (indicated by arrows in Figure 5.30-c). This particular texture can be described as a vuggy silica alteration.

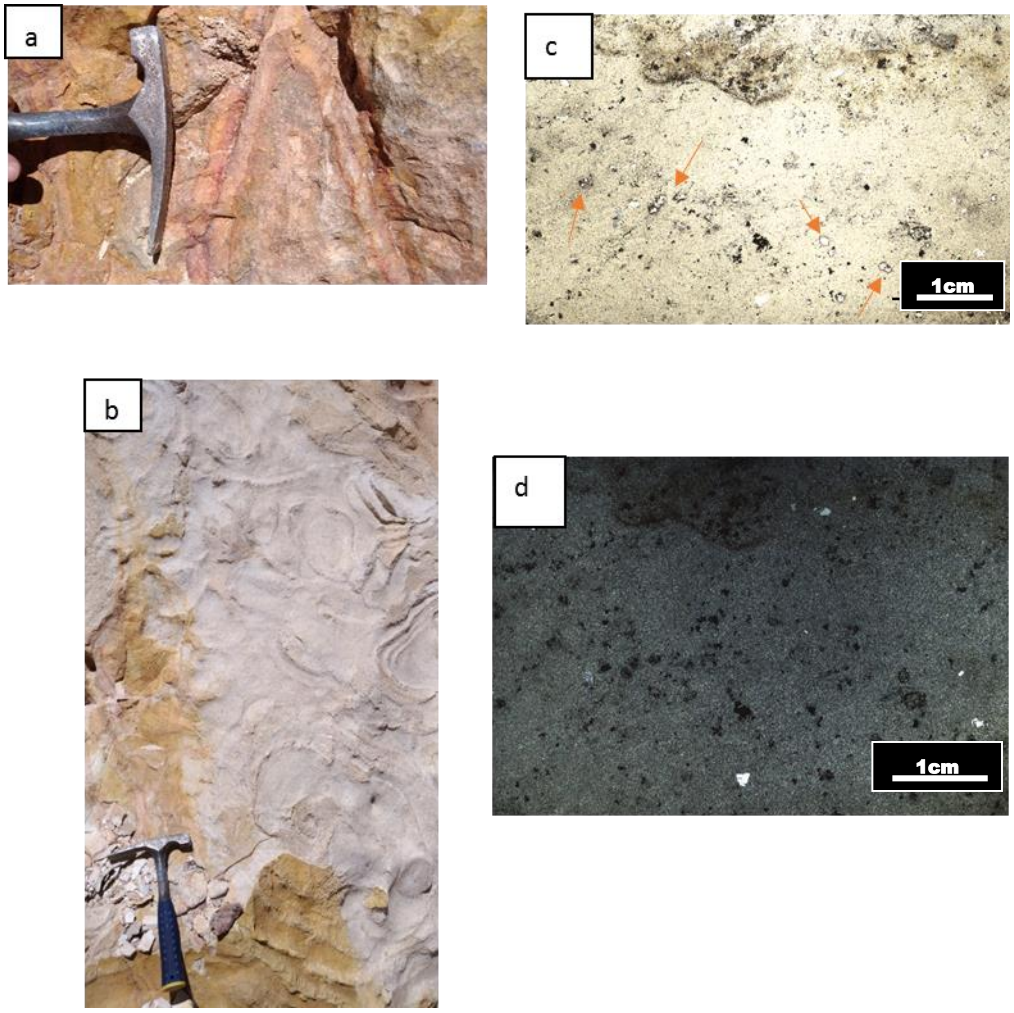

Figure 5.30_a) Andesite affected by weak alteration, wpt.69; b) Outcrop of sample Alt M1 composed by secondary quartz with spherical holes, wpt.69; c) Thin section of sample Alt M1 under parallel nichols; the arrows indicate the vuggs, d) Thin section of sample Alt M1 under crossed nichols.

The waypoint 72 (Figure 5.29) shows where the sample **Alt M2** was collected. This rock is extensively altered by intermediate argillic alteration (Figure 5.31), and is dominated by interstratified illite–smectite and quartz. In addition there are also the oligoclase (Figure 5.32).

Figure 5.31_Outcrop showing argillic alteration, wpt.72.

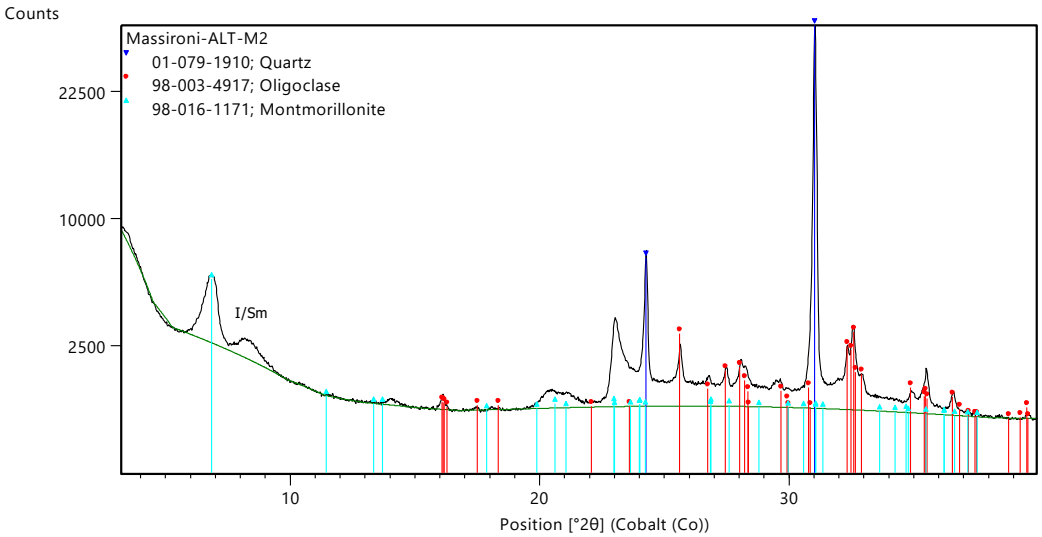

Figure 5.32_ XRPD Difractogram of sample Alt. M2.

5.3.3 Carizallillo alteration zone

The position of this alteration zone is shown in Figure 5.16. Unfortunately, this area has not been fully studied during the fieldwork but a report by Aragonita

Asesorias ltda mining company on this area was found and studied. During this time three high-sulfidation epithermal bodies were discovered.

The only portion visited during the fieldwork was in the Lavas Sierra la Dichosa at the waypiont 18. In this site, the hill cap is composed by a limonitic gossan with supergenic mineralisation, made of iron oxides and sulphates such as hematite, goethite and jarosite (Figure 5.34-b).

Figure 5.33_ Waypoints taken in the field in the Carizallillo alteration zone

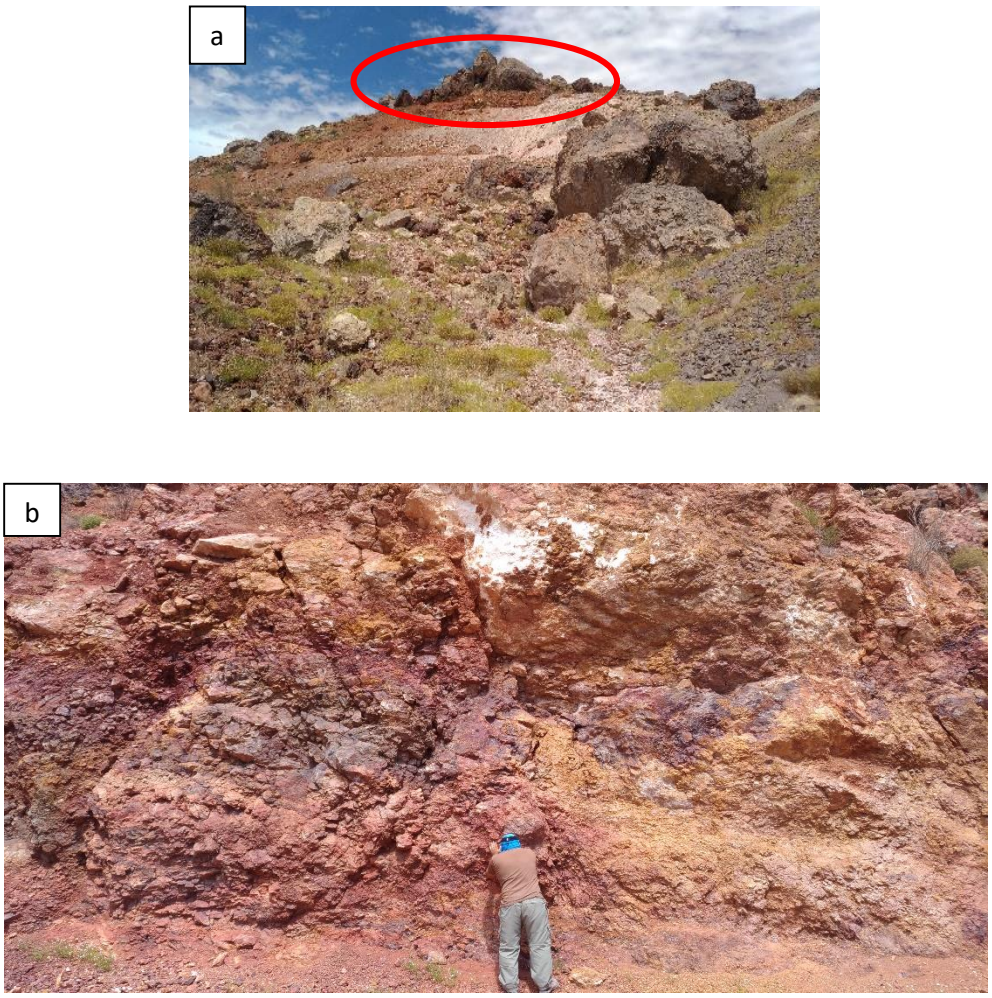

Figure 5.34_a) View of the limonitic gossan (red ellipse) from wpt.15. b) Limonitic gossan, formed by a solid gel of hematite, goethite and jarosite wtp.18.

5.3.4 Vein-rich alteration zone

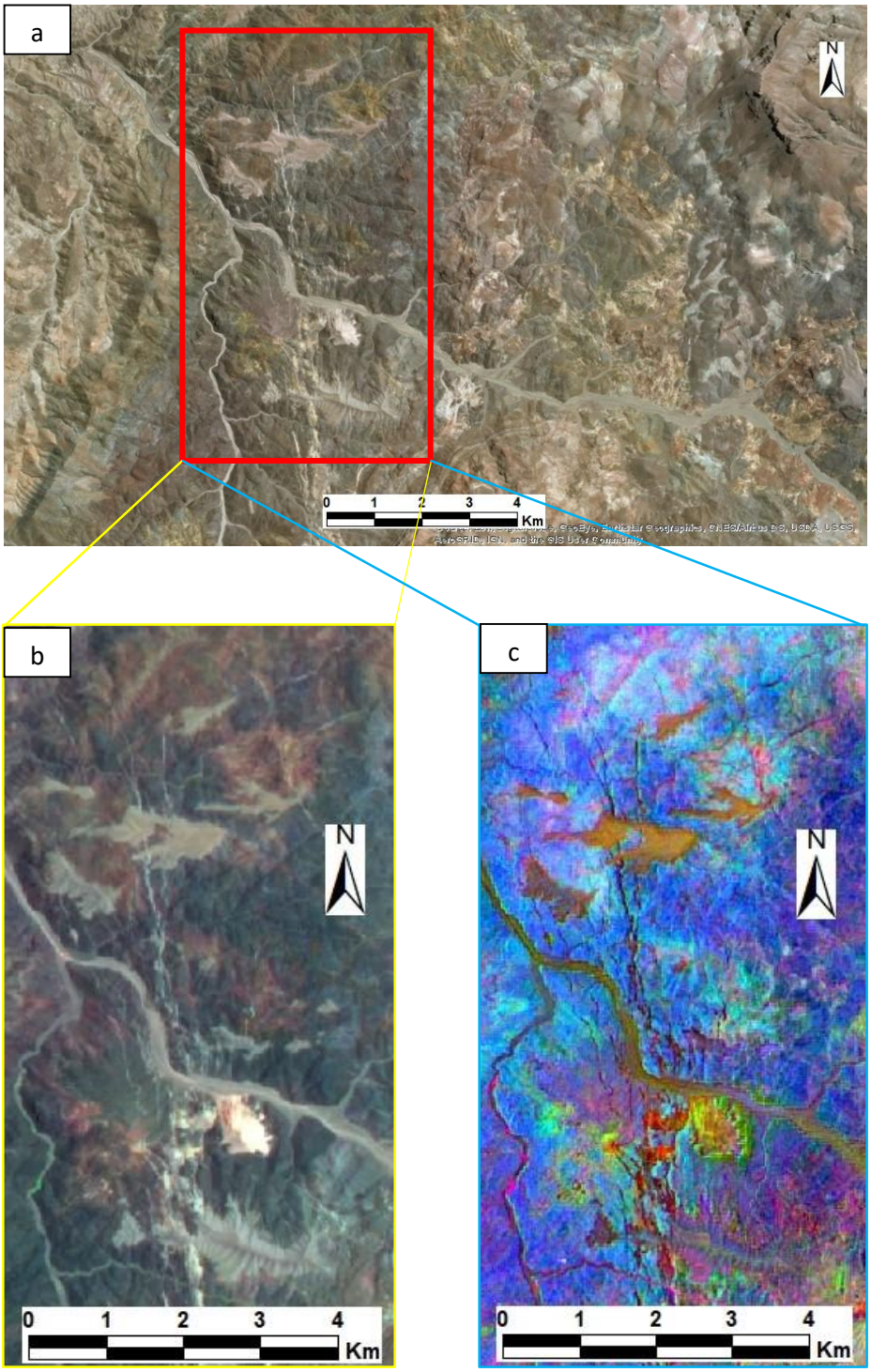

Figure 5.35_ a) Basemap of ArcGIS software showing the study area (red rectangle) on visible wavelength; b) ASTER RGB composition 731; b) ASTER RGB band ratio composition red: 3/1, green: 9/3, blue: (5+9)/8.

By interpreting the ASTER images in false colours, it was noted that within the formation of Lavas Sierra la Dichosa there are areas with different tones of colours. For example, in RGB band ratios (red: 3/1, green: 9/3, blue: (5+9)/8), zones with a lighter tonality of blue (cyan blue) can be seen. In the same way, analysing the ASTER image colours composition 731, it is possible to see a change from dark blue to red in exactly the same area (Figure 5.35). After the field checks, it was seen that these areas were affected by hydrothermal alteration.

A large presence of mineralised veins was noted during the fieldwork in the study area (Figure 5.36). The economic mineralisation within the veins is made by oxidised copper minerals (crysocolla, Figure 5.36-d) or sulphides (chalcopyrite, bornite), depending on the depth.

In some cases, it is possible to find galena and sphalerite. Small and medium local companies are currently exploiting these resources.

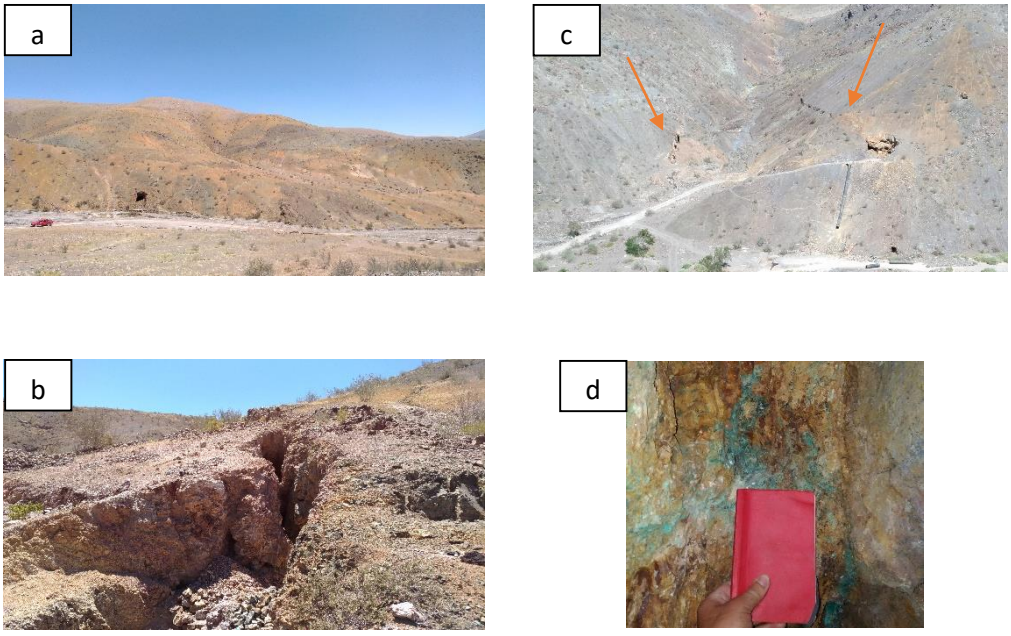

Figure 5.36_ a) View of alteration and mine workings from wpt 115; b) Extraction of copper-iron vein minerals in wpt 115; c) View of two fractures with copper mineralization from wpt 36, the veins are indicated with the red arrows. d) A big scale image of fracture in wpt 36.

In other cases, such as in sample Alt BP13, the alteration is dominated by epidote and chlorite. The XRPD analysis of the powder detected the following mineralogical association: quartz, epidote, albite, muscovite (sericite), titanite and clinochlore (Figure 5.38).

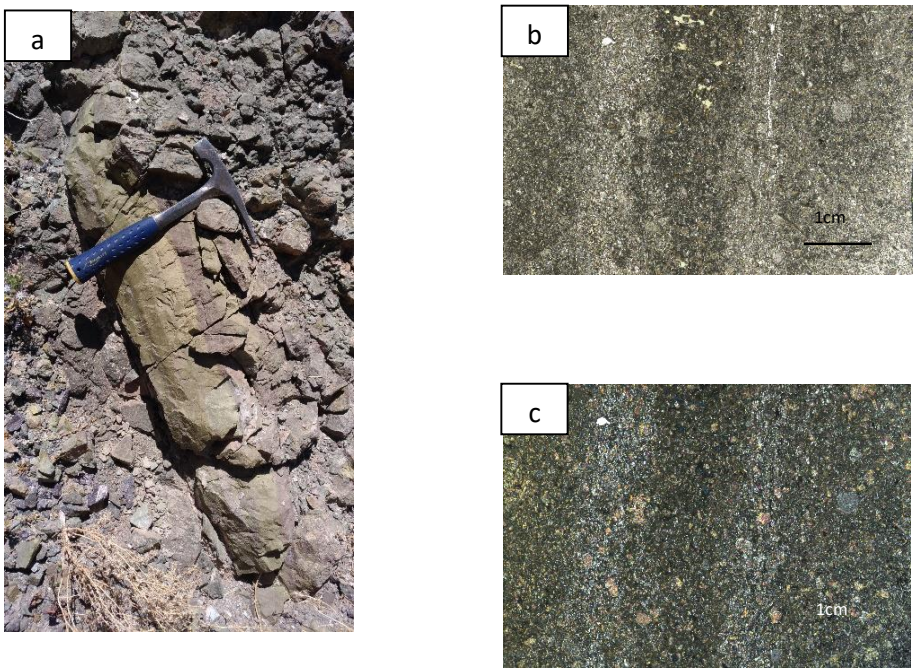

Figure 5.37_a) Outcrop from which sample Alt BP13 was taken; b) Thin section of Alt BP13 under parallel nichols; c) Thin section of Alt BP13 under crossed nichols. Here, chlorite (bluish) and epidote (high interference colours) are visible.

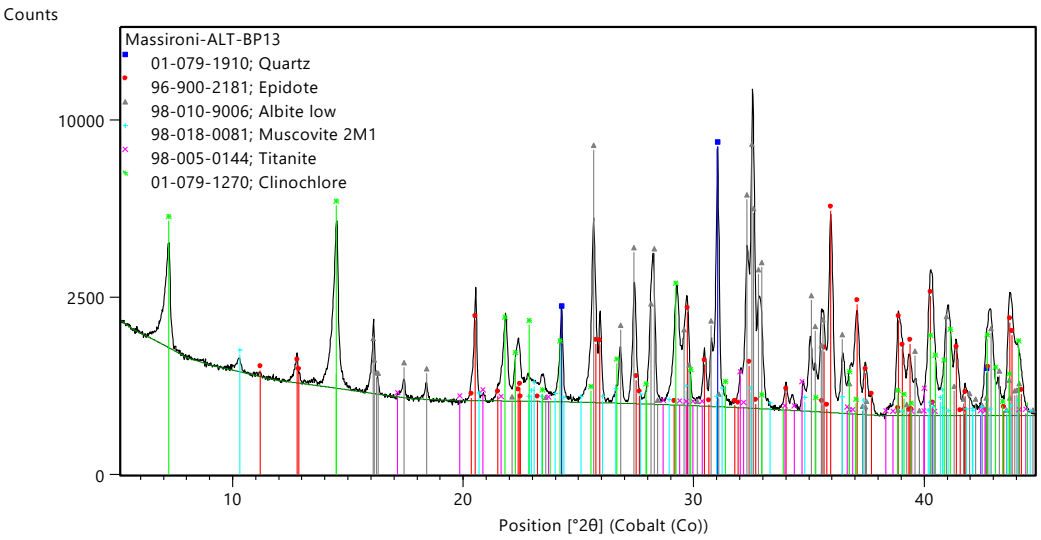

Figure 5.38_ XRPD Difractogram of sample Alt BP13

5.3.5 Breccia pipe zone

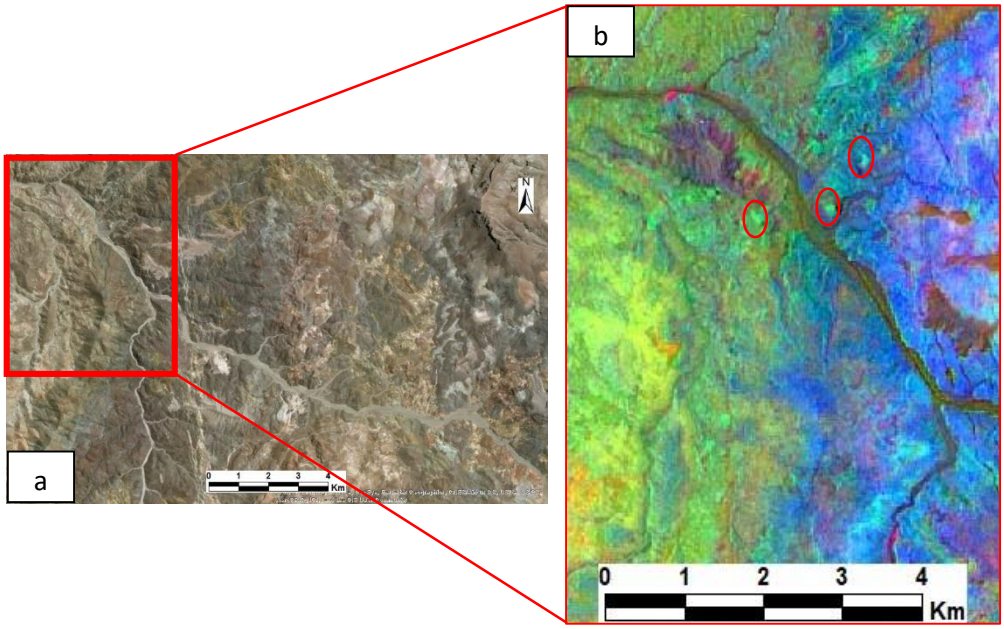

Figure 5.39_a) Basemap of ArcGIS software showing the study area on visible wavelength; b) Band ratio image showing a portion east of the pluton Cabeza de Vaca in contact with Lavas Sierra la Dichosa formation. The greener spots, marked by red circles, are the alteration halos of the breccia pipes.

On the east side of the pluton Cabeza de Vaca (west side in Figure 5.2) close to the contact with Lavas Sierra la Dichosa formation there are breccia pipes with a diameter between 50 and 100 metres, composed by tourmaline and quartz and with copper and gold mineralisation. Around each breccia, hydrothermal fluids have altered the plutonic rocks forming clay minerals such as kaolinite and montmorillonite, but also sericite and jarosite (Figure 5.40). In the ASTER bands ratios composition red: 3/1, green: 9/3, blue: (5+9)/8 image, the alteration halos can be noted as green spots (Figure 5.39-b). That colour clearly represents the OH absorption of clay minerals. These bodies are easier to identify on the field because they are composed principally by tourmaline and quartz which are stronger than the surrounding argillified granite, so the weathering acts differently (Figure 5.41-a). In this way, the black tourmaline-bearing bodies stand out with respect to the surrounding morphology. According to Sillitoe and Sawkins (1971) these bodies are dated back to the Palaeocene.

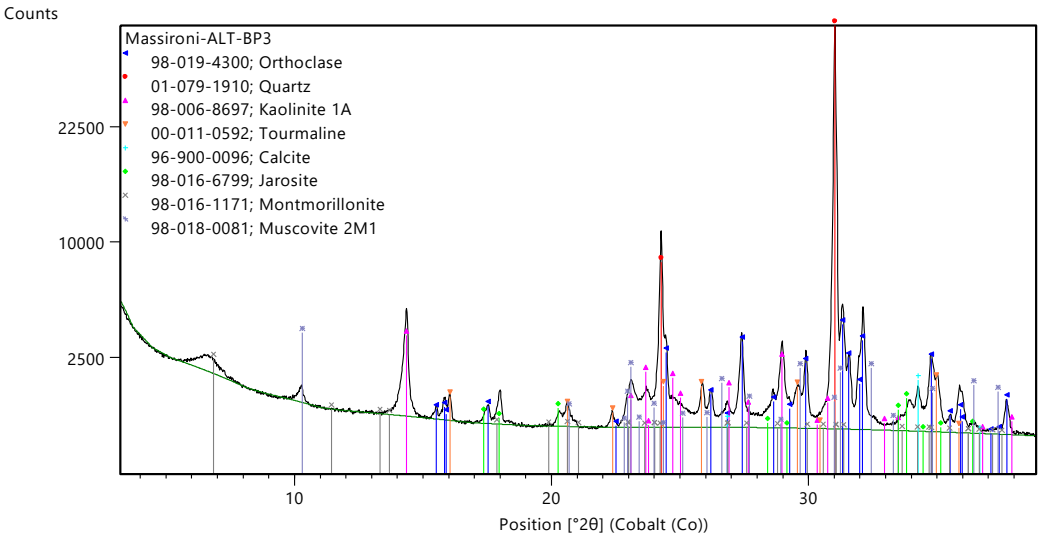

Figure 5.40 XRPD diffractogram of sample Alt BP 3

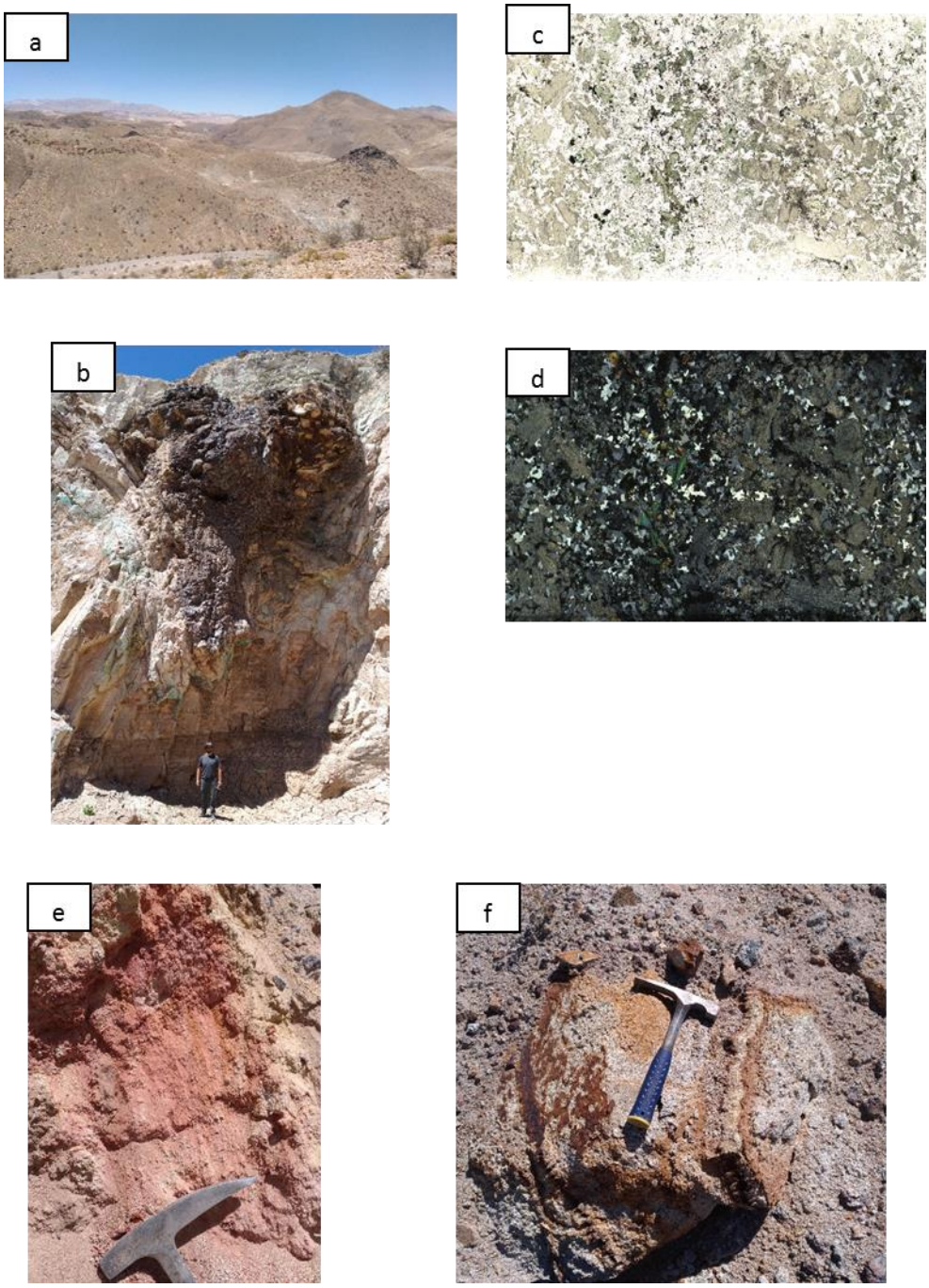

Figure 5.41 a) View that shows the different morphologies of breccia pipe bodies from wpt.111; b) Basal portion of a breccia pipe, wpt.130; c) Thin section of breccia body under parallel nichols, wpt.109; d) Thin section of breccia body under crossed nichols, wpt.109; e) Argillic alteration around breccia bodies, wpt. 106; f) Argillic alteration in a granite block, wpt.106.

6 HYPERION DATA PROCESSING

The analyses performed with the ASTER multispectral sensor have been used together with the fieldwork to create the geological map of the area. However, it was decided to perform a spectral characterization of the Carizallillo altertion area, using the Hyperion hyperspectral sensor. This area was chosen because here a High Sulfidation epithermal body has been found and studied by the Aragonita Asesorias mining company for gold extraction. In particular, being able to extract the spectral signatures of the purest pixels it is possible to search, through classifiers, possible deposits in a remote way (Khurshid et al. 2006)

Spectral hourglass wizard provided by the ENVI software version 5.3 was applied to perform this process in a Hyperion L1T file in geoTIFF format after radiometric calibration. This file was downloaded from the USGS site (https://earthexplorer.usgs.gov).

6.1 SPECTRAL HOURGLASS WIZARD

The hourglass processing flow uses the spectrally over-determined nature of hyperspectral data (respect to the multispectral one) to find the most spectrally pure, or spectrally unique, pixels (called endmembers) within the dataset and to map their locations and sub-pixel abundances. This processing flow begins with reflectance or radiance input data and continues in cascade with Minimum Noise Fraction (MNF), Pixel Purity Index (PPI), n-D visualization and, finally, with the use of the Spectral Angle Mapper classifier (Figure 6.1).

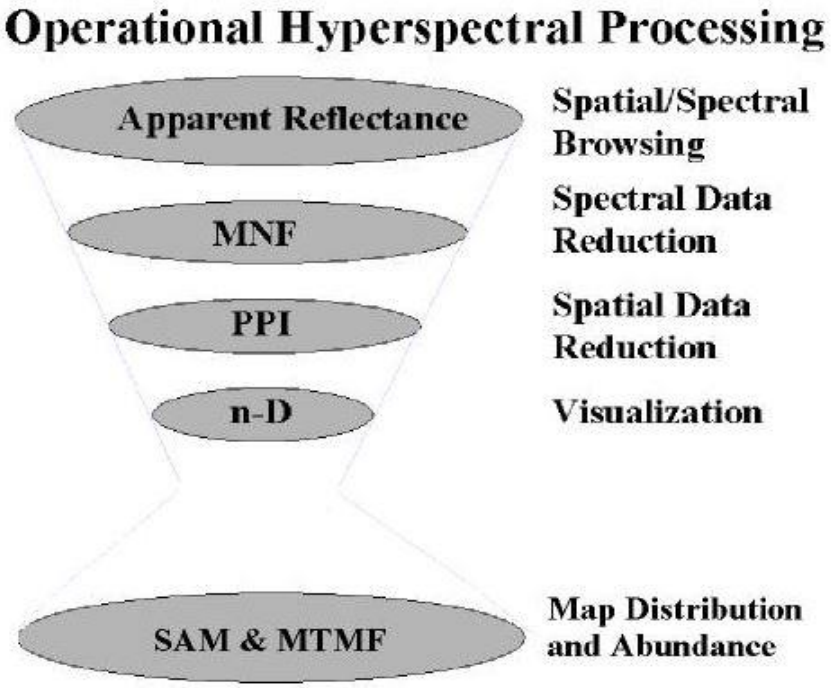

Figure 6.1_Scheme of spectral hourglass wizard.

6.2 MINIMUM NOISE FRACTION (MNF)

The Minimum Noise Fraction (MNF) transform is used to determine the inherent dimensionality of image data, and to reduce the computational requirements for subsequent processing. The MNF transform uses two cascaded Principal Components (PC) transformations (Koziol et al. 2018).

The first transformation, based on an estimated noise covariance matrix, decorrelates and rescales the noise in the data. This results in transformed data in which the noise has unit variance and no band-to-band correlations.

The second transform is a standard Principal Components transformation of the noise-whitened data. The resulting bands of the MNF transformed data are ranked with the largest amount of variance in the first few bands and decreasing data variance with increasing band number until only noise and no coherent image

remains (Figure 6.2). The bands containing only noise are not used in subsequent processing.

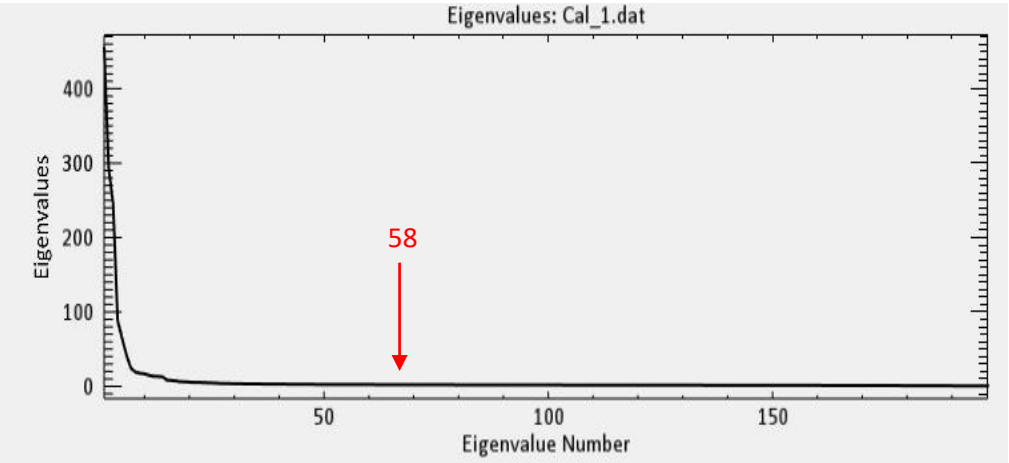

Figure 6.2_Grafic shows the eigenvalues result from MNF processing.

In particular, thresholding the MNF bands allows to separate the noise from the data, thus reducing the amount of data to be analyzed and improving spectral processing results. You can allow the Wizard to find this threshold and estimate the data dimensionality by using a Spatial Coherence measure.

ENVI calculates the spatial coherence threshold based on the bands with spatial coherence values greater than a given floor. If the threshold is set to 0, bands which score 0 will not be included. For example, if you input 50 bands into the MNF transformation and calculate the spatial coherence, it might return 36 out of 50 bands because 14 have a spatial coherence value equal to 0.

The spatial coherence curve (as applied to MNF data) should decrease as you move to higher MNF bands since the bands get noisier. Therefore, ENVI looks for the first band below the threshold and get rid of the rest.

(https://www.harrisgeospatial.com/Support/Self-Help-Tools/Help-Articles/Help-Articles-Detail/ArtMID/10220/ArticleID/19050/3821.

In this work, the threshold values applied was the default values of 0 but no values were found under to 0 after the processing so, looking to the diagram on Figure 6.2 the first 58 MNF bands have been used for the next step of the wizard.

6.3 PIXEL PURITY INDEX

The Pixel Purity Index (PPI) is used to find the most "spectrally pure," or extreme, pixels in multispectral and hyperspectral data (Martínez et al., 2006). The most spectrally pure pixels typically correspond to endmembers. The PPI is computed by repeatedly projecting n-dimensional scatter plots onto a random unit vector. The extreme pixels in each projection are recorded and the total number of times each pixel is marked as extreme is noted. A threshold value is used to define how many pixels are marked as extreme at the ends of the process. The threshold value should be approximately 2-3 times (2,5 in this work) the noise level in the data (which is 1 when using MNF transformed data) (Martínez et al. 2006).

In a n-dimensional data with many endmembers, the purest pixels still must be on the extreme corners or edges of the data cloud.

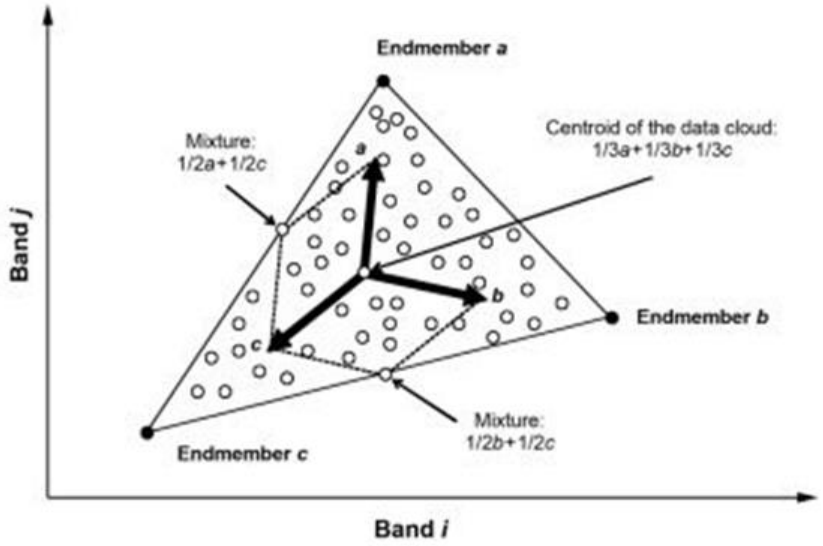

Figure 6.3 Process to found end member using PPI.

6.3.1 Calculating pixel purity index

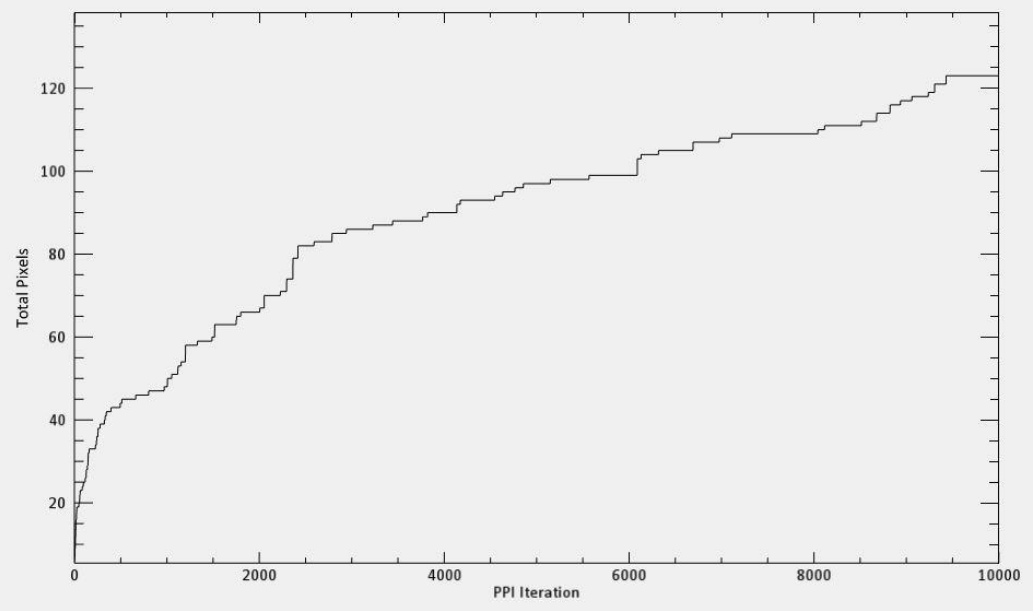

Figure 6.4_PPI result diagram.

A Pixel Purity Index Plot show the number of iteration on X axis and the cumulative number of pixels that have been found to be extreme on the Y one. The curve in the plot starts steeply because the purest pixels are target in each iteration and became flat when the last pixels are find. It is extremely difficult, if not impossible, to precisely know how many iterations are necessary but during our elaboration the curve became horizontal just before the 10000 iterations, registering 118 pixels in total (Figure 6.4).

When the specified iterations are completed, a PPI image is created in which the value of each pixel corresponds to the number of times that pixel was recorded as extreme. Bright pixels in the PPI image generally are image endmembers.

6.4 N-DIMENSIONAL VISUALIZER

N-Dimensional Visualizer provided in ENVI software need to find endmembers by locating and clustering the purest pixels in n-dimensional space. Spectra can be thought as points in a n-dimensional scatter plot, where "n" is the number of MNF bands. The coordinates of each point in n-space consist of "n" values that are simply the spectral radiance or reflectance values in each band for a given pixel.

Thus, position in the scatterplot conveys the same information as contained in the shape of the spectrum for a single pixel. In n-dimensional scatter plot space, because of the feasibility constraints, the best endmembers occur as vertices, or corners, of an n-Dimensional data cloud or mixing volume. The n-D Visualizer is used to rotate the data cloud, and to locate and highlight the corners of the cloud to find the endmembers (Martínez et al. 2006).

Recapping, through the n-D visualizer the endmembers found during PPI process are verified and refined. In this work, we have collected only the purest pixels reaching a total number of 47 end members out of 118. These pixels are saved as Region of interest (ROI) file to proceed with the last and most important stage of the wizard: spectral classification.

6.5 SPECTRAL ANGLE MAPPER

The Spectral Angle Mapper (SAM) is a classifier, able to match image spectra to reference spectra in n-dimensions (Figure 6.5). SAM compares the angle between the endmember spectrum (considered as an n-dimensional vector, where n is the number of bands) and each pixel vector in a n-dimensional space. (Kruse 1995)

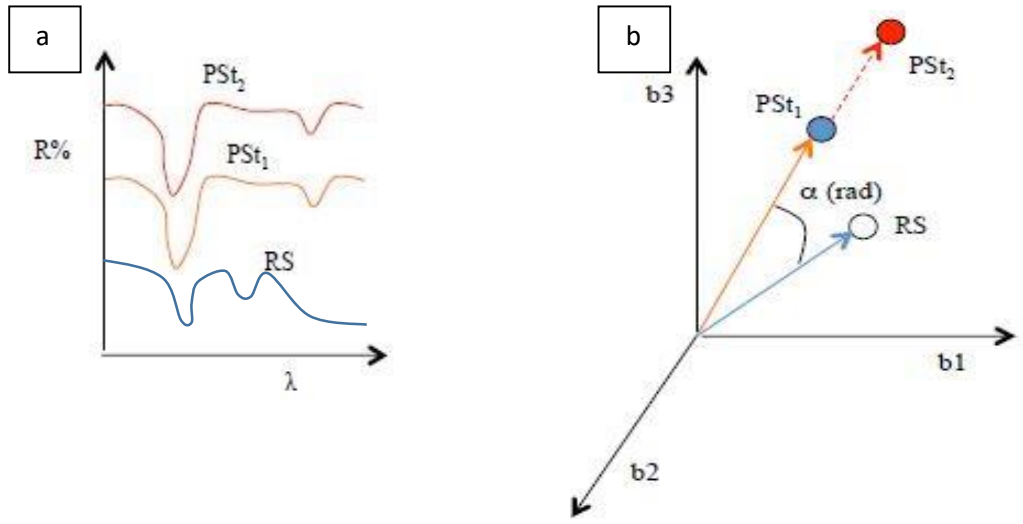

Figure 6.5_a)Spectral signature of the same object with different illumination PSt 1-2; b) Plot of the spectral signatures in an n-dimensional view as vectors, the signatures PSt 1-2 of the same material acquired in different condition of illumination are in the same vector, RS is the reference spectrum.

Smaller angles represent closer matches to the reference spectrum. This technique, when used on calibrated data, is relatively insensitive to illumination and albedo effects (Figure 6.5). SAM produces a classified image based on the SAM Maximum Angle Threshold. Decreasing this threshold usually results in fewer matching pixels (better matches to the reference spectrum). Increasing this threshold may result in a more spatially coherent image, however, the overall pixel matches will not be as good as for the lower threshold.

6.6 RESULTS

Spectral Angle Mapper classification has been applied on the Hyperion 1T image after radiometric calibration using the spectral endmembers obtained from the hourglass wizard of ENVI software. Figure 6.6 shows SAM results related to the 47 endmembers. The angle used for processing is 0.2 radians. It has been used a small angle because the endmember pixels used for the classification were identified by the same Hyperion image. In this case, the recording conditions are the same and the spectral difference between one and the other are expected to be minimal. Each colour correspond to a single endmember saved in a ROI file (Figure 6.6).

The Carizalillo zone of alteration is composed by seven different endmembers, each one with small differences from the others. In fact, the spectral signatures of the found endmembers show a similar shape between them. They show absorption peaks that can be referred to various alteration minerals, such as kaolinite, pyrophyllite, alunite, chlorite, goethite and jarosite (Figure 6.7).

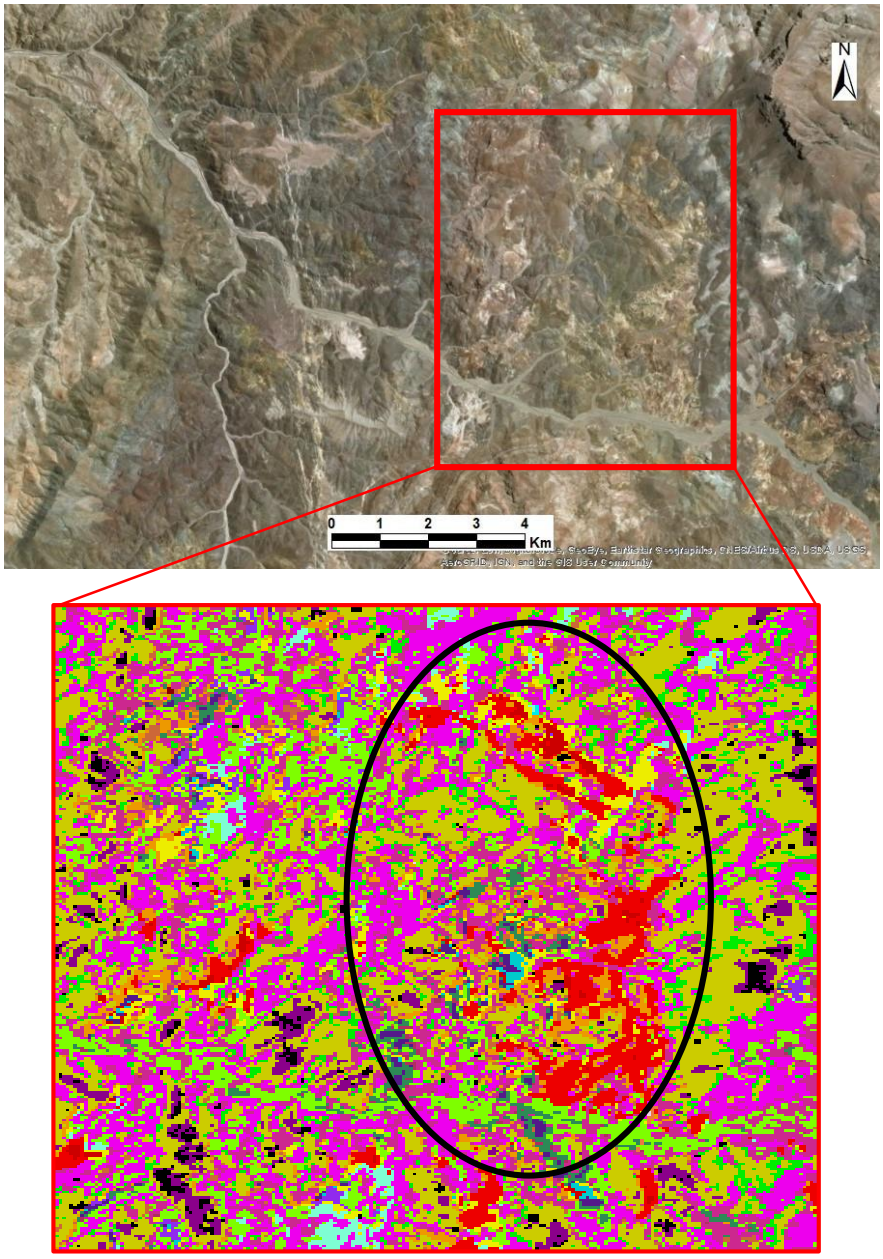

Figure 6.6_a)Basemap of Arcgis software show the Carizallillo alteration zone, (red reptangle); b) SAM classification using 47 endmember resulting from Hourglass processing in Carizallillo alteration unit (black ellipse) and neighbours area.

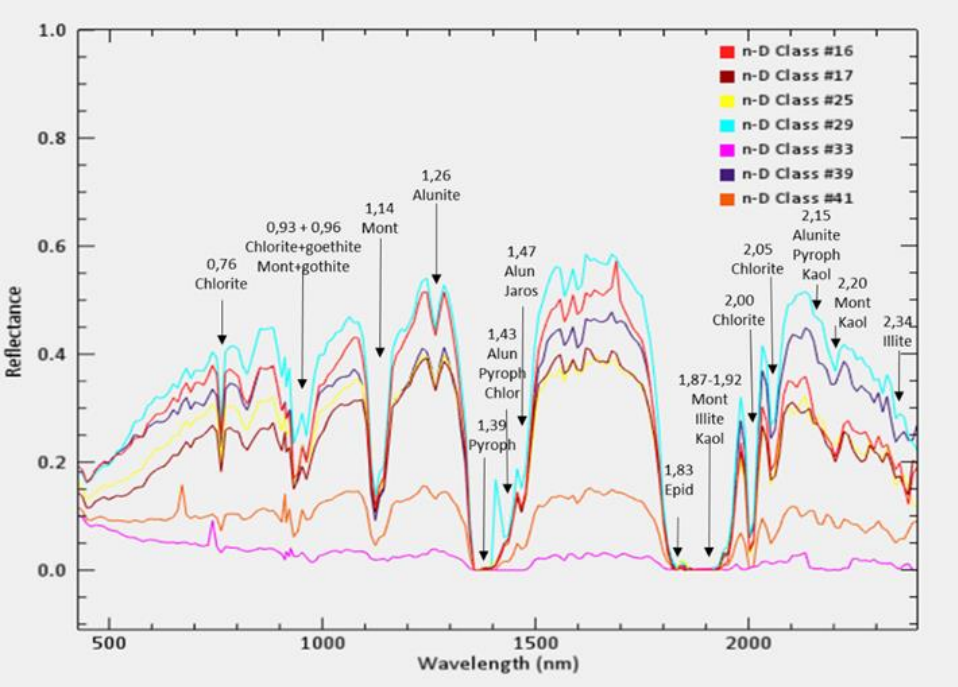

Figure 6.7_ Spectral library of the 7 selected endmembers showing which minerals are identified from each absorption peak

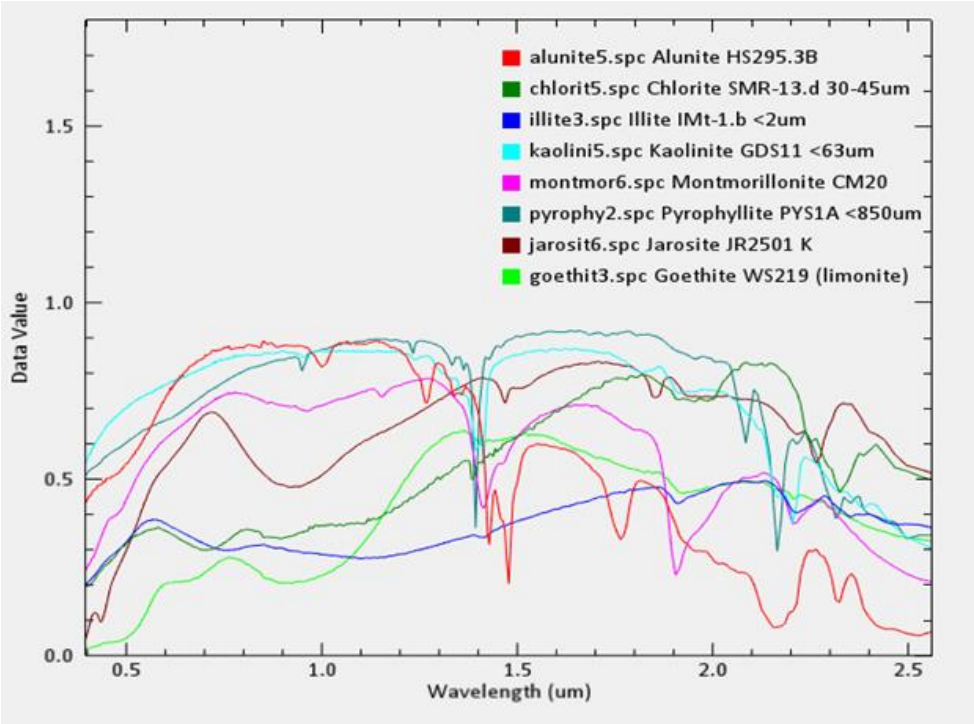

Figure 6.8_ Spectral signature of the pure minerals whose mixture are responsible of the 7 characteristic endmembers derived by the hourglass wizard.

The areas marked with cyan colour, is found in an area where a High Sulfidation epithermal body emerges is present (Aragonita Asesorias LTDA, 2016).

The cyan often is associated with violet and yellow, which correspond to silicified rock zone (see geologic map on chapter 5) where our fieldwork has highlighted a possible presence of a HS deposit. These three spectral signatures could represent a key to find specific HS deposits using hyperspectral images. In particular, in the study area 4 areas of interest have been found (Figure 6.9).

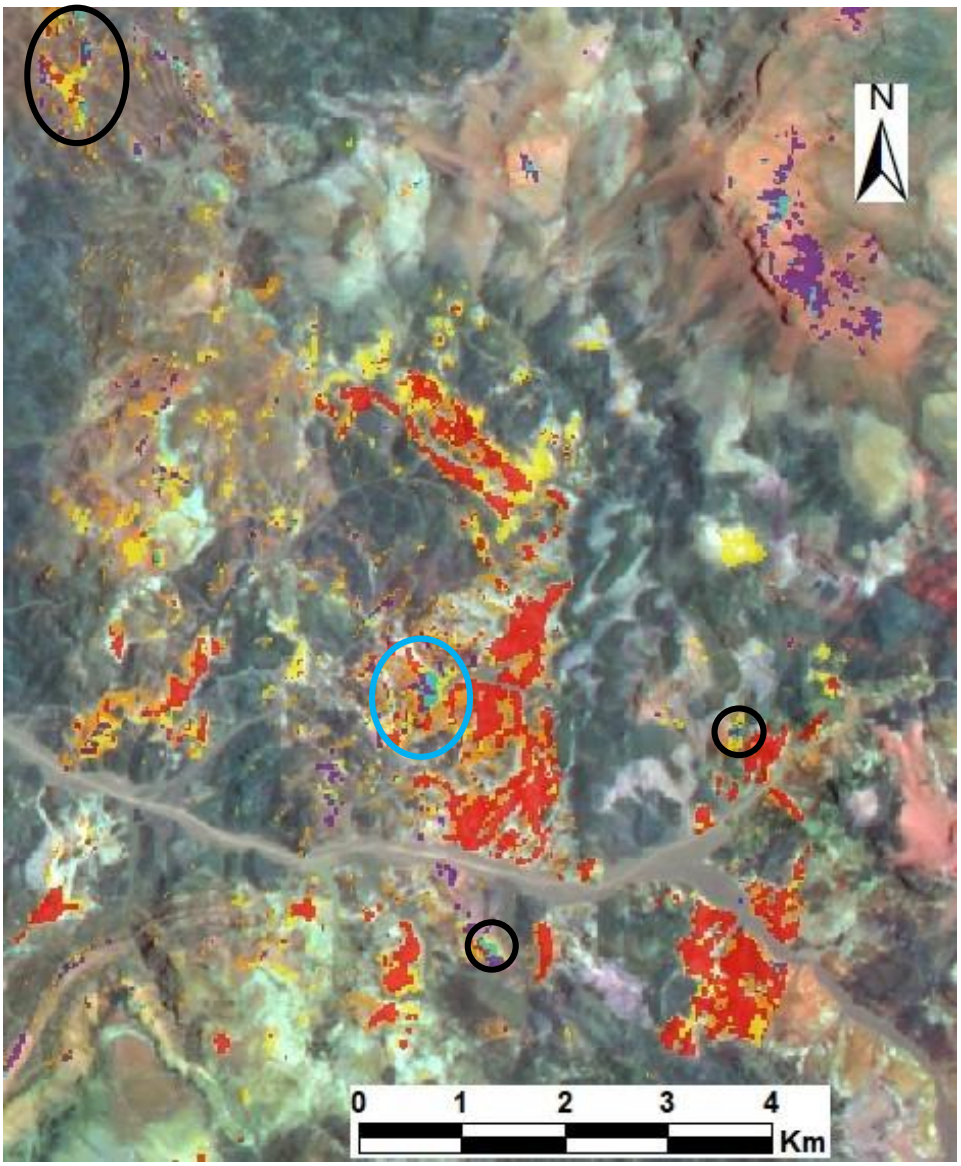

Figure 6.9_distributions of selected 7 endmembers in Carizalillo zone, Blue ellipse shows the HS deposit used for founding alterations pixels. Black ellipses highlight the prospecting zones where is possible to find HS deposits.

7 DISCUSSION

The period I spent in Chile was from October 2017 until the end of December. During this time, remote sensing elaborations, fieldwork, and sample analysis have been done. The elaboration of ASTER data showed a different spectral response by different lithologies (see chapter 4). These data were useful for planning the work in the field. Fifty-two samples were collected and analysed by transmitted light microscopy; this study began in Copiapò and was finished at the Department of Geoscience, University of Padova, with additional studies under the microscope and by X- Ray powder diffraction (XRPD) on selected samples (12 in total), to understand the different mineral associations in the alteration zones (Figure 7.1).

At the end of these analyses, a new geological map with four new alteration zones and one new unit was created. In particular, a previously unknown andesitic dome sequence was recognised and four distinct alteration zones were delimited:

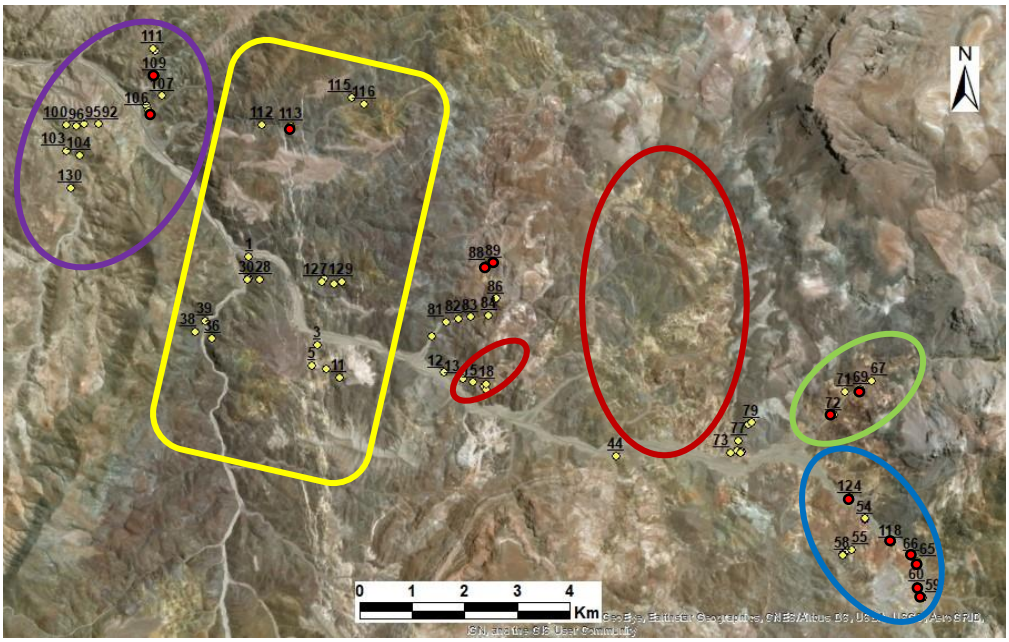

Figure 7.1_ Waypoints taken in the field (yellow spots) and sampling sites (red spots). The map scale is 1:80000. Blue ellipse: clay-rich alteration zone. Green ellipse: silicified zone. Red ellipse: Carizallillo alteration zone. Yellow feature indicate the vien-rich alteration zone. Purple ellipse indicate the breccia pipe zone.

Carizallillo high-sulphidation epithermal zone, silicified rocks zone, breccia pipe zone, clay-rich alteration zone and vein-rich alteration zone (see chapter 5).

The Carizallillo alteration zone was previously studied by the ARAGONITA ASESORIAS LTDA mining company, within a project called JASPE. During this project three high-sulphidation epithermal bodies were detected. I was able to locate these three bodies too by using the Principal Component (PC) Analysis on ASTER data. Similar areas were also detected in other locations and studied using the Hyperion data for prospecting purposes (see chapter 6). In particular, the Hourglass wizard provided by the ENVI software was used to individuate the purer pixels (endmembers) and relative spectral signatures present in the Hyperion image (see chapter 6). Seven endmembers, out of a total of forty-seven identified by the software, identify very well every alteration zone mapped during the fieldwork, and three of them perfectly recognise the alteration halos of the central epithermal body found in the JASPE project and in the PC image of ASTER. The endmembers were used to classify the zone and identify new zones of interest for mining prospection (Figure 7.3)

In particular, in the silicified rocks zone and clay-rich alteration zone a great number of samples were collected to verify the presence of ore deposits or prospective structures.

In the clay-rich alteration zone, the samples Alt C1 (wpt. 59), Alt C2 (wpt. 60), Alt C6 (wpt. 65) e Alt C7 (wpt. 66), Alt C9 (wpt. 118), Alt C15 (wpt. 124) (Figure 7.1) present a variety of alteration minerals, such as muscovite, alunite, pyrophyllite, quartz, montmorillonite, jarosite, illite and smectite. However, not all the samples are characterised by the same alteration minerals. For example, muscovite and illite are present in sample Alt C9 and allow to classify the type of alteration as phyllic. The illite–smectite association, instead, appears in sample Alt C7 and represents an intermediate argillic alteration. The association of alunite, pyrophyllite and quartz, which appears in samples Alt C2 and Alt C6, indicates a high-T (> 250°C) advanced argillic alteration (Figure 7.2). Furthermore, the sample Alt C15 (Figure 7.2) is composed by a monomineralic

aggregate of vuggy quartz, which indicates extensive alteration by acidic fluids (see chapter 3), involving complete erasure of the original structure of the rock and leaching of all chemical components other than silica.

In the silicified rocks zone, two samples, Alt M1 (wpt. 69) and Alt M2 (wpt.72), were collected and analysed (Figure 7.1). Sample Alt M1 (vuggy silica) has a texture and mineralogical composition very similar to sample Alt C15 from the neighbouring clay-rich zone and may be considered as the most representative lithotype in the silicified rocks zone. Sample Alt M2, instead, is composed of interstratified illite/smectite, in which montmorillonite is prevalent. In this case, the alteration is an intermediate argillic type, similar to that shown by sample Alt C7 from the clay-rich alteration zone. Considering the spatial relations between the different alteration zones and the partial overlap between different alteration styles, we may envisage that the observed alterations are related to the same hydrothermal system. The possible location of the studied samples within an idealised epithermal system is shown in Figure 7.2.

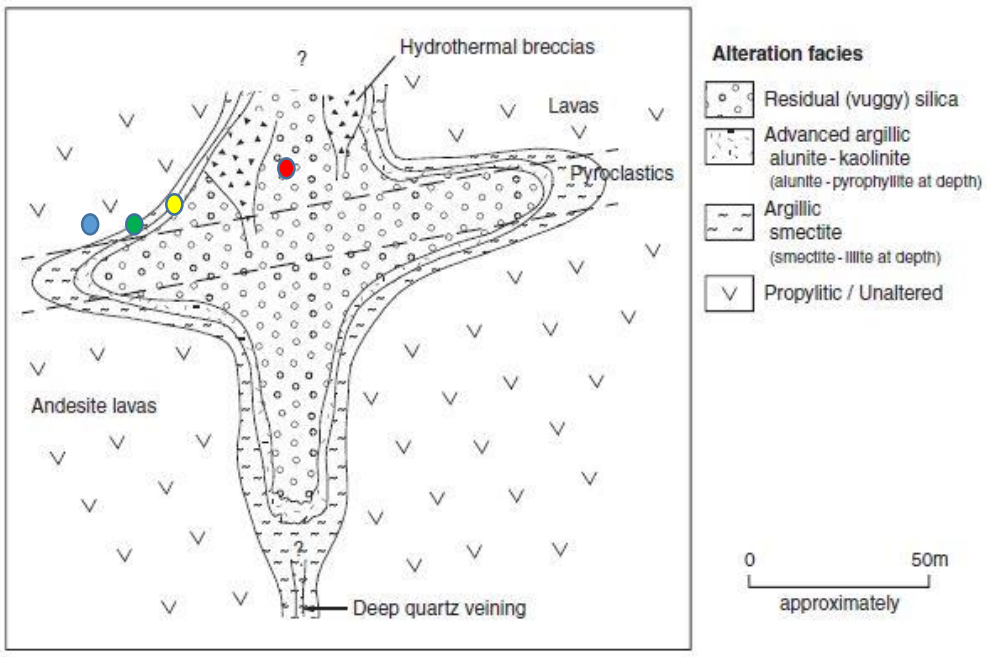

Figure 7.2_Different halos of alteration in a typical high-sulphidation epithermal system, showing the possible location of studied samples. Blue spot shows sample Alt C9, affected only by a low grade of phyllic alteration; green spot corresponds to samples Alt C7 and Alt M2, affected by intermediate argillic alteration; yellow spot correspond to samples Alt C2 and Alt C6, affected by advanced argillic alteration; red spot correspond to samples Alt C15 and Alt M2, affected by vuggy silica alteration.

Breccia pipe and vein-rich alteration zones (Figure 7.3) are characterised by the presence of ore deposits principally composed by Cu oxides exploited by local mining companies. The related alteration haloes, detected using the ASTER elaboration (see chapter 4), were characterised through XRPD analyses (see chapter 5). These have shown that around each breccia pipe a halo of argillic alteration occurs, which is composed by kaolinite, montmorillonite and sericite. In the vein-rich alteration zone (Figure 7.3), the halo detected with the ASTER elaborations is determined by a propylitic alteration formed by epidote, chlorite and albite.

The spatial and geological relations and similar alteration degree and spectral response on the satellite images suggest that the clay-rich, silicified rocks, and Carizallillo alteration zones are part of the same hydrothermal system. Instead, the hydrothermal veins occur only in the Lavas Sierra la Dichosa formation, so they could be older.

The position of Carizallillo alteration zone, clay-rich alteration zone and silicified rocks alteration zone is always so close to the Estratos De Quebrada El Romero Units (Figure 7.3). So it is possible to hypnotize the same age of these alteration zones.

As seen in chapter 5, these areas have a similar spectral response. This could suggest the apartments to the same HS system. During the ground truth, in fact, both in the silicified alteration zone and in the clay-rich alteration zone were found the similar kind of alteration (vuggy sillica and intermediate argillic alteration). What changes is the distance from a hypothetical hydrothermal vein. The silicified rock zone, given the greater content in quartz, could be in a more proximal position. The Clay rich alteration zone, rich in clay minerals, could be in a more distal zone.

It is worth noting that high-sulphidation hydrothermal systems are often linked with deeper porphyry-type systems (e.g. Sillitoe 2010). The occurrence of widespread signs of high-sulphidation hydrothermal activity in the area may thus suggest the possible occurrence of concealed and potentially even more rewarding porphyry systems at depth.

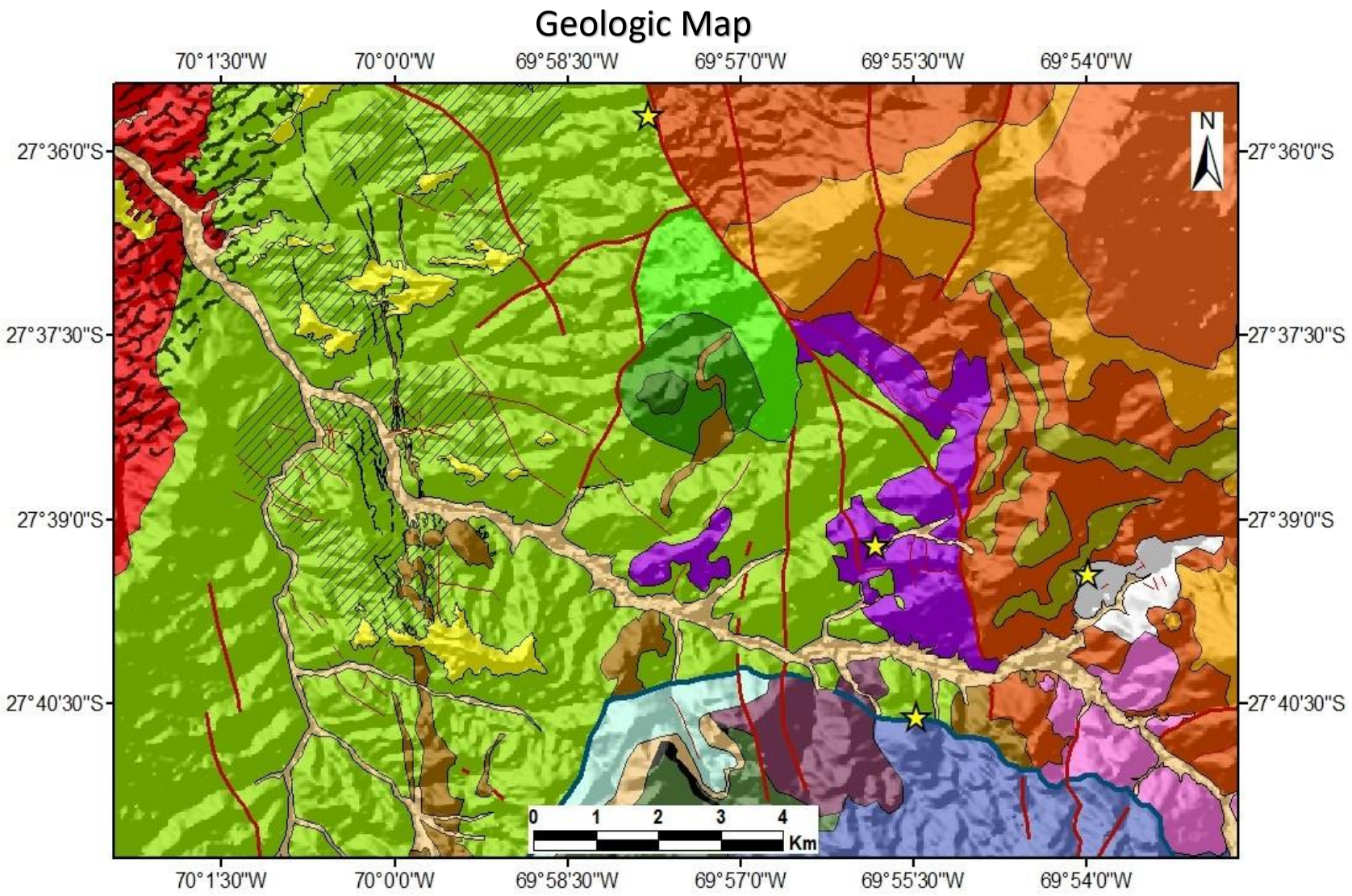

Figure 7.3_Geologic map

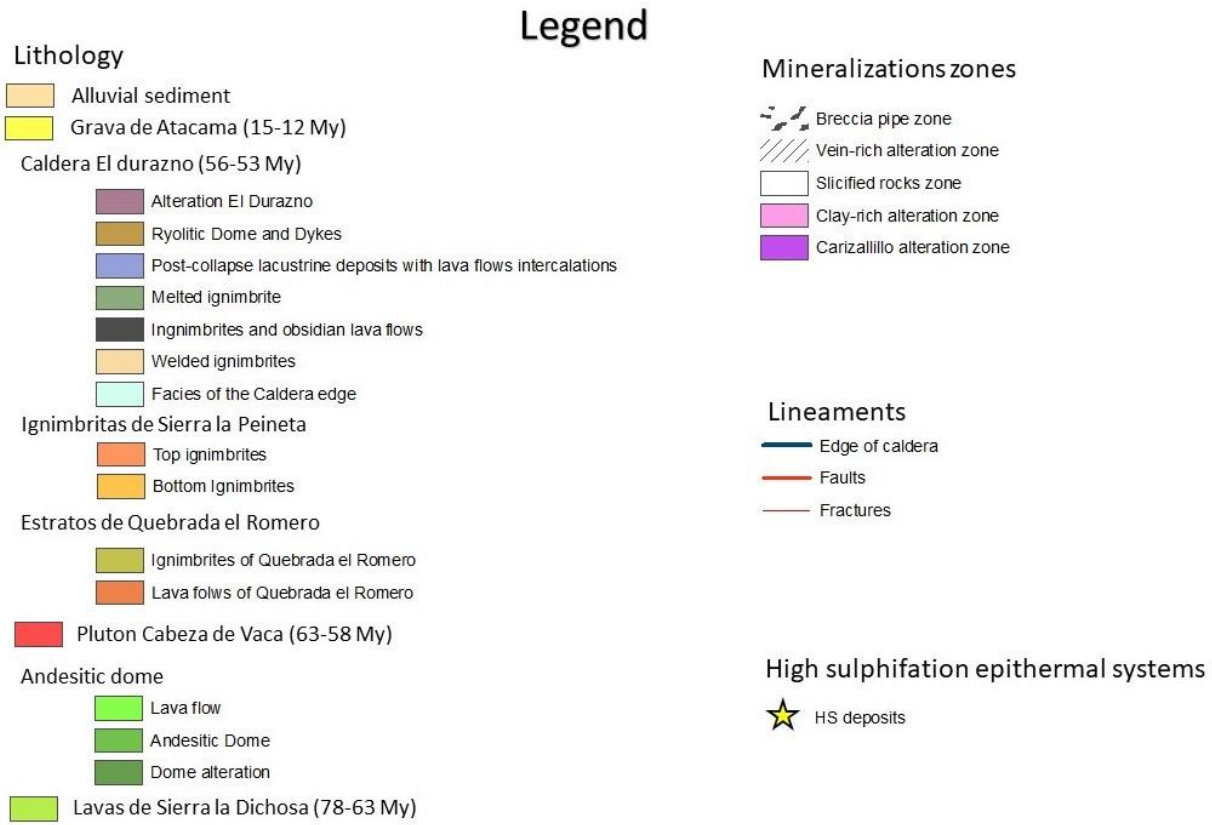

Figure 7.4_Legend related to the Quebrada Carizallillo

8 CONCLUSIONS

The aims of the work carried out in the Atacama region were:

- To improve the geological map of Hoja la Guardia provided by the Chilean geology and mining service (Iriarte 1999).
- To identify, sample, analyse and classify the different zones of alteration present in the studied area (Quebrada Carizallillo).
- To use the Hyperion hyperspectral sensor to perform a characterisation of the different alteration halos in the Carizallillo zone and individuate promising prospecting sites for new high-sulphidation deposits.

All the work phases planned at the beginning of this project have been completed.

The use of ASTER satellite image during the pre-fieldwork period was fundamental for having a first idea on the geological units and possible hydrothermal alterations, a useful prerequisite for planning detailed field-checks. The interpretation of the ASTER images were made with the support of the professors of the Universitad de Atacama Miguel Caceres and Karl Riveros and were carried out by comparing them with the existent geological map of Hoja la Guardia provided by the Chilean geology and mining service (Iriarte 1999).

The analysis of the collected samples provided important information for identifying the types of alteration, which resulted to be diverse, including: propylitic, phyllic, intermediate and advanced argillic, and vuggy silica.

The Hyperion hyperspectral data analysis, coupled with field checks and bibliographic studies (Jaspe project), allowed me to discover three new sites of interest, which may be related to high-sulphidation bodies.

In conclusion, in Quebrada Carizallillo the following ore deposits have been identified or can be inferred based on the previous and the present data:

- High-sulphidation epithermal system are located in the Carizallillo alteration zone and, with a good chance, also in the clay-rich alteration

zone, in the silicified rocks zone, in the Caldera alteration unit and in the Lavas Sierra la Dichosa unit to the north. (Figure 7.3)

- Breccia pipe bodies composed mainly by crysocolla, chalcopyrite, bornite are exposed along the contact between the Cabeza de Vaca pluton and the Lavas Sierra la Dichosa unit in the western portion of the geological map (Figure 7.3).
- Polymetallic veins in the Lava Sierra la Dichosa Unit, composed by the same copper minerals crysocolla, chalcopyrite and bornite but also by lead and zinc minerals (galena and sphalerite).

In the future, further studies to more precisely map the areas of alteration could be performed using a sensor (better hyperspectral) with high ground resolution (at least five meters). These sensors can be installed not only on satellites, but also on drones. Once the area has been characterised through the analysis of a sufficient number of samples, drilling work might be planned to identify the shape and extension of possible mineralised bodies.

9 BIBLIOGRAPHY

Abrams, M, and S Hook. 2002. "ASTER User Handbook Version 2." Jet Propulsion 2003 (23/09/2003): 135. https://doi.org/10.1017/CBO9781107415324.004.

Arevalo. 1994. "Mapa Geològico de La Hoja Los Loros." Servicio Nacional de Geologia y Mineria.

Barzoi, Sorin C., and Marin Seclaman. 2010. "Petrographic and Geochemical Interpretation of the Late Cretaceous Volcaniclastic Deposits from the Hateg Basin." Palaeogeography, Palaeoclimatology, Palaeoecology 293 (3–4): 306–18. https://doi.org/10.1016/j.palaeo.2009.08.028.

Bishop, Michael P., and Jeffrey D. Colby. 2011. "Topographic Normalization of Multispectral Satellite Imagery." Encyclopedia of Earth Sciences Series Part 3: 1187–97. https://doi.org/10.1007/978-90-481-2642-2_664.

Catchpole, Honza, Kalin Kouzmanov, Lluís Fontboté, Marcel Guillong, and Christoph A Heinrich. 2011. Fluid Evolution in Zoned Cordilleran Polymetallic Veins - Insights from Microthermometry and LA-ICP-MS of Fluid Inclusions. CHEMICAL GEOLOGY. Vol. 281. https://doi.org/10.1016/j.chemgeo.2010.12.016.

Charrier, Reynaldo, Luisa Pinto, and María Pía Rodríguez. 2002. "Tectonostratigraphic Evolution of the Andean Orogen in Chile." The Geology of Chile, 21–114. https://doi.org/10.1144/GOCH.3.

Coira, B, John Davidson, Constantino Mpodozis, and Victor Ramos. 1982. Tectonic and Magmatic Evolution of the Andes of Northern Argentina and Chile. Earth-Science Reviews. Vol. 18, 303-332. https://doi.org/10.1016/0012-8252(82)90042-3.

D. Lowell, J, and J M. Guilbert. 1970. Lateral and Vertical Alteration-Mineralization Zoning in Porphyry Ore Deposits. Economic Geology. Vol. 65,373-408. https://doi.org/10.2113/gsecongeo.65.4.373.

David Dallmeyer, R, Michael Brown, John Grocott, G Taylor, and Peter Treloar. 1996. Mesozoic Magmatic and Tectonic Events within the Andean Plate Boundary Zone, 26°-27°30'S, North Chile: Constraints from [Tex-Math](40}Ar/({39)) Ar[/Tex-

Math] Mineral Ages. Journal of Geology. Vol. 104, 237-340. https://doi.org/10.1086/629799.

Díaz-Alvarado, J., N. Rodríguez, P. Fuentes, e F. Torres. 2016. "Geología de La Caldera El Durazno. Sistema de Calderas de Colapso Paleoceno-Eoceno Durante La Reactivación Del Magmatismo Asociado a La Megacaldera Carrizalillo, Precordillera Del Norte de Chile. VIII Congreso Uriguayo de Geologìa"

E. McCallum, M. 1985. Experimental Evidence for Fluidization Processes in Breccia Pipe Formation. Economic Geology. Vol. 80, 1523-1543. https://doi.org/10.2113/gsecongeo.80.6.1523.

Hart, Craig, and Richard Goldfarb. 2005. Distinguishing Intrusion-Related from Orogenic Gold Systems. Proceedings of Scientific Conference on Minerals, New Zealand.

Hartley, A J, G May, G Chong, P Turner, S J Kape, and E J Jolley. 2000. "Development of a Continental Forearc: A Cenozoic Example from the Central Andes, Northern Chile." Geology 28. Vol 4, 331–349. https://doi.org/10.1130/0091-7613(2000)028<0331:DOACFA>2.3.CO;2.

Iriarte, S., C. Arévalo, e C. Mpodozis. 1999. "Mapa Geológico de La Hoja La Guardia." Servicio Nacional de Geología y Minería.

Jeffrey W. Hedenquist. 2000. "Exploration for Epithermal Gold Deposits." SEC; Reviwss Vol.13, 245–277.

Kennth, Segerstrom. 1968. "Geología de Las Hojas Copiapo y Ojos Del Salado." Instituto de Investigaciones Geologica (Chile).

Khurshid, Shahid, Karl Staenz, Lixun Sun, R A Neville, H P White, Bannari Abdou, Catherine Champagne, and Robert Hitchcock. 2006. Processing of EO-1 Hyperion Data. Canadian Journal of Remote Sensing. Vol. 32, 84-97. https://doi.org/10.5589/m06-014.

Koziol, Paulina, Magda K. Raczkowska, Justyna Skibinska, Sławka Urbaniak-Wasik, Czesława Paluszkiewicz, Wojciech Kwiatek, and Tomasz P. Wrobel. 2018. "Comparison of Spectral and Spatial Denoising Techniques in the Context of High

Definition FT-IR Imaging Hyperspectral Data." Scientific Reports 8 Vol.1, 1–11. https://doi.org/10.1038/s41598-018-32713-7.

Kruse, Fred A. 1995. "Geologic Mapping Using Combined Analysis of Airborne Visible/Infrared Imaging Spectrometer (AVIRIS) and SIR-C/X-SAR Data."

Laurence Robb. 2006. Introduction to Ore-Forming Processes, by Laurence Robb. Mineralium Deposita - Blackwell Science Ltd Vol. 41 (129-174). https://doi.org/10.1007/s00126-006-0089-z.

Laznicka, P. 2006. Giant Metallic Deposits: Future Sources of Industrial Metals. Giant Metallic Deposits: Future Sources of Industrial Metals.Secon edition,109-176. https://doi.org/10.1007/3-540-33092-5.

Martínez, Pablo J., Rosa M. Pérez, Antonio Plaza, Pedro L. Aguilar, María C. Cantero, and Javier Plaza. 2006. "Endmember Extraction Algorithms from Hyperspectral Images." Annals of Geophysics 49 Vol.1, 93–101. https://doi.org/10.4401/ag-3156.

Massironi, Matteo, Luca Bertoldi, Paolo Calafa, Dario Visonà, Andrea Bistacchi, Claudia Giardino, and Alessio Schiavo. 2008. "Interpretation and Processing of ASTER Data for Geological Mapping and Granitoids Detection in the Saghro Massif (Eastern Anti-Atlas, Morocco)." Geosphere ,4 736. https://doi.org/10.1130/GES00161.1.

Pardo-Casas, Federico, and Peter Molnar. 1987. Relative Motion of the Nazca (Farallon) and South American Plates Since Late Cretaceous Time. Tectonics. Vol. 6, 233-248. https://doi.org/10.1029/TC006i003p00233.

Pirajno, Franco. 2009. Hydrothermal Processes and Mineral Systems,Springer Sciece Business Media B.V: 73-126 (https://doi.org/10.1007/978-1-4020-8613-7_10.

Pour, Amin Beiranvand, and Mazlan Hashim. 2012. "The Application of ASTER Remote Sensing Data to Porphyry Copper and Epithermal Gold Deposits." Ore Geology Reviews 44: 1–9. https://doi.org/10.1016/j.oregeorev.2011.09.009.

Ramos, Victor. 1999. Plate Tectonic Setting of the Andean Cordillera. Episodes. Vol. 22, 183-190.

Ridley, John. 2013. Ore Deposit Geology.,Cambridge University Press (92-238).

Rivera, O, C Mpodozis, C Arèvalo, e S Iriarte. 1994. "Cuenca Extensionales y Campos de Calderas Del Cretacico Superior-Terciario Inferior En La Precordillera de Copiapò (27°-28° S), Chile." Actas 2.

Sillitoe, R H, and F J Sawkins. 1971. "Geologic, Mineralogic and Fluid Inclusion Studies Relating to the Origin of Copper-Bearing Tourmaline Breccia Pipes, Chile." Economic Geology Vol.66, 1028–1041. http://dx.doi.org/10.2113/gsecongeo.66.7.1028.

Sillitoe R.H. 2010. Porphyry copper systems. Economic Geology 105, 3–41

Singh, Ashbindu, and Andrew Harrison. 1985. Standardized Principal Components. International Journal of Remote Sensing - INT J REMOTE SENS. Vol. 6, 883-896.https://doi.org/10.1080/01431168508948511.

Somoza, Ruben. 1998. Updated Nazca (Farallon)-South America Relative Motions during the Last 40 My: Implications for Mountain Building in the Central Andean Region. Journal of South American Earth Sciences. Vol. 11, 211-215. https://doi.org/10.1016/S0895-9811(98)00012-1.

Uyeda, S, and C Nishiwaki. 1980. "Stress Field, Metallogenesis and Mode of Subduction." Edited by Strangway D.W. The Continental Crust and Its Mineral Deposits. Proc. Symposium Held for J.Tuzo Wilson, Toronto, May 1979, 323–339. https://www.scopus.com/inward/record.uri?eid=2-s2.0-0019093592&partnerID=40&md5=6ae5c407f14ec85285bd41a3981aee41.

W. Burnham, C. 1985. Energy Release in Subvolcanic Environments: Implications for Breccia Formation. Economic Geology. Vol. 80, 1467-1514. https://doi.org/10.2113/gsecongeo.80.6.1515.

Yáñez, G, J Cembrano, M Pardo, C Ranero, and D Selles. 2002. "The Challenger–Juan Fernández–Maipo Major Tectonic Transition of the Nazca–Andean Subduction System at 33–34°S: Geodynamic Evidence and Implications." Journal of South American Earth Sciences 15, 23–38. https://doi.org/https://doi.org/10.1016/S0895-9811(02)00004-4.

RINGRAZIAMENTI

Dopo questo lungo periodo di sacrifici finalmente il giorno della consegna della tesi è arrivato. È stato un periodo di profondo apprendimento, non solo a livello scientifico, ma anche personale. Vorrei perciò spendere due parole di ringraziamento nei confronti di tutte le persone che mi hanno sostenuto e aiutato durante questo percorso.

Un ringraziamento particolare va ai miei relatori, i professori Matteo Massironi, senza il quale l'esperienza trascorsa in Cile non sarebbe stata possibile, e Paolo Nimis per i loro preziosi consigli.

Gracias a todos los profesores chilenos: Miguel, Tatiana, Manuel y Karl que me han apoyado durante me estancia en Copiapò.

Miguel, Olga, Miguelito, Cony, Manu y Taty: gracias por hacerme sentir como en casa.

Un ringraziamento particolare va alla mia famiglia che mi ha sempre sostenuto senza mai chiedere nulla in cambio. Nonostante le difficoltà infatti mi avete sempre permesso di portare avanti le mie passioni ed ambizioni. Grazie.

Nei momenti difficili credo che ogni persona debba avere qualcuno con cui confidarsi. Un grazie perciò va anche a tutti i miei amici, in particolare Marco e Ilaria, che non rifiutano mai una chiacchierata davanti una buona birra e al merlo, fedele compagno di avventure oltreoceano.

Un ringraziamento va inoltre a tutti gli amici del rugby, con cui ho condiviso mille avventure.

Infine, voglio ringraziare Ilaria. Mi sei stata accanto durante tutto questo periodo sia in Italia che in Cile. Mi hai supportato durante i momenti di sconforto e sopportato nei momenti di maggior tensione, quando tutto sembrava remare contro e quando non sapevo dove sbattere la testa. Tu, che con un sorriso sei capace di raddrizzare una giornata storta. Grazie stellina.

Un sentito grazie a tutti!